LIQUID METAL-BASED DEVICES FOR ENERGY HARVESTING AND HEALTH MONITORING THROUGH HUMAN SWEAT

ZHONG LENI

PhD

The Hong Kong Polytechnic University

2024

The Hong Kong Polytechnic University

School of Fashion and Textiles

Liquid Metal-based Devices for Energy Harvesting and Health Monitoring through Human Sweat

Leni Zhong

A Thesis Submitted in Partial Fulfillment of the

Requirements for the Degree of Doctor of Philosophy

October 2023

CERTIFICATE OF ORIGINALITY

I hereby declare that this thesis is my own work and that, to the best of my knowledge and belief, it reproduces no material previously published or written, nor material that has been accepted for the award of any other degree or diploma, except where due acknowledgment has been made in the text.

_____ (Signed)

ZHONG Leni (Name of Student)

ABSTRACT

The skin, being the largest organ in the human body, contains various structures such as sweat glands, hair follicles, hair arrector muscles, and sebaceous glands. Except for specific areas like the vermillion border of the lips, the majority of the skin is equipped with sweat glands that continuously secrete sweat. Studies have reported the secretion of approximately 200-600 $g \cdot m^{-2} \cdot day^{-1}$ of sweat from the skin. Sweat comprises water, ions, lactate, glucose, and other metabolites, which not only provide information about the health status but also contain biological energy. Hence, this naturally produced biological energy presents an environmentally friendly, renewable source that can be utilized to power wearable devices. To harness this biological energy from sweat, the development of stretchable and conformal wearable biofuel cells is necessary. Liquid metal-based materials, particularly gallium alloys, demonstrate promise due to their stretchability, conformal properties, and biocompatibility. In this study, liquid metals were employed to fabricate stretchable biofuel cells aiming to harvest energy from sweat and to develop sweat sensors to detect analytes such as glucose, lactate, sodium ions, and potassium ions in sweat.

We utilized screen-printing method and transfer-printing method to pattern liquid metal circuits on polydimethylsiloxane (PDMS) substrates, which resulted in a metal-polymer conductor (MPC). The MPCs are with a maximum tensile strain of over 200%. After structural designing of the liquid metal-based biofuel cell patch, it allowed the carbon electrodes of the biofuel cell to retain their shape even when subjected to a strain of 40%. By modifying glucose oxidase or lactate oxidase, we fabricated glucose biofuel cells and lactate biofuel cells, respectively. With 0.2 mM glucose, the glucose biofuel cell attained a maximum power density of 14.11 $\mu W \cdot cm^{-2}$. With the lactate concentration of 15 mM, the lactate biofuel cell achieved a maximum power density of 31.00 $\mu A \cdot cm^{-2}$. By connecting extra booster module to harvesting energy, the biofuel cell patch was used to power wearable sensors, such as temperature, oximeter, and heart rate sensors, to monitor subjects' physical metrics during exercise.

In addition, we employed electrospinning technology to fabricate an air-permeable stretchable thermoplastic polyether urethane (TPU) electrospun mat. We successfully developed an air-permeable biofuel cell mat based on liquid metal by combining this electrospun mat with stretchable, low-resistance sponge-like carbon electrodes (SLCEs). This innovative design makes the mat breathable (passing 5.42 $g \cdot m^{-2} \cdot h^{-1}$ water in 60% humidity) while maintaining its stretchable characteristics. These biofuel cells demonstrated the maximum power density of 219 $\mu W \cdot cm^{-3}$ with 15 mM lactate. Directly connecting the biofuel cell with strain sensors can indicate the strain of sensors by the output current change.

At last, we built a profile of sweat that showed the pH of sweat to be acidic, lactic acid concentration is in the range of 4-82 mM, glucose concentration in sweat is in the range of 16-200 μM, sodium ion concentration is the highest at 52-266 mM, and potassium ion concentration is lower at 10-39 mM, the calcium ion concentration is 80-453 μM. We employed screen printing liquid metal-based sweat sensors for sweat detection. Additionally, we tackled the issue of electrochemical impurities present in real samples by incorporating an extra working electrode without any active substances into the system, effectively eliminating interference during analysis. We applied such liquid metal-based sweat sensors in situ to record and analyze glucose, lactate, sodium, and potassium changes of the subject during exercise.

In summary, the thesis highlights the potential of utilizing sweat as a renewable and clean energy source to power wearable devices and an indicator of health status. Liquid metal showed promise for developing such wearable biofuel cells and sweat sensors due to their stretchability, conformal ability, and biocompatibility.

LIST OF PUBLICATIONS

Published Paper(s):

Leni Zhong, Lixue Tang, Shuaijian Yang, Zhenting Zhao, Zijian Zheng, and Xingyu Jiang. Stretchable Liquid Metal-Based Metal-Polymer Conductors for Fully Screen-Printed Biofuel Cells. Analytical Chemistry 94, no. 48 (2022): 16738-16745.

Paper in Preparation:

Leni Zhong, Zhenting Zhao, Saijie Wang, Wancheng Yu, Fan Chen, Zijian Zheng, and Xingyu Jiang. Permeable Liquid Metal Mat for Energy Harvesting and Health Monitoring through Human Sweat.

ACKNOWLEDGEMENTS

First and foremost, I would like to express my sincere gratitude to my supervisor Prof. Zijian Zheng and Prof. Xingyu Jiang for generously offering me such a precious opportunity to conduct my PhD study in their groups. Their wealthy knowledge and meticulous attitudes towards scientific research inspired and shaped me a lot. Their patient guidance and encouragement support me move forward progressively.

I am much grateful for every member in Prof. ZHENG's group and Prof. JIANG's group for the great lab environment as well as the helping group culture contributed by all of them (Dr. Yuan Gao, Dr. Miya Ng, Dr. Qiayao Huang, Dr. Yi Pei, Dr. Yuqi Zhang, Dr. Xi Lu, Dr. Lei Wang, Dr. Lina Chen, Dr. Hong Hu, Dr. Yaokang Zhang, Dr. Wenshuo Wang, Dr. Joanne Ng, Dr. Yufeng Luo, Dr. Hailong Xu, Dr. Junling Xu, Dr. Pengwei Wang, Dr. Wenjiao Ge, Mr. Zhenyao Wei, Mr. Fan Chen, Mr. Wancheng Yu, Mr. Chuan Xie, Ms. Mingming Rong, Ms. Yawen Dai, Ms. Qianyi Guo, Ms. Qiuna Zhuang, Ms. Huixin Wang, Mr. Pengxiang Zhang, Mr. Shuaicheng Wang, Dr. Ziran Wang, Dr. Yong Yang, Dr. Hao Tang, Dr. Dou Wang, Dr. Yi Liu, Dr. Panpan Gao,). Special thanks go to Dr. Lixue Tang, Mr.Saijie Wang, Dr.Zhenting Zhao, Mr.Wancheng Yu, Mr.Shuaijian Yang, Mr. Lei He, Mr. Zhenyao Wei, Dr. Zeyang Pang, Dr. Jie Qi, Dr. Pengwei Wang, Dr. Yichun Ding, Dr. Ziran Wang, Dr. Qiyao Huang, Dr. Siying Wu, Dr. Yaokang Zhang, Ms. Qiuna Zhuang, Mr. Fan Chen, for their intensive training, assistance, discussion, and suggestion during my daily lab research activities. Many thanks are for all the technicians and partners who are actively engaged in this project.

Last but not least, I am very indebted to the financial support from the Hong Kong Polytechnic University and Southern University of Science and Technology. I am encouraged for the spiritual support from my parents, family members, and friends.

TABLE OF CONTENTS

LIST OF FIGURES

LIST OF TABLES

LIST OF ABBREVIATION

Abbreviation	
BFCs	Biofuel cells
CA	Chronoamperometry
CP	Chronopotentiometry
CV	Cyclic voltammetry
DC	Direct current
DCMC	Dialdehyde carboxymethyl cellulose
DET	Direcet electron transfer
DI water	Deionized water
DMF	Dimethylformamide
EBFCs	Enzymatic biofuel cells
ECG	Electrocardiograms
ECSA	Electrochemical active surface area
EGaIn	Eutectic gallium and indium
EIS	Electrochemical impedance spectroscopy
EMG	Electromyograms
HPC	Hydroxypropyl chitosan
ISF	Interstitial fluid
KPS	Potassium persulfate, $K_2S_2O_4$
LSV	Linear sweeping voltage
MPC	Metal-polymer composite
MWCNTs	Multi-wall carbon nanotubes
NFC	Near field communication
OCP	Open circuit potential
ORR	Oxygen reduction reaction
PDMS	Polydimethylsiloxane
PVB	Polyvinyl butyral
PMMA	Polymethyl methacrylate
PI	Polyimide
PVP	Poly(4-vinylphenol)

PS	Polystyrene
PVA	Polyvinyl alcohol
PEDOT	Poly(3,4-ethylenedioxythiophene)
PET	Polyethylene terephthalate
PVDF	Polyvinylidene fluoride
RF	Radio frequency
SEM	Scanning electron microscope
SEBS	Styrene-ethylene-butylene-styrene
SPEs	Scrren-printing electrodes
SC	Supercapacitor
TENGs	Triboelectric nanogenerators
THF	Tetrahydrofuran
TPU	Thermoplastic polyether urethanes

Chapter 1 Introduction

1.1 Background and Challenges

Alongside the development of material sciences and electronic engineering, wearable electronic devices have spreading application in daily life.[1]Wearable devices can be divided into invasive (such as pacemaker)[2], semi-invasive (microneedle patch)[3] and non-invasive (such as electronic skin, electronic glasses, electronic watches, etc.)[4, 5], which need to meet the requirements of softness. characteristics, bendability and stretchability to adapt to the strength of human tissue and changes in human posture. Ideally, these wearable devices can be used as biosensors to monitor the human body in real-time for a long time, collect and record bio signals, and can connect and export data with smart devices such as smartphones through wireless modules or Bluetooth modules.[6] The use of wearable electronic devices with biomedical monitoring functions is expected to realize home diagnosis and treatment services, miniaturization, and integration of traditional complex medical tests. [47] It has become a trend in this field to vigorously develop flexible and stretchable wearable devices and convert traditional microelectronic integrated circuits into flexible circuits.[8]

Compared with invasive wearable devices, non-invasive wearable devices are safer, have no risk of infection, require no surgical treatment, are more convenient to wear, and better meet the requirements of home health monitoring.[9] As the largest organ of the human body, the skin can non-invasively acquire various physiological indicators such as electrophysiological signals, blood oxygen signals, body temperature, pulse, blood pressure, and biomolecular information in body fluids.[10] It is an ideal object for home health monitoring. At present, non-invasive wearable devices can be divided into electronic-skins (e-skin)[11], electronic-textiles (e-textiles) [12,13-15], and functional accessories (contact lenses, watches, braces, etc.)[16, 17].

For the skin wearable system, the biggest problem is the compatibility issue, including the soft and hard compatibility between emerging flexible devices and traditional electronics, and the compatibility between electronic devices for daily care. Although researchers applied intrinsically conductive polymers to develop stretchable diodes,[18] traditional electronic components are still the mainstream in current flexible electronic devices. Mechanical mismatch between these rigid components and flexible substrates and flexible circuits can cause overall device damage during use. In this regard, researchers turned to focus on liquid metal-based electronics because the modulus of liquid metal is close to zero (Figure 1.1a).[19] Moreover, liquid metal-based electronics have higher conductivity in a wide strain range compared to other conductive materials (Figure 1.1b).[20] Liquid metal-based stretchable conductors are made in different types including the fibers,[21] microchannels,[22] composites,[23, 24 25, 26] and sponges.[27, 28] However, none of these electronics are permeable. Actually, the permeability of skin electronics is very important but is always overlooked in past works. Long-term wearing of impermeable electronics will cause a series of skin ailments because human skin bear the ability to release moisture. Hence, it is of important practical value to develop permeable liquid-metal electronics.

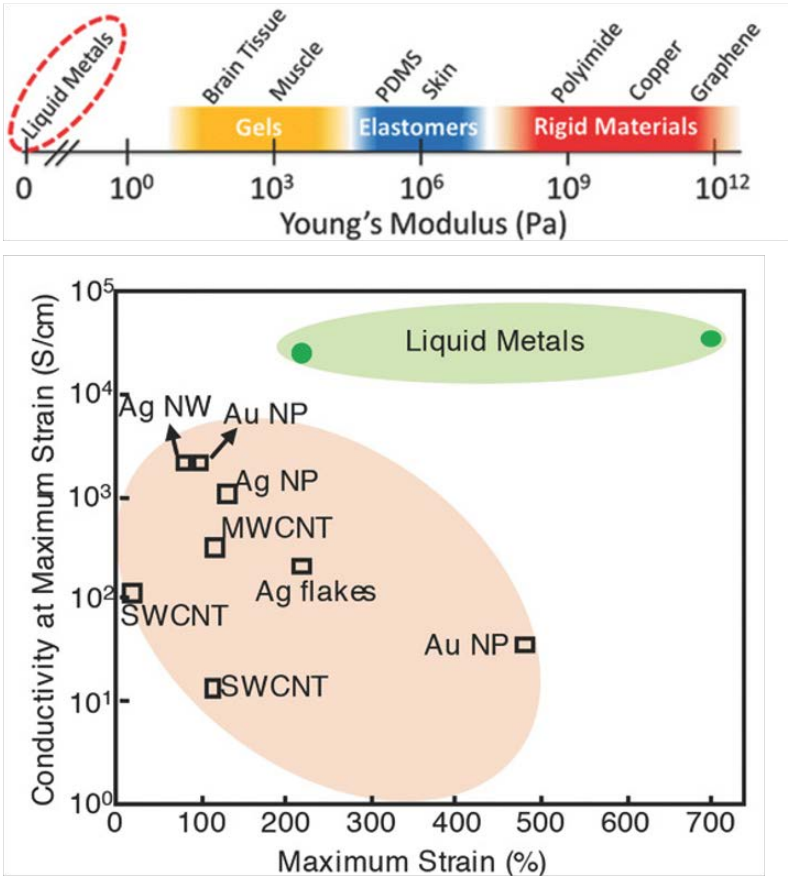

Figure 1.1 Comparison of Young's Modulus and strain of liquid metal with other materials for wearable devices.[19, 20]

1.2 Research Objectives

In accordance with the challenges that are mentioned above, this study aims to develop liquid metal-based devices for energy harvesting and health monitoring through human sweat. The detail objectives being addressed in this research are:

1. To develop a stretchable liquid metal-based biofuel cell using liquid metal that possesses stretchable properties. The fabrication process will involve integrating the liquid metal into a stretchable material, allowing the biofuel cell to be easily conformable to various surfaces. The resulting stretchable biofuel cell will enable comfortable and unobtrusive energy harvesting for wearable devices, enhancing their practicality and usability.

2. To fabricate an air-permeable liquid metal-based biofuel cell with stretchable and low-resistance sponge-like carbon electrodes. The efficiency and performance of the biofuel cell will be enhanced by incorporating air-permeable electrospun mat and low-resistance sponge-like carbon electrodes. The fabrication process will involve engineering the structure and composition of the electrodes to enlarge the ratio of surface to volume and elongate the stability of the electrode, resulting in improved power output.

3. To propose a testing method for calibrating liquid metal-based sweat sensors for enhancing the accuracy of sweat sensors among difference sweat samples and to establish a correlation between the sensor readings and the actual physiological parameters. By calibrating the sensors, the objective is to enhance their accuracy and reliability in detecting and monitoring biomarkers in sweat, facilitating more precise health monitoring.

1.3 Research Significance and Values

With the increasing demand for healthcare, there has been a rise in the availability of household and portable health testing products in the consumer market. The focus in this field is on immediate results, accuracy, convenience, and comfort. As a result, wearable electronic devices and electronic tattoos based on flexible materials have become popular, in addition to accessories like smartphones, smart watches, and smart glasses. Liquid metal, known for its unique properties of elasticity, high conductivity, and processability, is being increasingly utilized in this domain. Consequently, liquid metal-based materials are anticipated to become a prevalent choice for wearable electronics in the future.

This research aims to develop wearable devices for sweat-based applications. Sweat is the biofluid secret by skin, the largest organ of human body. For the individual, there are around 0.6-2.3 L sweat generating in daily life. Not only the process of perspiration

indicates how the body reacts to the environmental changes, but also the sweat itseif reflects the physical status of the body. It is realized by monitoring the biochemical materials in sweat through biosensors. Besides, such biochemical materials contain bio-energy which can be utilized by biofuel cells. In fabrications of these wearable electronics for sweat, two key parameters are considered including the mechanical compatibility and the permeability. For the former, conformal electronics with matched mechanical performance to skin are believed to entirely utilize the excreted sweat. For the latter, permeable electronics ensures skin health during long-term wearing.

In the first work, flexible and stretchable sweat biofuel cells were fabricated by using PDMS as the substrate and liquid metal as the conductive materials. The sweat biofuel cell maintained stable output in stretching state, with similar power density to its releasing state. In the second work, we changed PDMS with TPU electrospun mat to enhance the pemeabilty. In addition, we utilized sponge-like carbon electrodes to enlarge the surface area, thus improving the energy output of the biofuel cells. In the third work, we further applied the composite structure of the electrospun mat and sponge electrode to the biosensors for better electrochemical performance.

By taking advantages of liquid metal and electrospun mat, stretchable, permeable and mechanically compatible skin electronics for sweat including the biofuel cells and the biosensors were fabricated. The successful fabrication of such devices holds promise for the advancement of flexible electronics and offers potential support for future smart medical care by mitigating the problem of limited medical resources.

1.4 Outline of the Thesis

This thesis is organized as follows:

Chapter 1 briefly provides background information on the research topic and highlights the current challenges faced in the field of liquid metal-based wearable devices and

energy harvesting. Then, the research objectives and originality of this research project are stated.

Chapter 2 conducts a comprehensive review of existing literature on liquid metal-based wearable devices, including energy harvesting technologies and sensing devices, focusing on their design, fabrication techniques, and applications. It examines the development and applications of sweat monitoring devices, discussing their capabilities in analyzing and monitoring various health parameters. In addition, it summarizes the challenges faced in each of these areas and discusses the prospects and potential advancements in liquid metal-based devices.

Chapter 3 describes in detail the materials and instruments used in the research project, explains the fabrication processes employed to create liquid metal-based biofuel cells and sweat sensors, and details the procedures and protocols followed for the characterization of device properties.

Chapter 4 presents the experimental results and findings regarding the development and performance of the liquid metal-based biofuel cells, analyzes the electrochemical properties and power output of the biofuel cells, and provides the potential applications of the liquid metal-based biofuel cells.

Chapter 5 summarizes experimental results of the air-permeable sweat biofuel cell, presents the improved performance and efficiency of the biofuel cell, and discusses the potential applications of the air-permeable sweat biofuel cell in the field of gesture sensing.

Chapter 6 establishes a profile for human sweat, proposes a testing method for calibrating the sensors used in liquid metal-based sweat monitoring devices, and presents the results of the liquid metal-based sweat monitoring devices.

Chapter 7 summarizes the main findings and conclusions of the entire research project, predicts the prospects and applications of liquid metal-based devices, and underscores their potential impact on addressing the challenges in healthcare and wearable electronics.

Chapter 2 Literature Reviews

2.1 Overview of Liquid Metal Materials

In recent times, liquid metal has emerged as a prominent industrial material across multiple sectors owing to its distinctive characteristics. Its fluid nature at ambient temperatures coupled with its excellent conductivity render it highly suitable for deployment as a conductive material in stretchable devices and circuits. This chapter presents an overview of liquid metal-based devices, encompassing an exploration of the exceptional properties of liquid metal as a conductive material, elucidation of the various fabrication approaches employed for liquid-metal materials, and an analysis of the diverse applications of liquid metal-based devices. Furthermore, the chapter offers insights into the outlooks and challenges associated with liquid metal-based devices.

2.1.1 Overview of Liquid Metal Materials

This subsection discusses the different types of liquid metal materials commonly used in wearable devices, gallium-based alloys here, and explains the properties of liquid metals (e.g., thermal and electrical conductivity, melting point, and even self-healing abilities).

Liquid metal is a term commonly used to describe metals or alloys that are in a liquid state at or close to normal temperature. Examples of liquid metals include gallium (with a melting point of 29.8 ℃), rubidium (with a melting point of 38.89 ℃), cesium (with a melting point of 28.65 ℃), mercury (with a melting point of -38.87 ℃), francium (with a melting point of 27 ℃), gallium-based alloys, and others.[29, 30] However, mercury and amalgam themselves possess high levels of toxicity, low surface vapor pressure, and are easily sublimated.[31] When these substances enter the human body, they can cause irreversible damage to the nervous system and urinary system. [32] Similarly, rubidium, cesium, and francium are metals belonging to the alkaline earth

group, and they exhibit reactive chemical properties.[33] They react violently with water and are highly unstable. In particular, francium and its isotopes are radioactive, making them unsuitable for everyday applications. Likewise, gallium is also a relatively active metal. It is commonly found in various minerals in nature and does not have significant vapor pressure. However, when exposed to oxygen at the ppm level, gallium oxidizes and forms gallium oxide. Nonetheless, this dense layer of gallium oxide acts as a protective barrier, preventing further oxidation. Similarly, gallium indium alloys, which have lower melting points, also form a dense layer of gallium oxide composites on their surfaces. This not only provides protection but also reduces the surface tension of the liquid alloy, enabling it to be patterned into various shapes and adhere better to different materials.[34] Thus, these gallium-indium alloys, along with gallium-indium-tin alloys and others, which possess relatively low melting points, are non-toxic, and exhibit stability, have emerged as viable alternatives with significant practical applications in wearable devices. Table 2.1 presents a compilation of frequently employed liquid metals and their corresponding physical properties.

In this thesis, the liquid metal utilized was gallium indium alloys ($Ga_{80}In_{20}$) with a melting point of 16 ℃.

Table 2.1 Main physical properties of liquid metals [30, 35-40]

	Thermal conductivity $W \cdot m^{-1} \cdot K^{-1}$	Electrical conductivity $S \cdot m^{-1}$	Heat capacity $J \cdot kg^{-1} \cdot K^{-1}$	Density $Kg \cdot m^{-3}$	Surface tension $mN \cdot m^{-1}$	Melting point ^{o}C
water	0.6	$\leq 0.1 \times 10^{-3}$ [c]	4183	1000	72.8	0
EtOH	0.258		2349	1132	48.4	-12.6
Ga	29.4[a]		370[a]	5907[a]	707[a]	29.88
In	36.4[b]		230	7030[b]	550[m]	156.8
Hg	8.34[c]	1.04×10^{6}	139[c]	13546[c]	455[c]	-38.87
Cs	17.4[d]		236[d]	1796[d]	248[d]	28.65

Na	86.9[d]		1380[d]	926.9[d]	194[d]	97.83
K	54.0[m]		780[m]	664[m]	103[d]	63.2
Ag		6.3×10^{7} [e]		10530[e]		962
$Ga_{80}In_{20}$	26.58[e]		403.5[e]	6335[e]		16
$Ga_{75}In_{25}$	31.3[c]	3.3×10^{6} [c]				
$Ga_{67}In_{20.5}Sn_{12.5}$	16.5	3.1×10^{6}		6360		10.5
$Bi_{35}In_{18.6}Sn_{16}Zn_{0.4}$	10.9[c]	7.3×10^{6} [c]		7898		58.3
$Ga_{80}Sn_{20}$	16.7		440	5552		21-39
$Ga_{61}In_{25}Sn_{12}Zn_{1}$	23.2		450	6320		8
$Ga_{68.5}In_{21.5}Sn_{10}$	16.5		/	6440		10
$In_{51}Bi_{32.5}Sn_{16.5}$	21.6		220	8054		63
$Bi_{58}Sn_{42}$	19		201	8560		138

Note: a. 50 ºC; b. 160 ºC; c. 25 ºC; d. 100 ºC; e. 20 ºC; m. Melting point.

2.1.1.1 Melting point

Table 2.1 presents a comprehensive list of the melting points of various conventional liquid metals. Variations in mass ratios of the same constituents can result in significant disparities in alloy properties. Even slight alterations in mass ratios can have pronounced effects on the behavior of the material. The addition of trace elements to the alloy can also impart additional properties. Consequently, the melting point and other attributes of the alloy can be manipulated by modifying the mass ratio of its chemical constituents or by incorporating trace elements to fulfill specific requirements. For instance, gallium-based binary and ternary alloys possess lower melting points compared to gallium metal, remaining in a liquid state at normal temperatures. They are extensively utilized in the biomedical field due to their favorable biocompatibility. Another type of alloy, known as fusible alloys, predominantly consists of bismuth (Bi), lead (Pb), tin (Sn), cadmium (Cd), and indium (In). To align with the growing emphasis on environmentally friendly practices, the usage of toxic and environmentally hazardous metals should be minimized. Consequently, bismuth-based alloys have been

selected instead of lead-based alloys. Among these, the melting point of the $Bi_{35}In_{18.6}Sn_{16}Zn_{0.4}$ alloy can be adjusted to 58.3 ℃. Although this value is slightly higher than the melting point of gallium-based alloys, it remains significantly lower than commonly used metal biomaterials, such as iron, aluminum, and titanium. The moderate melting temperature facilitates the facile achievement of liquid-solid phase transitions in eutectic alloys under mild conditions.

2.1.1.2 Fluidity

Gallium (with a viscosity of 1.2 MPa·s at 77 ℃) exhibits a viscosity similar to that of water (1.002 MPa·s at 20 ℃), which indicates its relatively low viscosity and good fluidity.[41] Liquid metal has low viscosity and can be used as a solvent for pipetting processing, which is beneficial to the application of 3D printing technology and microfluidic technology.[42, 43] However, it is prone to the formation of an oxide layer on its surface, which contributes to the adhesion of gallium-based liquid metal to the substrates. Additionally, the amount of oxide present can impact its viscosity. For instance, introducing extra oxidation of liquid metal by stirring to prepare liquid metal inkcould effectively increase the viscosity of gallium-based liquid metal in printing.[44]

2.1.1.3 Electrical Properties

The conductivity of silver can reach 6.3×10^7 $S\cdot m^{-1}$, but silver can easily cause allergic reactions when used in biomedical electronic devices.[45] It has certain toxicity and is not suitable for invasive wearable devices. In addition, as precious metals, silver, gold, and platinum have high production costs for large-scale industrial production. Thus, more and more researches have been done in recent years to find alternative materials. The conductivity of metallic gallium can reach 2.2×10^6 $S\cdot m^{-1}$, which can be a good substitute for precious metals as conductor materials for wearable devices.

2.1.1.4 Thermodynamic Properties

The thermal conductivity of $Ga_{80}In_{20}$ is 26.58 $W \cdot m^{-1} \cdot K^{-1}$ at 20 °C, which has higher thermal conductivity than water and other inorganic/organic fluids. It cools computer chips efficiently and is therefore used as an excellent coolant and thermal interface material in electronic processing.[46] At the same time, due to its fluidity and high thermal conductivity, liquid metal is also used as a microwave electrode, which can transmit energy to kill tumors while also transferring heat to the outside world, thereby avoiding overheating of nearby tissues and affecting normal tissue cells.[47, 48]

2.1.1.5 Chemical Stability

It has been observed that when gallium is exposed to air with a certain humidity, it undergoes oxidation. Research has indicated that gallium is the primary element responsible for oxidation in GaInSn alloy. Under oxygen conditions, a dense oxide film forms on the surface of the liquid metal. This gallium oxide film can be effectively eliminated by the use of acidic or alkaline solutions, such as hydrochloric acid or sodium hydroxide.[49] When aluminum (Al) is placed in contact with a sodium hydroxide solution, a reaction occurs that releases hydrogen gas.[50] Experimental findings have revealed that when an aluminum sheet is attached to EGaIn or Galinstan in a NaOH solution, the liquid metal infiltrates the aluminum and activates a reaction between aluminum and the NaOH solution.[50] This accelerates the generation and release of hydrogen gas. Additionally, a galvanic cell is formed based on this reaction system, leading to mutually beneficial bipolar electrochemical reactions. This system has potential applications in self-powered micro-robots or soft robots, providing a novel approach for the development of intelligent biomedicine in the future.

2.1.1.6 Magnetism

Typically, metals and their alloys with low melting points do not possess the inherent property of magnetism. While liquid metal itself is non-magnetic, it can exhibit peculiar behavior in the presence of specific conditions under a magnetic field. In this study, researchers positioned a gallium-based alloy within a pair of concentric ring electrodes,

submerged the liquid metal and the ring electrodes in a solution of NaOH, and placed a permanent magnet beneath the container. Through experimentation, it was observed that the liquid metal ball could be induced to undergo centrifugal rotation around the central electrode. Notably, the rotation speed escalated with an increase in voltage and was modulated by the concentration of the sodium hydroxide solution. Additionally, it was observed that when the volume of the liquid metal reached a certain threshold, the rotation speed did not correspondingly diminish[51]. Leveraging the influence of this magnetic field on liquid metal may pave the way for the development of liquid metal motors in medical equipment, soft robots, and other related domains.

2.1.1.7 Biocompatibility

Liquid metals are gaining popularity due to their unique characteristics. However, the well-known liquid metal mercury has limitations in its application due to its high neurotoxicity, low vapor pressure, and susceptibility to causing environmental pollution during processing and production. To overcome these limitations, low melting point alloys consisting of Ga, In, Sn, and Bi elements have emerged as potential biomedical materials. Gallium compounds, for example, have received significant attention in the medical field due to their anti-inflammatory, antibacterial, and immunosuppressive effects in animal models of human diseases.[52, 53] Gallium and gallium nitrate have been utilized as diagnostic and therapeutic agents for cancer, calcium metabolism disorders, and bone metabolism disorders.[47, 54] Tin, on the other hand, has historical use in food and beverage containers and is an essential trace element for the human body. Indium plays a major role in electrical engineering, with safety standards set by the Japanese Association. In clinical applications, gallium-indium alloy has been used as a biocompatible dental filling biomaterial, demonstrating its biological safety.[55] Bismuth, considered a green and clean material, is used in industry as a substitute for toxic lead. Pepto-bismol, a popular drug, is based on bismuth compounds. Furthermore, experiments involving the burial of BiInSnZn alloy samples under the skin of mice for different durations demonstrated the alloy's long-term

biocompatibility.[56] In conclusion, low melting point alloys composed of gallium and bismuth exhibit favorable biocompatibility and have found applications in the biomedical field.

2.1.2 Brief Introduction of Liquid Metal-Based Wearable Devices

This subsection introduces the concept of liquid metal-based wearable devices, highlighting their unique properties and advantages over traditional wearable devices, and explaining the growing demand in various applications, such as healthcare, sports, entertainment, and so forth.

Liquid metal generally refers to an element or alloy with a melting point lower than or close to the room temperature.[57] This unique property enables liquid metal to flow like water, offering numerous benefits for flexible electronics. These characteristics distinguish liquid metal-based wearable devices from traditional ones, including their stretchability, conformability to the biological interfaces, and implantability.

Stretchability is the most prominent advantage of liquid metal-based wearable devices. Unlike traditional devices that require physical structures, such as island bridge structures or origami techniques, liquid metal-based wearable devices on which liquid metal placed on the substrate by additive technology can reach a strain of over 100 % (Figure 2.1a).[12, 57, 58] And with the use of ultra-stretchable substrates, strains of over 1000% are possible.[59, 60]

Conformability is another advantage of liquid metal-based wearable devices. Certain wearable devices need to conform to the skin or biological interfaces to fulfill their functions, such as acquiring physiological electrical signals. Liquid metal-based wearable devices can easily conform to the skin or other tissues (Figure 2.1b)[61-63]. Such conformal liquid metal ECG sensors could even detect the U wave which was ignored by the commercial sensors. The U waves can be associated with the clinical syndromes of the Torsade de Pointes (TdP), [64] stenoses of the left anterior descending coronary

artery,[65] and the arrhythmic risk[66].

Moreover, the bio-compatible and bio-safe properties of liquid metals are important to its applications. Traditional metal materials, such as Cu, Ni, and Ag, can trigger allergies and cause inflammation. [67] Liquid metals, as alternative metallic materials, can avoid these issues. To assess the biocompatibility of liquid metals, scientists evaluated the interaction between liquid metals and biological system at different levels. At the cellular level, liquid metals could be co-cultured with cells and did not affect the morphology and viability of cells.[57] In addition, it has been reported that Ga-based liquid metals can have influence on growth and development of cells. At the tissue level, researchers have observed the application of liquid metals or liquid metal-based devices through pathological sections to evaluate their biocompatibility. Researchers reported that liquid metal-based electronic vessels were successfully implanted into animal models for up to three months (Figure 2.1c). [68-70] At the individual level, physical signs, feelings, and behavior of subjects, in conjunction with tissue-level characterization, have been utilized to evaluate the impact of liquid metal-based devices on individuals. After wearing the liquid metal-based devices for two days, there were no obvious inflammation and irritation on skin.[61, 68] Despite there are numerous articles demonstrate the biocompatibility of liquid metals, further investigations and advancements are still required to fully understand the interaction between liquid metals and biological systems.

The fabrication of liquid metal-based wearable devices primarily relies on additive technology, which will be discussed in the next section. Here, we focus on the advantages of liquid metal within additive technology (Figure 2.1d).[71] (1) Easy patterning: Liquid metals exhibit a liquid/solid coexistence, with metallic oxides assisting in patterning on the substrate. Alternatively, liquid metal particles can be used to create conductive ink patterns on substrates using current industrial printing technologies. (2) Easy dispersion: With a viscosity similar to water, liquid metal can be dispersed into solvents through methods such as sonication, stirring, or spraying. (3)

Easy recycling: Dispersed liquid metal particles can be treated in acid or alkaline solutions to dissolve the surface metal oxide shell, allowing them to merge back into bulk metal. This enables the fabrication of new liquid metal ink. Thus, in terms of additive fabricating technology, the application of liquid metal materials also has irreplaceable advantages.

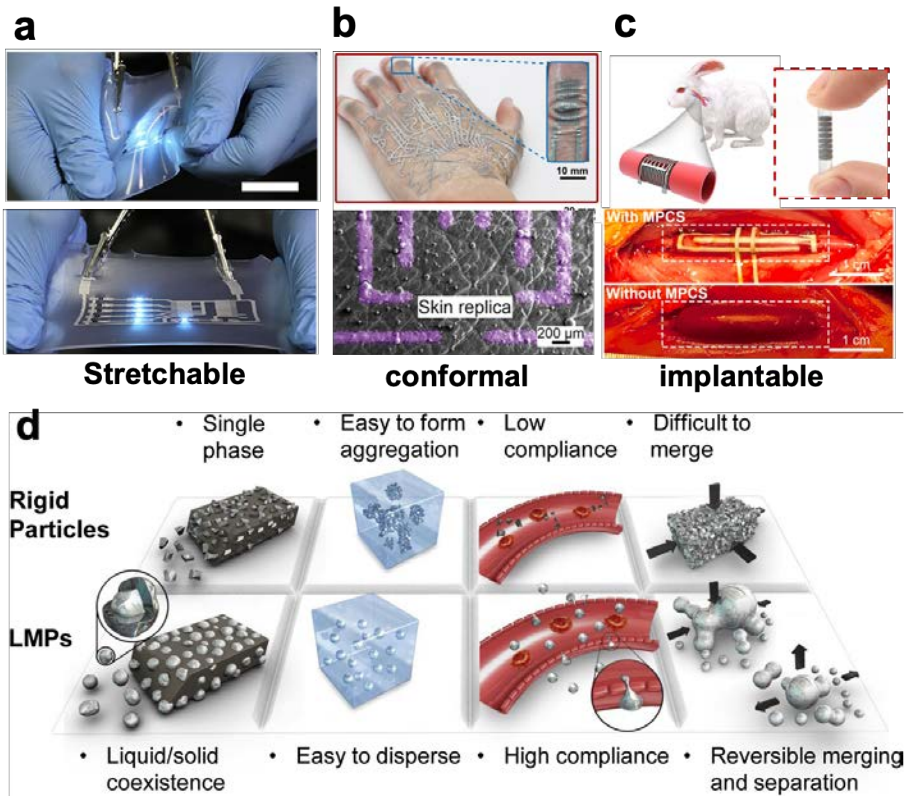

Figure 2.1 Properties and advantages of liquid metal-based wearable devices; liquid metal-based devices are (a) stretchable [12, 57], (b) conformal [72], and (c) implantable [69]; (d) properties of utilizing liquid metal particles over traditional conductive particles. [71]

Liquid metal-based wearable devices have emerged as promising technologies with diverse applications in various fields. Their unique characteristics such as stretchability, conformance, and implantability make them particularly suitable for applications in the biomedical field, among others. Here, we explore the applications of liquid metal-based wearable devices and the potential impacts they can have in these areas, such as

healthcare, prosthetics and rehabilitation, sports training, virtual reality (VR), human-machine interfaces (HMI), and motion capture (Figure 2.2).

Liquid metal-based wearable devices have significant potential in healthcare. They can be used for monitoring vital signs, such as heart rate, body temperature, and blood pressure.[6, 58, 73, 74] These devices can provide continuous, non-invasive monitoring, enabling early detection of health issues and improved patient care. Additionally, liquid metal-based sensors can be used for drug delivery or microfluidic systems for lab-on-a-chip diagnostics.[71, 75]

Liquid metal-based wearables offer advancements in the field of prosthetics and rehabilitation.[29, 39] By conforming to the user's body, these devices provide a more comfortable and natural fit, enhancing mobility and control. They can also incorporate sensors to detect muscle signals and provide more precise control and feedback for prosthetic limbs.[76, 77] This technology holds the potential to greatly improve the quality of life for individuals with limb loss or disabilities.

Liquid metal-based wearables can be used in sports training to monitor biomechanical movements, track performance metrics, and provide real-time feedback to athletes.[78] These devices can measure joint angles, muscle activity, and other relevant parameters to help optimize training routines, prevent injuries, and enhance athletic performance. The stretchability of liquid metal enables a comfortable fit during intense physical activity.

Liquid metal-based wearables can enhance the immersive experience in VR systems.[79] By capturing precise hand movements and gestures, these devices enable users to interact intuitively with virtual environments. This technology allows for more realistic and responsive interactions and has the potential to revolutionize the gaming and entertainment industries.[80]

Liquid metal-based wearables offer exciting possibilities for intuitive HMI. For example, recording EEG signals can detect and interpret gestures, movements, and even emotional responses, enabling seamless interaction between humans and machines.[81] [82, 83] This technology has applications in areas such as robotics, smart homes, and advanced control systems.

Liquid metal-based wearables can be used for motion capture in various fields, including animation, sports analysis, and rehabilitation. By accurately tracking and recording movements, these devices allow for detailed analysis and replication of human motion. [63, 84] This technology is instrumental in areas where precise movement data is required for research, training, or entertainment purposes.

In conclusion, liquid metal-based wearable devices have diverse applications across several fields, with significant potential in healthcare, prosthetics and rehabilitation, sports training, virtual reality, human-machine interfaces, and motion capture. These devices offer unique advantages, such as stretchability and conformance, enabling comfortable and accurate data collection. Continued research and development in this area will likely lead to further advancements and expanded applications in the future.

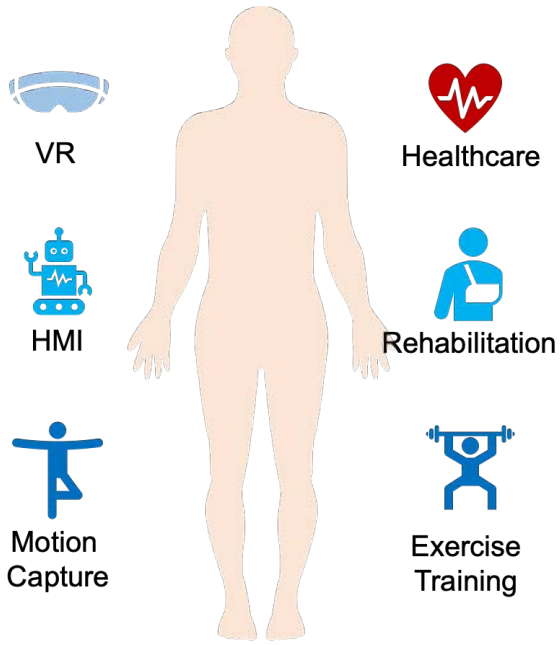

Figure 2.2 Applications of liquid metal-based wearable devices

2.1.3 Fabrication Methods for Liquid Metal-Based Wearable Devices

This subsection discusses the various fabrication techniques employed to create liquid metal-based wearable devices, such as screen printing, direct writing, 3D printing, microfluidic perfusion, and so forth. According to the various fabrication methods, the comparison of advantages and limitations of each fabrication method is summarized.

2.1.3.1 Screen Printing

Screen printing is a traditional method for manufacturing flexible circuits, where a designed circuit pattern is printed on a screen using a laser (Figure 2.3a).[12, 57, 58, 60, 62, 63, 70, 73, 74, 78, 81, 84-86] Subsequently, a liquid metal ink is applied to the screen, which allows for the printing of a patterned liquid metal circuit. This technique enables the production of flexible circuits with relatively high resolution (50 μm) and high throughput (2000 $pcs \cdot h^{-1}$).[12, 81] In comparison to inkjet printing or digital printing, screen printing does not require a customized printer and is more cost-effective, although it necessitates the customization of screens for different circuit patterns. Additionally, screen printing has less stringent requirements for liquid metal preparation conditions and does not necessitate reaching the boiling point like a thermoelectric inkjet printer. This printing method allows for the industrial production of various complex electronic patterns, including functional circuits and general art drawings, on flexible or rigid substrates with differing surface morphology within a short period of time.

2.1.3.2 Spray Coating

Spray coating is a versatile surface coating technique that involves the deposition of a thin layer of material onto a substrate using a spray nozzle or gun (Figure 2.3b).[61] Spray coating offers several advantages, such as uniform coverage, precise control of coating thickness, and the ability to apply coatings to complex shapes and surfaces. For instance, liquid metal ink was sprayed on the wrist to form a conformal e-tattoo to monitor ECG

signals. Such e-tattoo could collect the U wave of ECG signals which has medical meanings but usually being ignored in commercial ECG sensors.

2.1.3.3 Microfluidic Perfusion

The microfluidic channel method refers to the use of patterned microfluidic chips to prepare flexible circuits (Figure 2.3c).[43, 87, 88] Bulk liquid metal is directly injected into the channels of the microfluidic chip to achieve circuit patterning. This method can reach the accuracy of liquid metal patterns (<100 μm). Furthermore, microfluidic perfusion can used to process liquid metal conductive ink. By changing the rheological parameters, the size of liquid metal droplets could be controlled.[89] For this method, the microfluidic channels should be designed and molded in advance.[90] In addition, the rheological properties should be considered.

2.1.3.4 Direct Writing

Compared with traditional direct painting or writing, mechanical printing methods with digital control make liquid metal patterns more precise and quantitative. Researchers have built and demonstrated a multifunctional desktop liquid metal printer that can print both flat circuits and 3D metal objects. [91] The body consists of a syringe, nitrogen tube, pressure controller, workbench, three-axis orbits of motion, and various electronic graphics that can be printed through computer software.

2.1.3.5 3-D Printing

3D printing is a technology that constructs objects by printing them layer by layer until the 3D structure is built. Liquid metal can be printed directly or mixed with another polymer (Figure 2.3d). [78] The formation of an oxide layer on the surface of liquid metal plays a crucial role in determining the shape of the liquid metal pattern. When printing in either the X-axis or Y-axis direction (parallel to the substrates), the shear force exerted by the nozzle must be sufficient to exceed the yield stress of the oxide, thereby

causing its rupture. Conversely, when printing in the Z-axis direction (perpendicular to the substrate), the tension forces acting on the oxide result in its breakage. The resolution of liquid metal patterns is influenced by several factors including nozzle size, printing rate, and even the height of the nozzle.[92] Furthermore, mixing liquid metal with polymer to fabricate composite ink for 3D printing is another strategy. One of the advantages of this method is that the viscosity and rheological behavior can be adjusted by the molecular mass and the concentration of the polymer solution.[87]

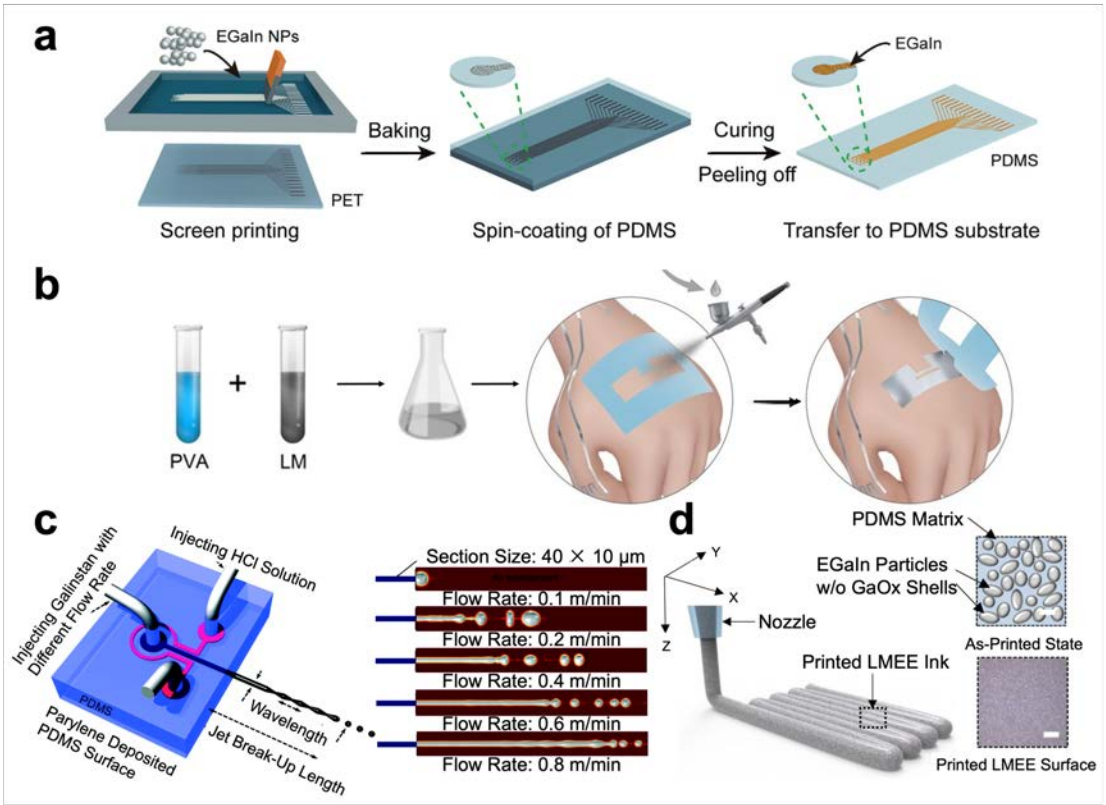

Figure 2.3 Fabrication methods for liquid metal based wearable devices; (a) screen printing[88]; (b) spray coating[61]; (c) microfluidic perfusion[43]; (d) 3-D printing[87].

2.1.4 Application of Liquid Metal-Based Wearable Devices

Liquid metal-based wearable devices have gained significant attention due to their unique properties like stretchability, conformance, and implantability. These devices have shown immense potential in various fields, including biosensors, biomedicine,

energy, robotics, and displays (Figure 2.4). In this section, we will explore the applications and advancements of liquid metal-based wearable devices in each of these areas.

2.1.4.1 Liquid Metal-Based Biosensors

Liquid metal-based strain sensors can detect and measure the deformation or strain applied to them. The tensile strain of the sensor is generally determined by the resistance change (Figure 2.4a).[57] These sensors based on liquid metal are highly stretchable (200 – 1000%)[57, 59, 60, 86] and can conform to irregular surfaces, making them suitable for monitoring body movements or external forces.[93]

Liquid metal-based pressure sensors can measure changes in pressure or force applied to them. The pressure sensors are mainly realized by determining the relationship between the output potential of triboelectric or piezoelectric materials to the input pressure (Figure 2.4b)[93], because such materials are sensitive to mild pressure. In addition, resistance change and capacitive change are also utilized to measure pressure.[94] They find applications in medical monitoring, such as measuring blood pressure or respiratory rate, tactile touch monitoring, as well as in sports and fitness devices.[95]

Liquid metal-based electrophysiological sensors can detect and record electrical signals generated by the body, such as electrocardiograms (ECG) or electromyograms (EMG) (Figure 2.4c).[68] These sensors are used in wearable devices for heart monitoring, muscle activity monitoring, and brain-computer interfaces.[61, 81, 83, 84]

Liquid metal-based biomarker sensors can detect specific biochemical parameters on the stretchable bio-interface, such as glucose levels, lactate, dopamine, or pH (Figure 2.4d).[73, 74, 96] These sensors have potential applications in healthcare for monitoring diseases, tracking athletic performance, and managing chronic conditions like diabetes.[97] Due to the chemical properties of the liquid metal, such biosensors should

encapsulate liquid-metal conductors properly and utilize other electrochemical stable materials for electrodes to keep the sensors from the electrochemical inference. To mitigate electrochemical interference from liquid metal itself, it is essential for biosensors to ensure appropriate encapsulation of liquid-metal conductors and incorporate other electrode materials with electrochemical stability.

2.1.4.2 Liquid Metal-Based Biomedicine

Except for health monitoring relative biosensors, liquid metal-based wearable devices get further applications in biomedicine, such as vascular stent, contact lens, wound dressing, and so forth.

Liquid metal-based electronic blood vessels are a pioneering biomedical application for liquid metal-based implantable devices for cardiovascular diseases (Figure 2.4e). [70, 98] Such electronic vessels are used to restore blood flow in narrowed or blocked blood vessels. These electronic vessels not only offer excellent biocompatible and conformal artificial stents to replace the pathological vessel, but also provide an extra electrical field for accelerating the repair of blood vessel.

Liquid metal-based contact lenses can be used for ocular drug delivery or as biosensors for monitoring various eye conditions. These lenses can release drugs directly onto the eye[62] and provide real-time monitoring of intraocular pressure or tear glucose levels[16]. For drug delivery, the patterned coil of liquid metal on the contact lens can generate an electric field, thereby enabling electroporation on membranes to enhance drug delivery (Figure 2.4f).

Liquid metal-based wound dressings have antimicrobial properties and can facilitate wound healing by promoting tissue regeneration and controlling infection (Figure 2.4g).[52, 53, 68] Except for being conformal to irregular wound shapes and electrically-driven delivering therapeutic agents, the liquid metal-based wound dressings can release hydrogen for antibacterial activities.[53]

2.1.4.3 Liquid Metal-Based Energy Supplies

Liquid metal-based materials, such as gallium-indium alloys, can be used as electrode materials for supercapacitors.[99] These supercapacitors offer high energy storage capabilities (as high as 12.4 mF cm^{-2}), periodic stretchability (cyclic tensile strain 30%), and long cycle life (>4200 charging and discharging cycles), making them suitable for stretchable energy storage devices (Figure 2.4h).

Liquid metal-based energy harvesting can convert mechanical, thermal, or other energy from the human body into electrical energy. These devices can power wearable electronics or recharge energy storage devices. Liquid metal-based energy harvesting devices will be further discussed in the next section. Here, take near-field communication (NFC) technology as an example (Figure 2.4i). The NFC utilizes inductive coupling between two loop antennas to exchange data or supply power. Liquid metals, no matter bulk metals or metal particle composites, are highly compatible with additive technologies (such as screen printing, dip coating, 3-D printing, and so forth), thereby enabling pattern antennas on substrates at low cost. Thus, liquid metal-based antennas are widely spread in communication and energy harvesting applications.

Liquid metal-based batteries (gallium-based alloys) offer a stretchable battery without the risks of flaming. [100, 101] Figure 2.4j shows a gallium-air battery can operate at room temperature and ambient environment with electrochemical performance of 0.383 $mW \cdot cm^{-2}$ at 1.5 V. The whole cell reactions are shown as:

$$4Ga \longrightarrow 4Ga^{3+} + 12e^{-} \qquad (2.1)$$

$$3O_2 + 6H_2O + 12e^{-} \longrightarrow 12\,OH^{-} \qquad (2.2)$$

The tensile strain of such gallium-air battery is 100% with remained discharge performance of 98.87 %.[100] In addition, the EGaIn-MnO_2 battery system has been

proved as well with the specific capacity of 140.74 $mAh \cdot g^{-1}$.[102] These batteries have the potential to power wearable devices and have application on stretchable biomedical devices.

2.1.4.4 Liquid Metal-Based Robotics

Liquid metal-based materials, such as gallium alloys, can be integrated into soft robotics for flexible and stretchable sensors and actuators. Multi-layer liquid metal-based sensors with multi-degree of freedom could precisely capture the motion of the subject. By transmitting such motion data, the robotic hand could repeat the motion from the subject (Figure 2.4k). These liquid metal-based sensors which emphasize the stretchable and conformal properties enable robots to perform delicate tasks, opening new possibilities in robotics applications.[24, 39, 103] Furthermore, the fluidity, thermal conductivity, electrical conductivity, and magnetism (at specific condition) of liquid metals can also actuate soft robots, which will be not discussed here.

2.1.4.5 Liquid Metal-Based Displays

Liquid metals were utilized in stretchable displays and photonic electronics (Figure 2.4 l).[34, 104] By using the dip-coating method or screen-printing method, the liquid metal can be coated on stretchable substrates to serve as current collectors. The electroluminescent materials (i.e., ZnS powder) can be mixed with silicone polymer to realize the stretchable electroluminescent layer. Such liquid metal-based electroluminescent devices are assembled to the textiles to realize functional clothing.

In conclusion, liquid metal-based wearable devices offer a wide range of applications in biosensors, biomedicine, energy, robotics, and displays. Their unique characteristics, including stretchability, conformance, and implantability, make them suitable for various wearable applications. Continued research and development in this field hold the potential for further advancements and innovative applications in the future.

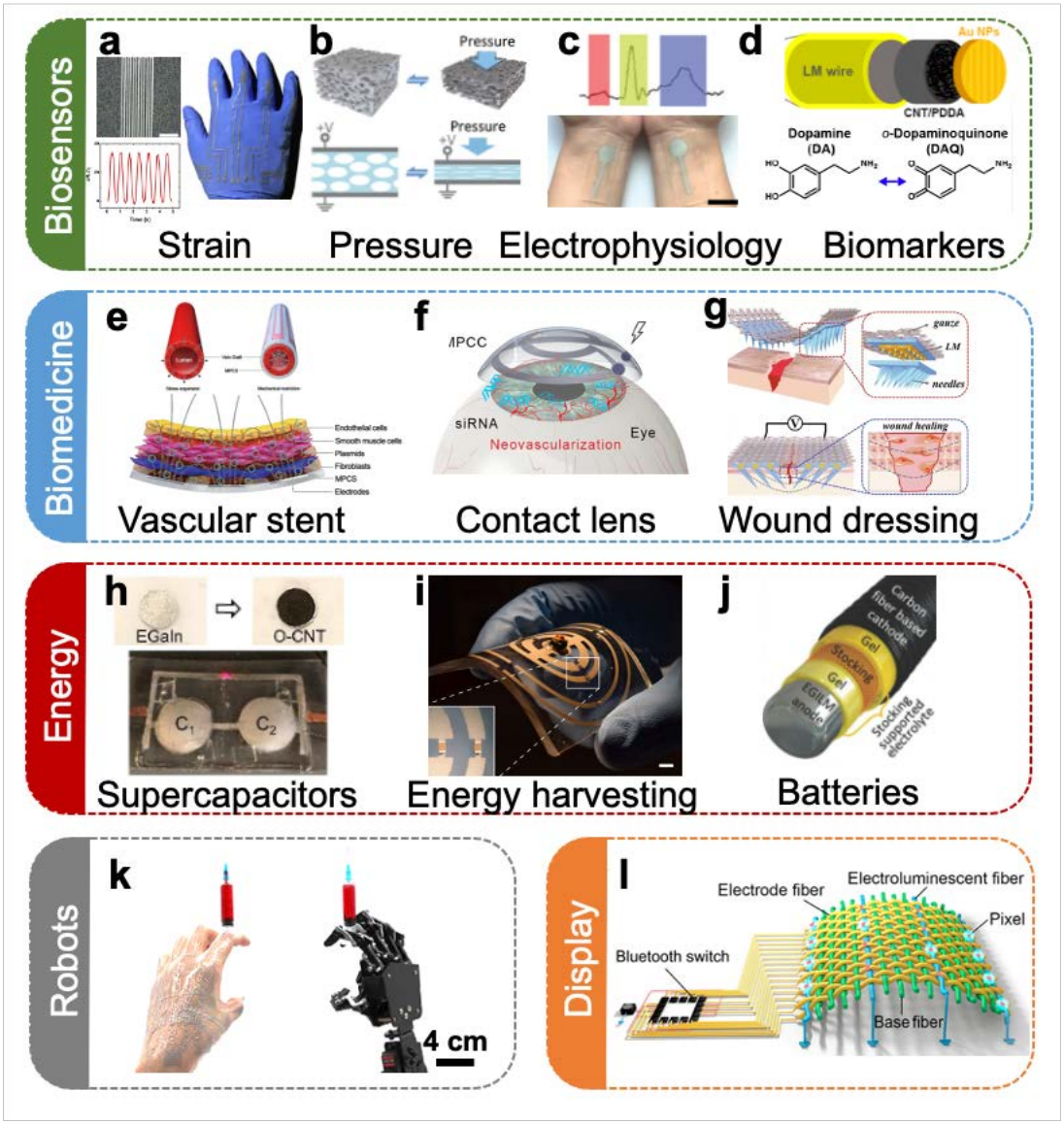

Figure 2.4 Applications of liquid metal-based wearable devices;[57] (a) strain sensors; (b) pressure sensors;[93] (c) electrophysiological sensors;[68] (d) biomarker sensors;[97] (e) vascular stent;[69] (f) contact lens;[62] (g) wound dressing;[105] (h) supercapacitors;[99] (i) energy harvesting technologies;[106] (j) batteries;[100] (k) robots;[63] (l) displays.[34]

2.2 Liquid Metal-Based Energy Harvesting Devices

This section provides a comprehensive review of liquid metal-based energy harvesting devices, consisting of three subtopics: (1) a concise introduction to energy harvesting devices, (2) an overview of wearable biofuel cells, and (3) the challenges and prospects of liquid metal-based energy harvesting devices. By comparing diverse energy-

harvesting technologies, the advantages of employing liquid-metal materials into energy harvesting devices can be delineated. Additionally, considering biofuel cells as a cleaning energy source, their integration into liquid metal-based devices is explored. Furthermore, the last subsection examines various obstacles associated with the future implementation of liquid metal in biofuel cells.

2.2.1 Brief Introduction of Energy Harvesting Devices

Energy harvesting technologies have made great contributions to self-powered wearable devices. This section provides a brief overview of energy harvesting devices, exploring their fundamental concepts, principles, and working mechanisms. It introduces the applications of liquid metal in various types of energy harvesting technologies, including radio frequency (RF), photovoltaic, thermoelectrical, piezoelectric, triboelectric energy harvesting, and biofuel cells (Figure 2.5).

RF technology has been widely used in powering wearable devices. At an ambient environment, it provides power density in the range from 0.2 $nW \cdot cm^{-2}$ to 1 $\mu W \cdot cm^{-2}$, which is relatively lower than other energy harvesting technologies.[107, 108] Thus, there are several modules cooperating to harvest and storage the energy, then to power wearable devices. For example, the antenna (size, number, etc.), rectifier, voltage multiplier, and frequency band, so forth are affecting the efficiency.[109] As mentioned above, NFC based on RF technology (with 13.56 MHz RF and RF identification tags) takes advantage of inductive coupling between two printing antennas to power wearable sensors and realize data exchange. Researchers used a liquid metal-based antenna to communicate the precoding information stored on NFC tags with mobile phones (Figure 2.5a)[110]. Interestingly, the liquid metal-based antenna not only reveals its flexibility and conformal ability, but also shows its recycling ability. The patterned liquid metal can leave the substrate by treating it with acidic or alkalic solutions and merge with bulk metal for recycling, which is another irreplaceable property of liquid metal-based devices. Nevertheless, the NFC technology is limited by the working

distance between the RF source and antennas (< 3.9 inches for electronic devices)[111]. Thus, liquid metal-based antenna contributes to RF energy harvesting technology mainly in size, shape, numbers, and conformal to bio-interface.

Both triboelectric and piezoelectric energy harvesting technologies convert mechanical energy into electrical energy with high output potential (Figure 2.4b, e)[112, 113]. Piezoelectric devices typically comprise a sandwich-like structure, consisting of a layer of piezoelectric materials positioned between two vertically oriented electrode layers. Application of external force induces deformation between dipoles in the piezoelectric layer, resulting in the accumulation of varying charges on the opposing electrodes. However, the energy conversion process in piezoelectricity necessitates continuous external force stimulation. The power density of piezoelectric devices is in the range of 0.1 $\mu W \cdot cm^{-3}$ to 506.7 $mW \cdot cm^{-3}$.[114] In particular, the PVDF can reach the maximum power density of 506.7 $mW \cdot cm^{-3}$. Researchers reported that by adding liquid metal particles inside PVDF nanofibers, the surface potential of nanofiber decreased from -0.55 V to -0.67 V which enabled more charge transferring. Such PVDF/Galinstan nanofibers had the highest output potential of 1680 V and a maximum power density of 2.4 $mW \cdot cm^{-2}$.[115]

In contrast, triboelectric harvesting technology offers a wider selection of materials and simpler preparation methods compared to piezoelectric energy harvesting technology. In general, triboelectric materials encompass polytetrafluoroethylene (PTFE), PDMS, Kapton, polyethylene terephthalate (PET), nylon, and various metallic materials.[116] The power density of triboelectric devices is in the range of 39.3 $\mu W \cdot cm^{-2}$ to 4.3 $mW \cdot cm^{-2}$.[114] The addition of liquid metal in the triboelectric devices contributes to the electrical connection under the deformation of conductive materials. By using Galinstan as stretchable electrodes and silicone as a triboelectric layer and encapsulation, researchers invented a liquid metal-based triboelectric nanogenerator (TENG) which realized a tensile strain of 300 % and generated a OCP of 354.5 V and a power density of 8.43 $mW \cdot m^{-2}$.[113]

Photovoltaic energy harvesting technology is a hot topic in the energy field because solar energy is the most abundant resource surrounding human beings. The solar irradiance at earth is in a range of 60-250 $W \cdot m^2$ every year. By absorbing sunlight, photovoltaic materials can generate electron-hole pairs or excitons. Then, by separating the charge carriers with opposite types to the external circuit to generate current.[117] Currently, the efficiency of the solar cell reached over 20 %, specifically, 29.1 ± 0.6 % for GaAs thin film cell, 21.6 ± 0.6 % for perovskite cell, and 26.7 ± 0.5 % for Si crystalline cell.[118] To realize stretchable solar cells, one of the strategies is coating photovoltaic materials on the pre-strain substrates. Liquid metal, EGaIn, was used to replace traditional evaporated Al to overcome the crack upon releasing of the pre-strain (Figure 2.5c)[119]. Another example of applying liquid metal in stretchable solar cells is to fabricate transparent, stretchable and conductive electrodes, liquid metal grid, via 3-D printing technology. The liquid metal grid, characterized by a line width of 5 μm and a spacing of 100 μm between each line, exhibited a transmittance of 90.1% at 500 nm wavelength and a sheet resistance of 1.7 $\Omega \cdot sq^{-1}$.[120]

Thermoelectric energy harvesting devices operate by converting thermal energy into electrical energy through the implementation of a temperature gradient across an electric couple. The electric couple consists of two materials, an n-type material responsible for electron transport and a p-type material responsible for hole transport. As a result of this temperature gradient, the charge carriers within the electric couple undergo diffusion from the hotter region to the colder region, consequently generating an electric potential.[121] The power density of thermoelectric devices is in the range of 0.1 $\mu W \cdot cm^{-2}$ to 3.8 $mW \cdot cm^{-2}$.[114] The liquid metals are good thermal conductivity thereby applying on carrier collectors (Figure 2.5d).[122] The wearable thermoelectric devices take advantage of the temperature gradient of body and indoor environment and harvest up to 5 mW energy during 8 hours of wearing.[123] Researchers invented a liquid metal-polymer composite which remains stretchability at -80 ℃ due to its supercooling properties. Such liquid metal-polymer composite combined with thermoelectric generators could power heart rate monitors in cold weather

conditions.[124]

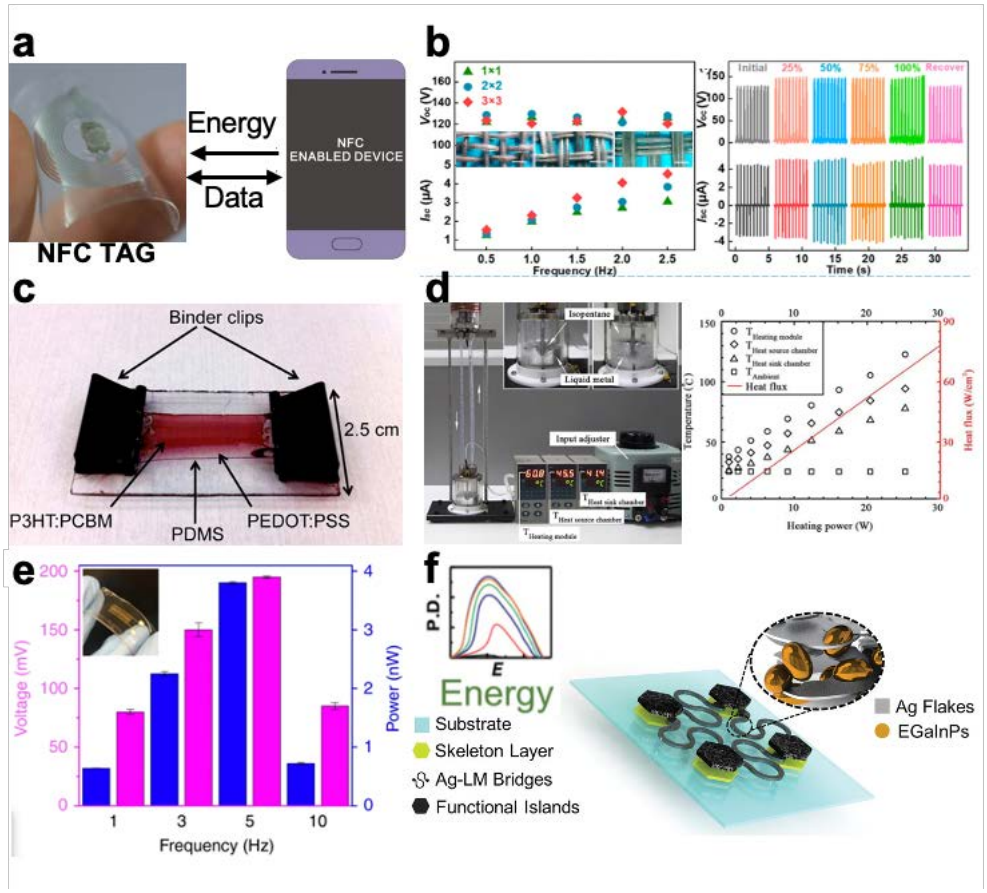

Figure 2.5 Liquid metal-based energy harvesting devices; (a) NFC;[110] (b) triboelectric energy harvesting[113]; (c) photovoltaic energy harvesting;[119] (d) thermoelectric energy harvesting;[122] (e) piezoelectric energy harvesting[112]; and (f) biofuel cells[125].

Biofuel cells (BFCs) are green and environmental-friendly energy that converse biological energy into electrical energy. Biofuel cells are mainly divided into microbial biofuel cells. In addition, biofuel cells based on subcellar units, photosynthetic protein and photosynthetic apparatus, have also been reported.[126, 127] In comparison to microbial BFCs, enzymatic BFCs exhibit greater efficacy in fuel transportation, catalytic activity, and selectivity. Consequently, wearable BFCs, specifically enzymatic BFCs, offer power densities ranging from 20 $\mu W \cdot cm^{-2}$ to 20 $mW \cdot cm^{-2}$ (Table 2.2). Due to these characteristics, they are considered optimal and sustainable options for flexible wearable electronic devices. Researchers took advantage of the conformal ability of

liquid metal to enhance the conductive connection between rigid functional electrodes and soft flexible silver circuits (Figure 2.5f).[125]

Liquid metal plays a crucial role in energy harvesting technology due to its unique properties. Its stretchability makes it an excellent choice for stretchable and wearable energy harvesting devices, as it can withstand and accommodate mechanical deformations without affecting its conductive properties. Additionally, the conformability of liquid metals allows for enhanced connectivity between rigid functional materials and soft current collectors, promoting efficient energy transfer. In thermoelectric harvesting devices, the exceptional thermal conductivity of liquid metal makes it invaluable. Its high thermal conductivity facilitates efficient heat transfer between the hot and cold regions, maximizing the conversion of thermal energy into electrical energy. Another notable characteristic of liquid metal-polymer composite is its supercooling properties. This attribute enables its applications in freezing environments, where it can maintain its liquid state below its normal freezing point. This property opens opportunities for energy harvesting technologies to operate in extremely cold conditions, where traditional materials may be ineffective. Overall, the stretchability, conformability, thermal conductivity, and supercooling properties of liquid metals make them a versatile and indispensable component in various energy harvesting devices.

2.2.2 Overview of Biofuel Cells

This section delves into the analysis and exploration of wearable biofuel cells. It discusses their construction, operation, and performance characteristics, highlighting the advantages and limitations of utilizing liquid metal as a key component in biofuel cell systems. The section also presents case studies and research findings related to the application of liquid metal-based biofuel cells in practical settings.

The comparison of the power output performance of BFCs with other energy harvesting technologies reveals the research worth of the BFCs. As mentioned above, the

triboelectric devices have power density in a range of 39.3 $\mu W \cdot cm^{-2}$ to 4.3 $mW \cdot cm^{-2}$, RFs are from 0.2 $nW \cdot cm^{-2}$ to 1 $\mu W \cdot cm^{-2}$, piezoelectric devices are from 0.1 $\mu W \cdot cm^{-3}$ to 506.7 $mW \cdot cm^{-3}$, thermoelectric devices are from 0.1 $\mu W \cdot cm$-2 to 3.8 $mW \cdot cm^{-2}$, and the BFCs are from 20 $\mu W \cdot cm^{-2}$ to 20 $mW \cdot cm^{-2}$. For the power density, the solar cells and the piezoelectric generators rank high, but are limited by the continuous extra stimulations, lights or machinal force. Thermoelectric generators and BFCs are driven by spontaneous biological energy thereby attracting attention. Wearable BFCs generate higher power density than thermoelectric generators, thereby this thesis focuses on wearable BFCs.

Enzymatic biofuel cells (EBFCs) offer the advantage of utilizing renewable and sustainable fuels, which contain diverse chemical substances that can provide insights into the health issues of an individual, enabling non-invasive metabolic monitoring. Various biofluidic sources, such as sweat, tears, saliva, and interstitial fluid (ISF), have been explored as fuels for EBFCs. The concentration of metabolites present in these biofluids directly impacts the performance and output power of EBFCs, leading to diverse applications depending on the chosen fuel source. Despite the capability of EBFCs to generate energy ranging from a few $\mu W \cdot cm^{-2}$ to several $mW \cdot cm^{-2}$ (as indicated in Table 2.2), they face challenges regarding limited power generation rate, low open circuit voltage, and short lifespan. Consequently, further research on BFCs is necessary to address these issues and enhance their performance.

Figure 2.6 illustrates the operational mechanism of a representative EBFC. In this configuration, the fuel undergoes catalysis at the anode, resulting in the generation of electrons and oxidized fuel. These electrons are then transported or mediated to the electrode surface, subsequently being conveyed to the cathode through the external circuit. At the cathode, the oxidant is subsequently catalyzed and reduced, thereby consuming the generated electrons. To maintain charge equilibrium within the electrolyte, protons either directly migrate or move through a selectively permeable

membrane toward the cathode. Depending on the different generations of EBFCs being designed, the presence of mediators can be optional.

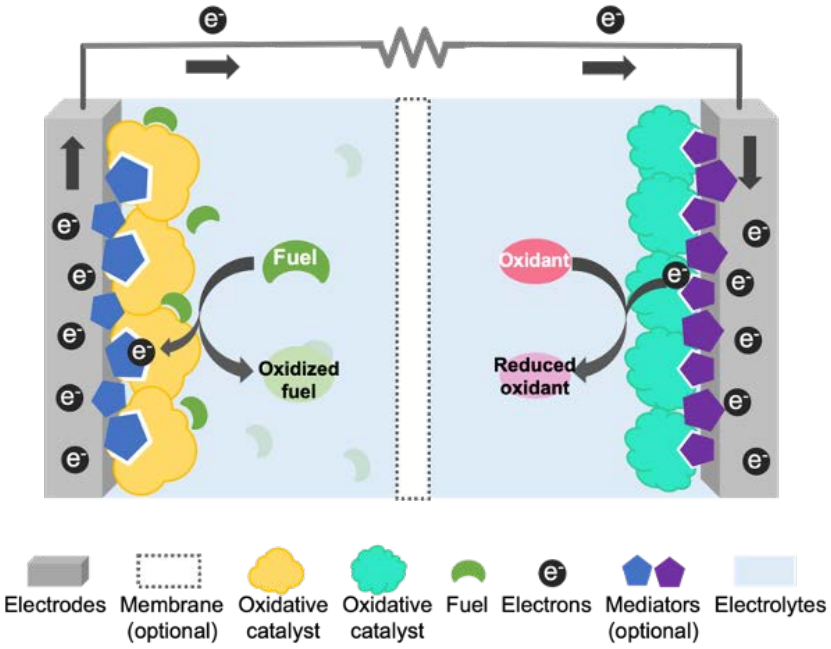

Figure 2.6 Mechanism of EBFCs.[128]

The main factors of EBFCs limiting power generation rate, low power density and low open circuit voltage are as follows: (1) the rate of electron transfer; (2) the stability of the enzyme during operation; (3) the rate of biofuel diffusion to the active site of the enzyme. [129, 130]

The transfer of electron speed is affected by enzyme activity on the one hand, and electron mediators on the other. Electron mediators are small molecules capable of accepting and donating electrons. Different ways of electron transfer formed different generations of electrochemical enzyme sensors (Figure 2.7).[131, 132] The 1st generation of BFCs employs electron-transferring reactions that generate hydrogen peroxide (H_2O_2) as a byproduct. The accumulation of H_2O_2 can adversely affect enzyme activity, leading to the development of subsequent generations of BFCs. The 3rd generation, known as direct electron transfer (DET) biofuel cells, utilizes specific enzymes with catalyst and electron transfer subunits. However, DET biofuel cells are limited by the availability of

suitable enzyme species and are costly, which hampers their widespread application. This thesis aims to focus on fabricating liquid metal-based wearable BFCs and sensors that operate on the 2nd and 2.5th generations of electron-transferring mechanisms.

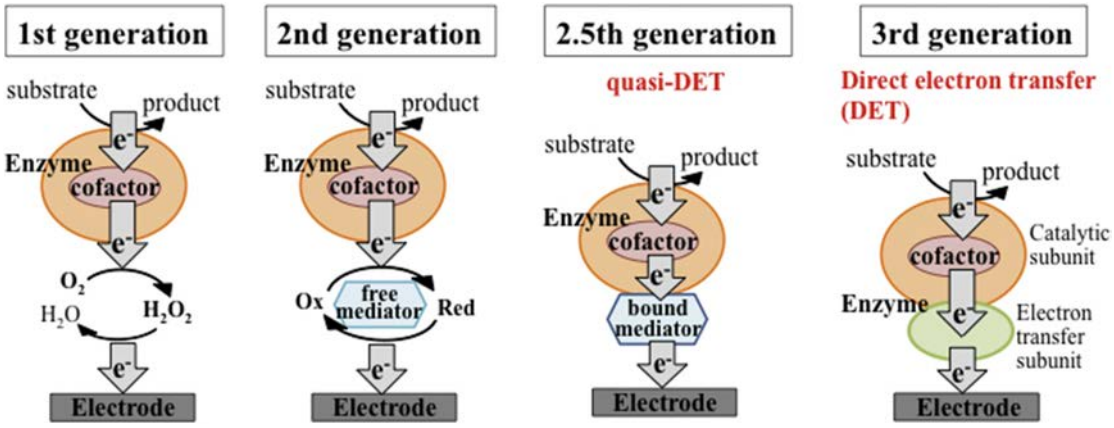

Figure 2.7 Alternative electron-transfer mechanism.[131, 132]

In addition, a synergistic effect can enhance the activity of electron transfer. For instance, Pt-black, hierarchical Ni, and other materials with high electrochemically active surface area. Researchers added Pt-black as the synergistic material of bilirubin oxidase (BOx) to promote the oxygen reduction reaction (ORR) on the cathode, while applying hierarchical Ni to anode to enhance electrochemical performance (Figure 2.9).[133]

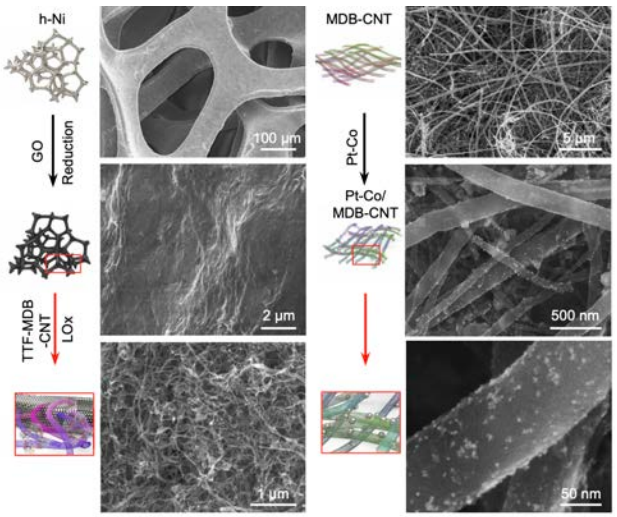

Figure 2.8 SEM images of CNTs with enzymatic co-factor and electron mediators.[133]

The stability of the enzyme can be improved by immobilizing the enzyme. Among them are physical adsorption method, covalent bonding method, cross-linking method, affinity bonding method, and entrapment method (Figure 2.9).[134] Carbon nanotubes are classified into multi-walled carbon nanotubes and single-walled carbon nanotubes. They have a large specific surface area, an ordered structure of nanotubes, and good electrical properties, so they are often used as a carrier for immobilized enzymes. Some researchers have systematically studied the condition of horseradish peroxidase (HRP) immobilized on MWCNTs, and the effect of the immobilized enzyme on the removal of phenol has been investigated. The results show that the HRP loading amount reaches 7.5mg·g^{-1} CNTs, the removal rate of phenol can be 78% within 20 minutes, and the removal rate of phenol can still reach 1/3 of the initial value after 4 cycles. Compared with free enzyme, immobilized enzyme can be stored in PBS buffer for up to 60 days, and the removal rate of phenol is basically unchanged. The diffusion rate of biofuel to the active site of the enzyme is affected on the one hand by the concentration of the substrate and on the other hand by the reaction rate at the solid-liquid phase interface.

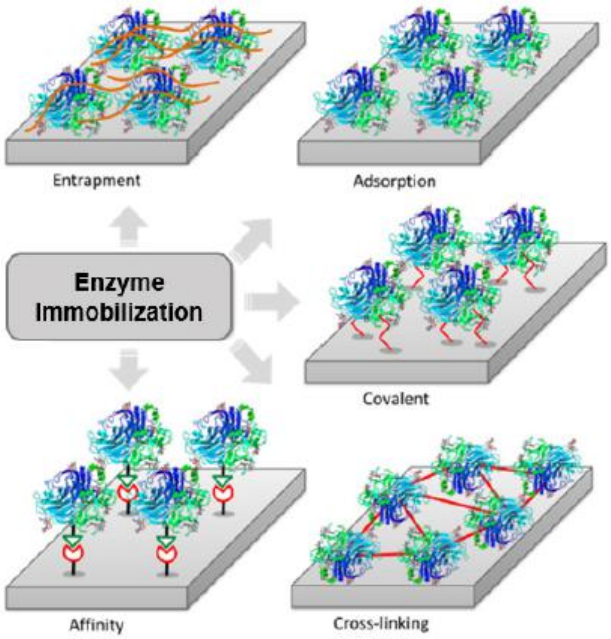

Figure 2.9 Type of immobilized enzymes[134]

Moreover, the electrolytes will affect the output energy of the biofuel cell. There are many biofluids being utilized as biofuels, such as sweat, interstitial fluid (ISF), saliva, and tears (Figure 2.10). The sweat-based BFCs are of various types attached to the skin, including tattoo, bandit, textiles, patch, and so forth (Table 2.2). Due to the ingredient of the sweat, lactate is the most used fuel in the sweat because it is in the range of 2-82 mM. [135-143] Table 2.2 summarized the power density of recent sweat BFCs, which in a range of 20 $\mu W \cdot cm^{-2}$ to 23 $mW \cdot cm^{-2}$ via burning lactate. In addition, glucose, urea, ethanol, and other materials also can be the target of the sweat BFCs.[144-146] Because ethanol has lipophilic and hydrophilic properties, it easily penetrates cell membranes. After a subject drank an alcoholic beverage, the metabolized alcohol can be quickly (5 min) detected in the sweat.[147] Researchers reported that when sweat BFCs were attached to the forearm, they could start generating electricity as early as 15.23 minutes, and the maximum power density reached 1.01 $\mu W \cdot cm^{-2}$ in 45 minutes. When attached to the forehead, the earliest power generation could be detected in 8.33 minutes, and the maximum power density can reach 0.65 $\mu W \cdot cm^{-2}$. It shows that the metabolism rate and amount of ethanol in different parts are different.[144]

Table 2.2 Published results of wearable sweat EBFCs.

Anode	Cathode	OCP (V)	J ($mA \cdot cm^{-2}$)	P ($mW \cdot cm^{-2}$)	Type
LOx	Pt	0.52	/	0.070	Tattoo-epidermal[148]
LOx	Pt	0.36	0.25	23	Bandit[149]
LOx	Ag_2O	0.45	1	0.15	Stretchable-textile[150]
LOx	Ag_2O	0.5	/	1.2	Stretchable-skin[151]
LOx	*BOx*	0.55	0.140	0.02	Patch-type[152]
LOx	*BOx*	0.74	/	0.52	Stretchable-skin[153]

The ISF-based BFCs are always connected with a microneedle to collect ISF. ISF contains water, solutes, and extracellular matrix. Interstitial water transport nutrients and metabolites between blood capillaries and cells.[154]It was reported that the glucose in ISF was highly correlative to the blood glucose and was higher than the glucose in sweat, thereby glucose was an important energy source for ISF BFCs. Researchers integrated BFC into the microneedles with glucose oxidase in the anodes and Pt blacks in the cathodes (Figure 2.10b). When the glucose in the normal range of 5-10 mM, the maximum power density reached 3-5 $\mu W \cdot cm^{-2}$. [155]

The research on saliva-based BFCs is less than other biofluid-based BFC. It is assumed that the complex environment in the mouth, such as abundant bacteria, enzymes, and so forth. Researchers collected the saliva to investigate the potential of saliva-based BFCs which consumed the glucose (Figure 2.10c). The result showed that before lunch, the maximum power density of the saliva BFC could reach 2 $\mu W \cdot cm^{-2}$, after lunch, the maximum power density could reach $3 \mu W \cdot cm^{-2}$.[156] However, the saliva sensors were shaped into a mouth guard to accommodate the acquisition of salivary electrolytes. It was reported that researchers analyzed the lactate and uric acid via an amperometric sensor. [157, 158]

The tears-based BFCs generally take the form of contact lenses (Figure 2.10d). The tears-based BFC took advantage of glucose in the tears in the anodes and oxygen in the cathodes could generate a maximum power density of 1 $\mu W \cdot cm^{-2}$ at the voltage of 0.5 V and OCP of 0.57 V.[159] 3D electrodes contribute to enhance the current density of the BFCs, due to their larger electrochemically active surface areas. Researchers used the buckypaper as electrode materials to develop a tear-based BFCs which consume lactate. Such tear-based BFC had a maximum power density of 8.01±1.4 $\mu W \cdot cm^{-2}$.[160]Furthermore, the nanoporous gold (NPG) electrodes were applied to tears-based BFCs with a OCP of 380±28 mV and the maximum power density of 1.7±0.1 $\mu W \cdot cm^{-2}$. Due to the limitation of volume of the tears, the energy harvesting by tears-based BFC is lower than sweat-based BFCs.

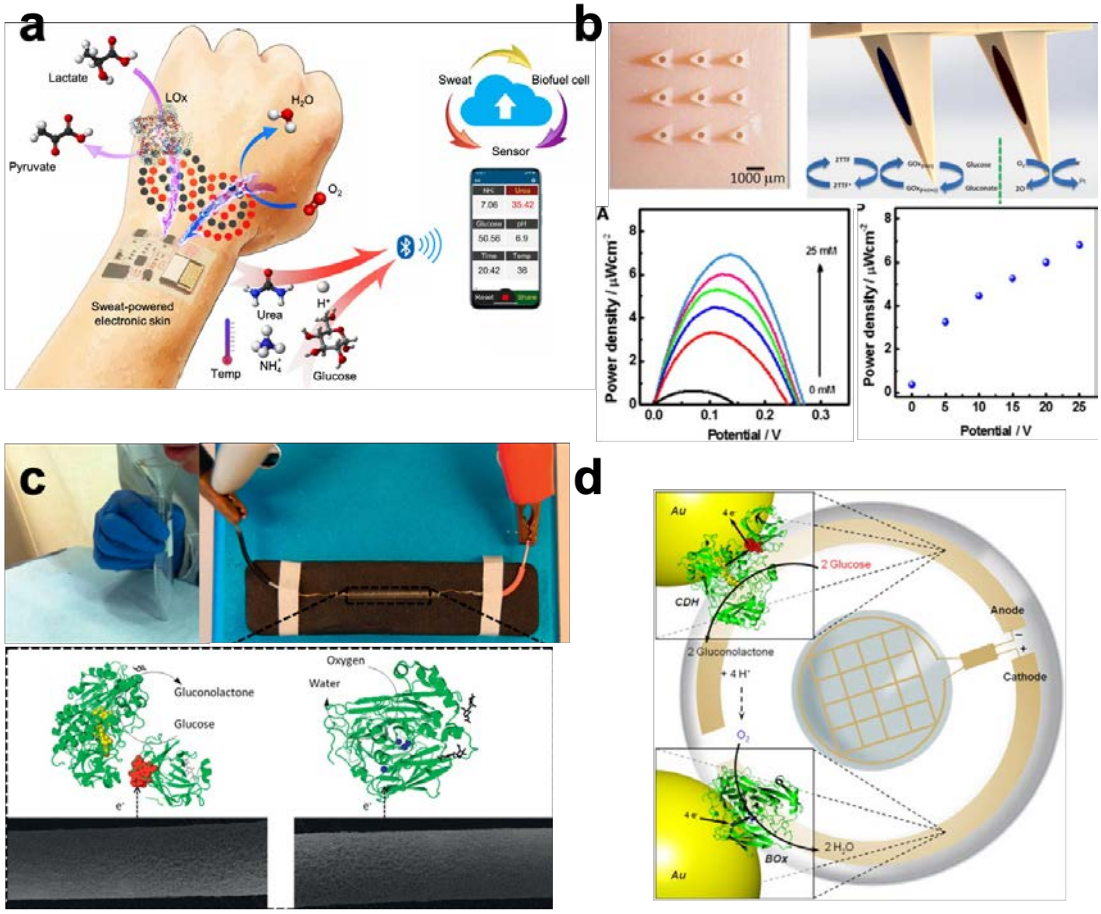

Figure 2.10 Examples of BFCs with various biofluid; (a) sweat based BFC;[133] (b) ISF based BFCs;[155](c) saliva-based BFCs;[156] (d) tears based BFCs.[159]

2.2.3 Challenges and Future of Liquid Metal-Based Biofuel Cells

This section critically examines the challenges and future prospects associated with liquid metal-based biofuel cells. It discusses potential barriers and limitations that impede the widespread deployment of these devices, such as stability, scalability, and cost-effectiveness. Additionally, it explores ongoing research efforts, developments, and possible solutions to address these challenges and enhance the performance and usability of liquid metal-based biofuel cells.

One of the major challenges facing liquid metal-based biofuel cells is ensuring their stability, particularly when exposed to acidic environments such as sweat. As sweat contains various acids, it can potentially corrode the liquid metal used in the biofuel cells. Thus, proper encapsulation of the liquid metal is crucial to protect it from direct exposure to acidic substances and maintain the stability of the biofuel cell. In terms of the future of liquid metal-based biofuel cells, there is great potential for advancements in encapsulation techniques. Researchers are actively exploring ways to develop effective and robust encapsulation materials and strategies that can provide long-term protection for the liquid metal, preventing corrosion and ensuring the overall stability of the biofuel cells.

Furthermore, as the technology progresses, efforts are being made to enhance the efficiency and power output of liquid metal-based biofuel cells. This involves optimizing the design and configuration of the cells, exploring new catalyst materials, and improving the overall performance of the electron-transferring mechanisms.

Overall, the future of liquid metal-based biofuel cells looks promising, with ongoing research focusing on addressing challenges related to stability and corrosion. By developing effective encapsulation methods and continuously improving the efficiency and power generation capabilities, liquid metal-based biofuel cells have the potential to play a significant role in wearable and portable energy systems in the future.

2.3 Liquid Metal-Based Sweat Monitoring Devices

This section presents a comprehensive review of liquid metal-based sweat monitoring devices, encompassing three subtopics: (1) a concise introduction to sweat analysis, (2) an overview of sweat monitoring devices, and (3) the challenges and prospects of liquid metal-based sweat monitoring devices. By employing a step-by-step approach, readers can comprehensively grasp the importance of sweat analysis, the methodologies utilized in current technical practices for sweat analysis, and the utilization of liquid-metal materials, a flexible, even stretchable, novel conductive material, in wearable technology. Furthermore, in the concluding subtopic, various obstacles associated with the future implementation of liquid metal applications in sweat monitoring devices are delineated.

2.3.1 Brief Introduction of Sweat Analysis

This subsection provides an overview of sweat and its importance in monitoring human health. It explores the composition of sweat, including its electrolyte levels, metabolites, and biomarkers, and explains how the analysis of sweat can provide valuable insights into various health conditions and performance levels.

Sweat is one of biofluidics that is secreted from glands to adjust body temperature and to metabolize excess materials, which means it can reveal health status in a certain extent. It is reported that human secret sweat is about 200-600 $g \cdot m^{-2} \cdot day^{-1}$.[161] One adult can secret maximum sweat up to 4 $L \cdot h^{-1}$.[162] The secretion will change according to the body temperature. Sweat glands are single tubular glands that can be divided into apocrine sweat glands and eccrine sweat glands.[163, 164] Eccrine sweat glands are mainly responsible for secreting sweat, which is distributed throughout the body and is densely distributed on the forehead, chest, palms, and soles of the feet.[165] Sweat secreted by apocrine sweat glands contains a large amount of bacteria and lipids, so it is rarely used for surface sweat detection (This thesis focuses on sweat secreted by eccrine sweat glands).

The secretion process of Na^+ and Cl^- is the driving force for the secretion of water from the blood into sweat. Water and NaCl are secreted from the cells into the lumen of the secretory part through 7 steps [166, 167]. According to the mechanism of sweat generation, it is assumed that metabolites in sweat are correlative with ISF. Table 2.3 summarizes the reported range of ingredients in blood, ISF, and sweat, respectively. These components can provide valuable insights into an individual's health status and can be used for the diagnosis and monitoring of certain diseases.[168]

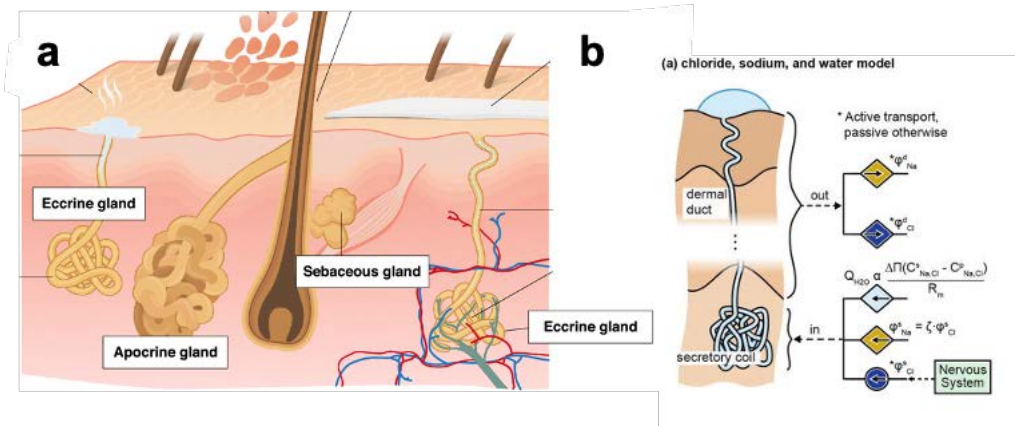

Figure 2.11 Model of sweat glands; (a) physical structure of the sweat glands[164]; (b) mechanism of secreting sweat through eccrine sweat glands[167].

Glucose is the metabolite which attracts the most attention. Glucose is a sugar and serves as an essential energy source for the body. In individuals with diabetes, the level of glucose in sweat can provide valuable information about their blood sugar control. It is reported that glucose in ISF has high correlation (>0.9) with blood glucose levels.[169] The mechanism underlying the secretion of glucose in sweat is postulated to involve paracellular transport. In this process, Claudin proteins form tight connections that facilitate the filtration of glucose from the bloodstream into sweat. Consequently, the concentration of glucose in sweat is observed to be merely 1% of the glucose concentration present in the blood[170, 171]. It is reported that before having a meal the concentration of glucose in sweat is 30-200 μM, while after having a meal the value can reach 200-500 μM.

Lactate is produced in the body during exercise or periods of high energy demand. In

biochemistry, lactate is participated in the Purine Nucleotide Cycle, PNC and the Tricarboxylic Acid Cycle, TCA cycle, which generate energy in lack of oxygen. Though the mechanism of secreting lactate in sweat is still not clear,[172] elevating levels of lactate in sweat can indicate conditions like metabolic disorders, muscle fatigue, or compromised oxygen delivery. Monitoring lactate in sweat can offer insights into an individual's exercise performance and recovery. Before doing exercise, the concentration of lactate in blood is 1.1-3.5 mM and 13-27 mM in sweat, while after doing exercise, the lactate in blood can reach 6.5-10.9 mM, and in sweat can reach 45.9-78.5mM.[135-137]

Urea is a byproduct of protein metabolism and is excreted through sweat. Elevated levels of urea in sweat can be linked to kidney dysfunction or abnormalities. Sweat urea analysis can aid in monitoring kidney health and detecting early signs of renal impairment.

Na^+ are electrolytes that help regulate fluid balance and maintain blood pressure. Abnormal levels of sodium in sweat can be indicative of conditions like dehydration, electrolyte imbalances, or certain kidney disorders. [135, 140, 173-175]

K^+ is another essential electrolyte involved in maintaining proper cellular function and muscle contractions. Sweating can lead to potassium loss, which can be relevant in conditions like electrolyte disturbances or excessive sweating disorders. [135, 174]

Alcohol can be detected in sweat after consumption, and its detection in sweat can be used as an indirect measure of alcohol consumption or monitoring compliance in alcohol abuse treatment programs. [147, 176, 177] A non-invasive electrochemical device has been documented as having the capability to detect alcohol in sweat approximately 5 minutes after the consumption of an alcoholic beverage.[147] This device utilizes electrochemical sensors to measure the concentration of alcohol present in sweat, providing a rapid and convenient method of alcohol detection. The findings indicate a strong correlation between the alcohol concentration observed in sweat and the

corresponding levels in the bloodstream, with a correlation coefficient as high as 0.934. Furthermore, extensive research substantiates a strong correlation between the concentration of alcohol in sweat and that in the blood. [176] This correlation is attributed to the presence of lipophilic and hydrophilic groups facilitating the permeation of alcohol molecules through the cell wall. As a result, monitoring alcohol levels in sweat holds immense value in assessing and quantifying alcohol consumption.

Sweat analysis for diagnostic purposes is an emerging field with the potential to revolutionize healthcare. Non-invasive and continuous monitoring of these sweat components can enhance disease management, facilitate early detection, and provide personalized healthcare interventions. It is important to note that while sweat analysis shows promise in various medical applications, additional research and validation are necessary to establish its clinical practicality and reliability.

Table 2.3 Molecular signatures[167, 178]

Targets		Reported range			Health relative meanings	Refs.
		Blood	ISF	Sweat		
Metabolites	Glucose	2.7-11.1mM;	2.8-23.6 mM;	30–500 μM*	Diabetes	135, 137, 169, 179-187
	Lactate	1.1- 10.9mM	2-18 mM	2–82 mM*	Lactic acidosis, sport training	135-143
	Urea			2–6 mM		188
	Creatinine	65-140 μM	/	9-18 μM	Kidney diseases	189-191
Electrolytes	Na^+	135 – 145 mM	/	10-266mM*	Hydration, heart failure, liver disease	135, 140, 173-175
	Cl^-	96 – 106 mM	/	10-100 mM	Cystic fibrosis	140, 173-175, 192, 193
	K^+	5-6 mM		2–39 mM*		135, 174
	Ca^{2+}			80-453 μM*	Uremia, chronic renal disease	174
	Mg^{2+}			76-569 μM*	Uremia	174, 194
	Ammonium (NH4+)		20–50× < sweat concentration	0.5–8 mM		

Targets		Reported range			Health relative meanings	Refs.
		Blood	ISF	Sweat		
Hormones	Cortisol	0.07 – 690 nM	Similar to blood plasma	0.1 – 20 nM	Stress, anxiety, cushing syndrome	[195-197]
	Testosterone	Female: 0.52 – 2.4 nM; Male: 9.7 – 38.3 nM		Lack of report	Heart muscle damage, fertility issues, irregular menstrual periods	
Nutrients	Tyrosine	200 – 400 μM	Similar to blood plasma	66 – 300 μM	Metabolic disorders, gout	[198]
	Tryptophan	55–80 μM		20 – 91μM	Anxiety, nerve damage	
	Vitamin C	2.8 – 98μM		0-36 μM	Connective tissue defects, joint pain	[199]
Proteins	Cytokines	Picomolar to nanomolar	15-42% of blood plasma	1.97 × 10–5 (IL-1α)	Immunodeficiency disorders, cytokine storm	[170]
	C-reactive protein	7 – 29 nM	Lack of report	4.2 – 250 pM	Coronary heart disease, obstructive pulmonary disease	
Drugs	Levodopa	0.5–15	Similar to blood plasma	Similar to plasma	Parkinson's disease	
	Acetaminophen	66 - 132 μM		0 – 50 μM	Fever, pain	[200]
	Alcohol	2.5-22.5 mM		2.5-22.5 mM		[177]

Notes:1mM = 18 $mg \cdot dl^{-1}$;

The asterisk (*) signifies that this research study adds value to the existing body of knowledge in the academic field.

2.3.2 Overview of Sweat Monitoring Devices

Sweat monitoring devices have seen significant advancements in recent years, enabling real-time and non-invasive measurement of sweat components. This subsection delves into the different types of sweat-monitoring devices, including electrochemical sensors, colorimetric sensors, and fluorescence devices (Figure 2.8). It examines their working principles, sensitivity, and limitations, and discusses the recent advancements and developments in the field of sweat monitoring technology.

2.3.2.1 Electrochemical sensors

Amperometric sensors measure the current produced by an electrochemical reaction to quantify analyte concentration. They typically employ working electrodes and reference electrodes to perform measurements. Amperometric sweat sensors demonstrate high sensitivity, low detection limits, and real-time monitoring capabilities. They are commonly used for monitoring glucose, lactate, alcohol, and various ions in sweat.

Potentiometric sensors rely on the difference in potential between electrodes to determine analyte concentration. These sensors utilize ion-selective membranes that respond to specific ions. They offer simplicity, stability, and can detect sodium, potassium, and calcium ions in sweat.

Voltammetric sensors apply a voltage to generate an electrochemical response. By measuring the resulting current, analyte concentration can be determined. Voltammetric sensors offer high sensitivity, selectivity, and are suitable for detecting various compounds in sweat, including glucose, lactate, and alcohol.

2.3.2.2 Colorimetric sensors

Colorimetric sensors rely on color changes to indicate specific analyte concentrations.[201] These sensors use indicators that react with analytes, leading to observable color changes.[202] The intensity or shift in color is correlated to the analyte concentration. The advantages of colorimetric sweat sensors are simple, cost-effective, and offer real-time visual readout. They find applications in detecting analytes such as pH, glucose, and lactate in sweat, also in detecting the sweating rate[202].

2.3.2.3 Fluorescence sensors

Fluorescence sweat sensors use fluorescent probes that emit light at specific wavelengths in response to analyte binding or chemical reactions. The emitted light is then measured to determine analyte concentration. These sensors offer high sensitivity,

selectivity, and allow for multiplexed detection. Fluorescence-based sweat sensors have been developed to monitor glucose, lactate, ions, and other biomarkers.

Sweat monitoring devices, including electrochemical sensors, colorimetric sensors, and fluorescence devices, have made significant progress in recent years. These devices offer promising opportunities for real-time, non-invasive, and continuous monitoring of sweat components, facilitating personalized healthcare and disease management. However, further advancements, validation, and integration with data analysis platforms are still required to fully realize the potential of sweat monitoring technology in clinical practice.

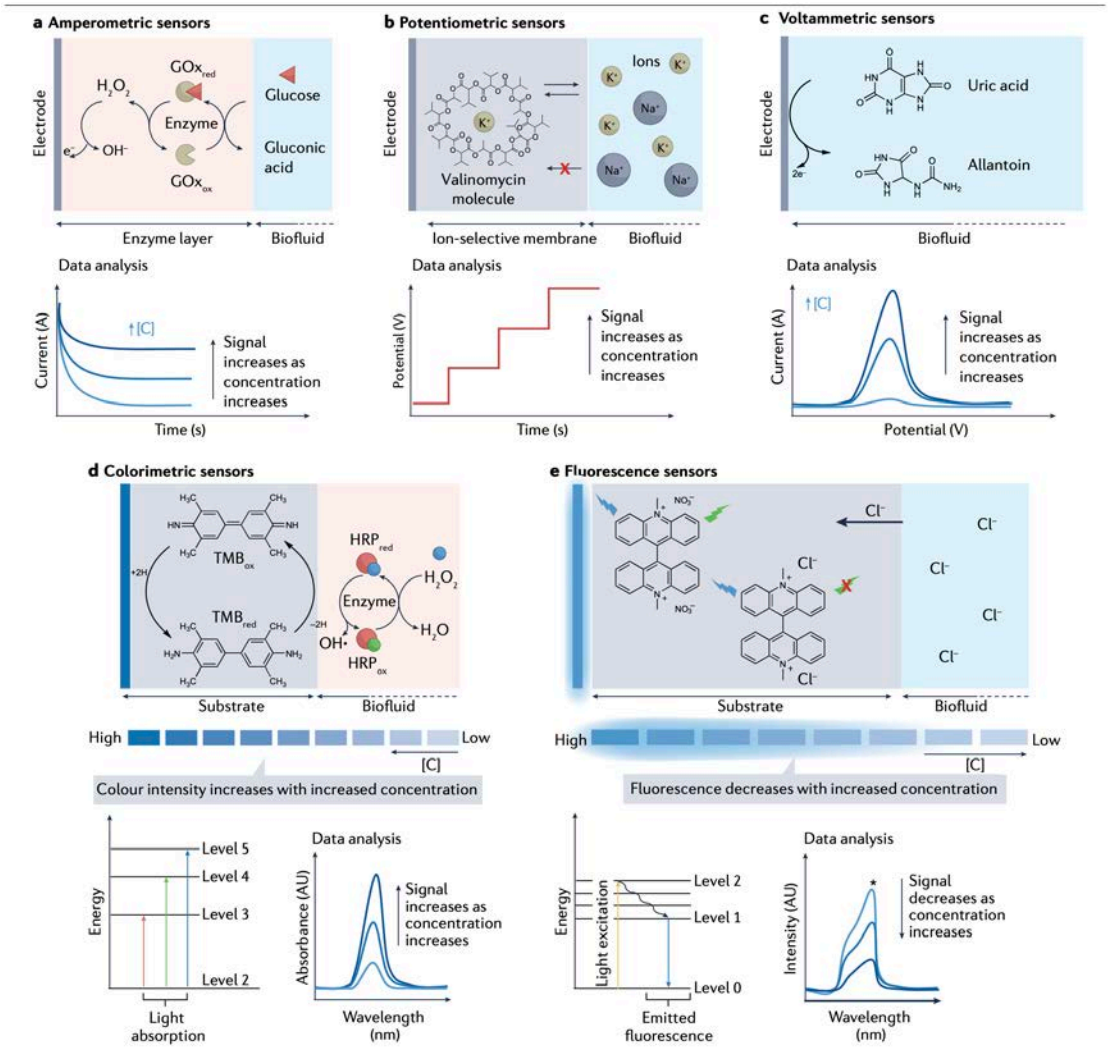

Figure 2.12 Different types of sweat monitoring devices and their working principles.[178]

2.3.3 Challenges and Future of Liquid Metal-Based Sweat Monitoring Devices

This subsection analyzes the challenges and outlooks of using liquid metal-based sensors for sweat monitoring. Previously, we discussed the advantages of liquid metal, such as its excellent conductivity, flexibility, and biocompatibility, in designing and fabricating high-performance sweat sensors. However, the implementation of these sensors for sweat monitoring comes with certain challenges, including stability and general problems associated with sweat sensors. Here, we will analyze these challenges and discuss the outlooks for liquid metal-based sensors in sweat monitoring.

Liquid metals, like gallium-based alloys, are highly reactive with the surrounding environment, making their encapsulation crucial for long-term stability. Strategies such as encapsulating liquid metal within elastomers or biocompatible materials have been proposed to address this challenge. Ongoing research focuses on developing encapsulation techniques that provide a barrier against oxidation and mechanical stress, ensuring the stability of liquid metal-based sensors.

Integrating flexible sensors with conventional rigid circuits can pose challenges regarding mechanical compatibility and electrical interconnectivity. Developing reliable methods for seamless connection, such as using conductive adhesives, stretchable conductors, or soft interconnects, is critical to ensuring stable and robust data transmission.

The low sweat rate inherent in some individuals can pose a challenge for sweat sensors. Detecting and collecting sufficient sweat volumes for analysis becomes vital. Advances in microfluidic systems and sweat stimulation techniques aim to improve sweat secretion rates and enable reliable measurements, even in individuals with low sweat rates.

Sweat samples can rapidly evaporate, leading to concentration changes that can affect sensor accuracy. Microfluidic-based systems with controlled flow rates, optimized

sample collection techniques, or on-site analysis within a closed system can help minimize sample evaporation and maintain measurement reliability.

Sweat sensors should collect pure sweat uncontaminated by skin debris, lotions, or other substances present on the skin surface. Strategies like sweat stimulation using iontophoresis or using selective ion-channel-based sensors can help minimize contamination and improve the specificity of sweat analysis.

Sweat sensors rely on obtaining fresh, immediate sweat samples for accurate analysis. Currently, techniques like sweat patches or microneedle-based devices are being explored to facilitate collecting real-time sweat samples. Developments in wearable and disposable sweat collection methods aim to overcome challenges related to sweat evaporation and sample contamination.

Despite the challenges, liquid metal-based sensors for sweat monitoring hold immense potential. Ongoing research and technological advancements aim to overcome stability concerns by developing reliable encapsulation techniques and seamless integration with electrical circuits. Additionally, addressing general problems of sweat sensors, including low sweat rates, sample evaporation, and contamination, will lead to improved accuracy and reliability.

Overall, addressing the challenges associated with liquid metal-based sensors for sweat monitoring will pave the way for improved accuracy, reliability, and widespread adoption of this promising technology in various applications, including healthcare, sports performance, and personalized wellbeing.

Chapter 3 Methodology

3.1 Materials

Chemicals being used are listed as follow:

Hydroxyl multiwall carbon nanotubes (MWCNT-OH) and MWCNT-COOH were from XFnano, China. MWCNT (NC7000) were from nanocyl, Belgium. Thermoplastic polyether urethanes (TPU) were from Evermore Chemical Industry CO., LTD., Taiwan (R.O.C.). The eutectic Gallium and Indium (EGaIn, 4:1, 100 g) were from Haoke Technology Inc., Beijing, China. Aniline, tetrahydrofuran, dimethylformamide, 1-decanol, carboxymethyl cellulose (CMC, M.W. 250000) and hydroxypropyl chitosan (> 80%) were from Macklin Inc., China. Sodium periodate ($NaIO_4$), sodium chloride (NaCl), potassium chloride (KCl), polyvinyl alcohol (PVA, the 1799 type), polyvinyl butyral (PVB), albumin bovine (BSA), Na ionophere X, sodium tetraki[3,5-bis(trifluoromethyl)phenyl]borate (Na-TFPB), bis(2-ethylehexyl)sebacate (DOS), PVC, valinomycin, sodium tetraphenylborate (Na-TPB), cyclohexanone and ethylene glycol were from Shanghai Aladdin Biochemical Technology Co., Ltd. Carbon Mediator Paste C2070424P2 was from SunChemical, U. K. SYLGARD™ 184 Silicone Elastomer, from Dow Corning, America. 1x PBS was from Solarbio, China. Glucose oxidase (G2133), glucose, and 25 % Nafion solutions, 5 % glutaraldehyde solution were from Sigma-Aldrich, America. Lactate oxidase (LOx, LCO-301) was from Toyobo, Japan. Bilirubin oxidase (BOx) was from Yuanye, China. Hydrochloric acid and sulfuric acid were from Dongguan Dongjiang Chemical Reagent Co., Ltd., China. Styrene-ethylene-butylene-styrene (SEBS, G1645) was from Kraton, America.

3.2 Chemicals Synthesis and Solution Preparation

0.5M KCl solution: 18.625 g of KCl was added to 1x PBS solution.

Electrolytes for electropolymerization of PANI: 16.42 mL HCl and 1.828 mL aniline were added to 181.752 mL deionized water.

TPU solution: 90 g of TPU was added to a mixture of 286.77 mL THF and 270.12 mL DMF.

Metal-polymer composite ink: 3 g of EGaIn was added to 1 mL of 5 % PVB solution and sonicated for 90 s with an amplitude of 25 %.

Enzyme solution: 40 $mg \cdot mL^{-1}$ GOD, 40 $mg \cdot mL^{-1}$ LOx, and 10 $mg \cdot mL^{-1}$ BOx solution, respectively, were dissolved into 10 $mg \cdot mL^{-1}$ BSA solutions (with a solvent of 1 x PBS).

Hydroxypropyl chitosan solutions: 300 mg hydroxypropyl chitosan in 5 mL deionized water.

Dialdehyde CMC (DCMC) solution: 300 mg DCMC in 5 mL deionized water.

Glucose solution: 4.5 g of glucose in 50 mL 0.5M KCl solution.

Lactate solution: 2.25 g of lactate in 50 mL 0.5M KCl solution.

3.3 Experimental Procedures

3.3.1 Screen-printing Method

The fabrication process of the EGaIn ink involved the sonication of liquid metal and PVB solution. The sonicator was set at 25 % amplitude with 5 s pulses and 5 s rest for a total time of 90 s.

3.3.2 Fabrication of Dialdehyde CMC

A solution was prepared by adding 2 g of CMC and 0.8 mL of 3 M H_2SO_4 into 40 mL of deionized water. After dispersing the CMC, a solution containing 20 mL of NaIO4

with a concentration of 50 mg·mL^{-1} was added to the dispersing agent. The mixture was subjected to stirring in a water bath at 40 ℃ for 4 hours. Subsequently, 1.3 mL of ethylene glycol was added to the resulting dialdehyde CMC (DCMC) solution, which was then stirred for an additional 0.5 hours. The solution was dialyzed in deionized water for 2 days. Finally, the solid DCMC was obtained by drying the solution at 4 ℃.

3.4 Characterization

3.4.1 Morphology

The morphology of the biofuel cell was characterized using a scanning electron microscope (HITACHI SU8100/HITACHI MC1000) with an accelerating voltage of 5 kV.

3.4.2 Tensile Strain

The testing sample was cut into a rectangular shape with a length of 30 mm and with a width of 10 mm. The sample was loaded on an Instron tester with a length of 20 mm, testing with a speed of 50 mm·min^{-1}.

3.4.3 Electrical Performance

The digit precision multimeter (Fluke, 8845A) and source meter (Keithley, 2400) were used to record the resistant and current of electrodes.

3.4.4 Electrochemical Performance

The electrochemical performance of electrodes was evaluated by electrochemical workstation (Metrohm, Autolab), portable electrochemical workstation (HY-E100X, ichy) and electrochemical module (PalmSens, EmStat Pico Module).

According to the Nernst equation (formula 1), the mechanism of Na^+ or K^+ sensor can be obtained (formula 2).[203] The potential of the sensor hence changes logarithmically

with the Na^+ concentration.

$$E_{\text{cell}} = E^{\ominus}_{\text{cell}} - \frac{RT}{ZF} ln \frac{[Red]}{[Ox]} \qquad (3.1)$$

where E_{cell} is the cell potential (electromotive force) at the temperature of interest, $E^{\ominus}_{\text{cell}}$ is the standard cell potential, R is the universal gas constant: $R = 8.314463\ \text{J}\cdot\text{K}^{-1}\cdot\text{mol}^{-1}$, T is the temperature in kelvins, Z is the number of electrons transferred in the cell reaction or half-reaction, F is the Faraday constant, $F = 96485.3321233100184\ \text{C}\cdot\text{mol}^{-1}$.

$$\Delta E = E^{\ominus}_{\text{cell}} - E_{cell} = \frac{RT}{ZF} ln \frac{[Red]}{[Ox]} \qquad (3.2)$$

To test the electrical performance, the biofuel cell needs to be verified the half-cell and cell reaction by electrochemical workstation in two-electrode and three-electrode systems respectively.

Electrochemical impedance spectroscopy (EIS) is a technique that measures the dielectric properties of a medium as a function of frequency.[204] EIS facilitates the measurement of the equivalent circuit composition of the complete electrochemical system and the internal resistance of said system. Moreover, EIS enables the determination of diffusion resistance and electron transfer resistance during the electrochemical reaction, thus facilitating analysis of the material reaction process.

Cyclic voltammetry (CV) is a general electrochemical research method to assess a new electrochemical system.[205] This method involves the control of the electrode potential, wherein a triangular waveform is scanned multiple times at varying rates over a defined time period. The potential range chosen allows for alternating occurrence of reduction and oxidation reactions on the electrode. Subsequently, the current-potential curve of the electrode is recorded. The shape of this curve aids in determining the reversibility of the electrode reaction, the presence of intermediates, phase boundary adsorption, new phase formation, and the characteristics of coupled chemical reactions. It is commonly utilized to measure electrode reaction parameters, establish its controlling

steps and reaction mechanism, as well as observe the range and properties of reactions that can transpire within the entire potential scanning range.

Chronopotentiometry (CP) is an electrochemical analysis method and an electrochemical technique for studying electrode processes. It measures the relationship between electrode potential and time in the electrolysis process under a certain fixed current. Similarly, chronoamperometry (CA) measures the relationship between the current response and time in the electrolysis process under a certain potential. CA is applied to glucose and lactate sensing.

The electrochemical performance of the half cells and biofuel cells was evaluated using an electrochemical workstation. The electrochemical characterization was conducted in a 0.5 M KCl solution in 1×PBS. The enzyme-catalyzed oxidation and oxygen reduction reactions were assessed using the LSV technique, with the sweeping rate of 5 $mV \cdot s^{-1}$. The experimental setup consisted of a three-electrode system, with the working electrode, a Pt film as the counter electrode, and an Ag/AgCl (3 M KCl) reference electrode.

In the case of the biofuel cell device, a two-electrode system was employed, with the bioanode serving as both the counter and reference electrode, and the biocathode as the working electrode. The LSV curves of the biofuel cell, under different glucose and lactate concentrations, were obtained by scanning from the open circuit potential (OCP) to 0.01 V at a rate of 5 $mV \cdot s^{-1}$.

Chapter 4 Liquid Metal-based Stretchable Sweat Biofuel Cells

This chapter explores the incorporation of liquid metal-polymer conductors (MPC) in the development of sweat biofuel cells, specifically focusing on the fabrication of a liquid metal-based sweat biofuel cell. This application of MPC presents novel possibilities in the realm of flexible wearables. The production process primarily relied on the screen-printing method, enabling cost-effective manufacturing. The electrode morphology was analyzed using SEM, while the tensile strain experienced during the fabrication process was evaluated using a universal stretching machine. The electrochemical performance, open circuit potential, and power density of the biofuel cell were assessed by employing an electrochemical workstation. Moreover, the integration of an external booster module facilitated the provision of power to a commercial health monitoring module, effectively demonstrating the application of this biofuel cell in the wearable technology domain.

4.1 Introduction

Biological fuel cells possess significant potential as a sustainable and long-lasting power source for wearable devices, as they harness the energy derived from natural metabolites to generate electrical energy.[152, 153, 206] The fundamental principle behind biofuel cells is their ability to continuously produce energy if the organism continues to produce metabolites that can serve as fuel. Incorporating biofuel cells into wearable devices has the advantage of significantly extending their lifespan. Furthermore, the growing demand for clean and renewable energy sources has propelled interest in biofuel cells, as the fuels and active materials used in these cells are biodegradable and environmentally friendly.[207] This characteristic minimizes the risk of environmental contamination while also enabling artificial regeneration of the cell components.[208] Notably, biofuel cells offer unique advantages beyond their applicability in power generation for wearable devices. They can be employed in biosensors, toxic detection systems, and drug delivery systems, further broadening their potential applications.[209]

In order to optimize the efficiency of power conversion, it is crucial for wearable biofuel cells to have a high degree of conformance with biological interfaces[210, 211]. Previous research has explored the use of nanoscale wavy gold and copper as conductors in wearable analytical devices to better adapt to the deformations of biosurfaces[151 212, 213]. However, these fabrication processes are complex and costly (Table 4.1). Printable silver inks have been proposed as a stretchable conductor for biofuel cells to withstand deformation [153]. Nonetheless, silver itself can provoke localized allergic reactions and is toxic [214]. Carbon-based conductors, while affordable and easy to prepare, possess limitations in stretchability and conductivity that restrict their applications.

Table 4.1 Comparison of previously reported conductors with the present work.

	Fabrication	Price of raw material[a] (USD·g^{-1})	Substrate	Electrical conductivity	Stretchability	Ref.
MPC	Screen-printing	0.52	PDMS	10^5	> 200%	/
Au	Sputtering	57.93	Electrospun mat	10^7	/	[215]
Au	Photolithography	57.93	Silicone	10^7	50 %	[151]
Ag	Screen-printing	0.66	Ecoflex	10^7	20 %	[153]
Cu	Electrodeposition	0.0077	Buckypaper	10^7	/	[216]
Cu	/	0.0077	Cu film	10^7	/	[217]
Carbon	Screen-printing	/	tattoo	10^2	/	[210]
Carbon	carbon cloth	/	Bandit	10^2	/	[149]

a. Data from London Metal Exchange, expiration date 21/10/2022

To address these challenges and enhance the stretchability and conformance of biofuel cells, our study incorporates highly stretchable and compatible MPC as interconnections for the biofuel cells.[12, 60] The MPC allows for conformal contact with the skin, establishing a stable and reliable bio-interface between the device and the skin.[63] Here, we present a novel approach for fabricating skin-attachable biofuel cells using MPCs, enabling a substantial fit with the deformations of the epidermis.

4.2 Experimental Section

4.2.1 Fabrication of MPC

The process of manufacturing MPC involved four sequential steps, as illustrated in Figure 4.1. To begin, the EGaIn ink was created by subjecting a mixture of liquid metal and PVB solution to ultrasonic treatment. Next, the EGaIn ink was applied onto a PET film through the screen-printing technique, followed by drying in an oven set at 80 ℃ for 5 minutes. Subsequently, a layer of PDMS was spin-coated onto the patterned EGaIn, ensuring complete infiltration of the PDMS into the gaps present between the EGaIn particles. Upon completion of PDMS curing, the PDMS layer was peeled off, yielding the MPC with the patterned EGaIn successfully transferred onto the polydimethylsiloxane (PDMS) layer.

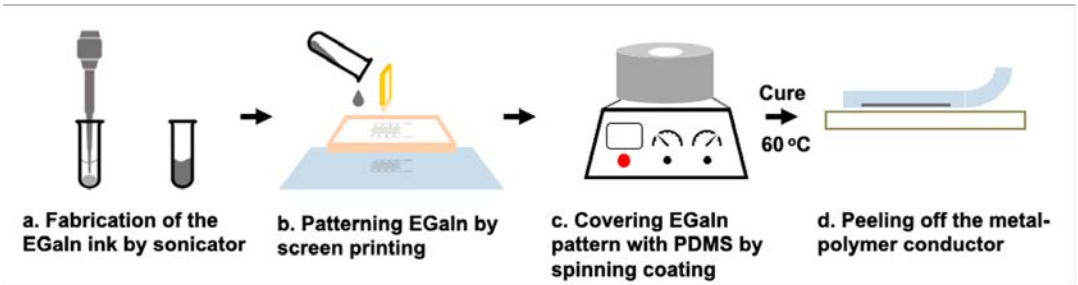

Figure 4.1 Scheme of fabricating MPC

4.2.2 Characterization of MPC

The MPC underwent an assessment encompassing the evaluation of its morphology,

electrical performance, and mechanical performance. The morphology of the MPC was examined through SEM. In Figure 4.2, the SEM images illustrated the successful embedding of the liquid metal particles within the PDMS matrix, resulting in enhanced stability and reduced leakage of the liquid metal. To further understand the structure of MPC, the cross-sectional view of acid-treating MPC is shown in Figure 4.2b. After acid treatment, the liquid metal particles in the MPC were consumed, leaving porous PDMS. This indicated that the MPC prepared in such method made liquid metal particles being encapsulated by PDMS, thereby reducing the likelihood of damage to the liquid metal circuit. Additionally, the thickness of the MPC was determined by analyzing the cross-sectional SEM images, yielding an average thickness value of 9.782 μm. Furthermore, the electrical resistance of the MPC was measured across a 1 cm length sample. In compliance with Ohm's Law, the electrical conductivity of the MPC was calculated to be 2.7×10^{5} $S\cdot m^{-1}$, representing an order of magnitude increase in comparison to conductors based on hydrogels or carbon.

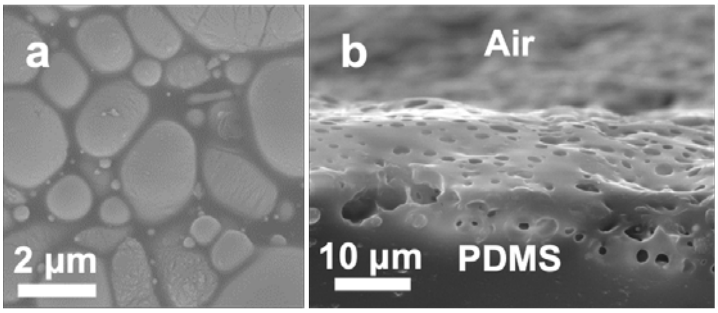

Figure 4.2 SEM images of the MPC; (a) top view of MPC; (b) cross-sectional view of acid-treating MPC. The mean value of the thickness of MPC was 9.782 μm.

The mechanical properties of the MPCs were assessed using a universal testing machine. The Young's modulus of the MPC was determined to be 0.844 ± 0.089 kPa, while the tensile strain exhibited a value of approximately 250%. The elastic deformation region was observed to span from 0% to 50% of the strain range. Considering the Poisson effect of the elastomer, it was observed that the thickness of the MPCs decreased when subjected to stretching. Thus, resistance was utilized as a measure to characterize the

electrical performance of the MPCs under strain.

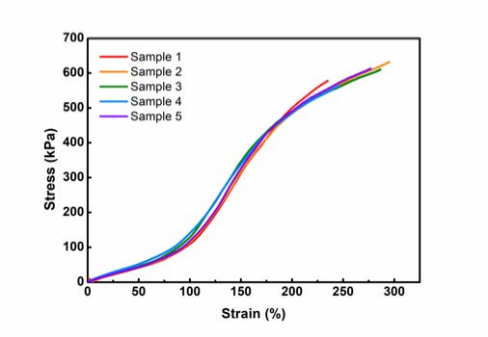

Figure 4.3 Tensile strain of MPC (sample numbers n = 5)

4.2.3 Fabrication Stretchable Liquid Metal-based Biofuel Cells

The stretchable liquid metal-based biofuel cells were composed of several components: a PDMS substrate, an MPC embedded within another PDMS layer, carbon electrodes with sensing materials, and PDMS pellets positioned on the backside of each electrode (Figure 4.4). In this section, we will discuss the fabrication process of the stretchable liquid metal-based biofuel cells following the preparation of the MPCs.

To prevent excessive strain on the electrodes, PDMS pellets were created by mixing a base and curing agent in a ratio of 6:1, resulting in a PDMS material with a higher Young's modulus. These cured PDMS pellets were then attached to the backside of the electrodes using a diluted PDMS precursor. After drying, the entire MPC electrode was peeled off and reversed to enable the printing of carbon paste.

In addition to the carbon electrode, another thin layer of PDMS (with a ratio of 10:1) was spin-coated onto the substrate. The spin-coating process involved rotating the substrate at speeds of 200 rpm for 30 seconds, 400 rpm for 15 seconds, and 1500 rpm for 15 seconds. Once the PDMS was fully cured, the carbon electrode was immersed in a solution containing 0.1 M aniline and 1 M HCl to electro-polymerize a layer of polyaniline (PANI) onto the electrode surface. The electro-polymerization process was

conducted using cyclic voltammetry, with a potential range of 0.2 V to 1.0 V applied for 25 cycles using a chemical workstation.

To functionalize the electrodes, solutions of glucose oxidase (GOD) at a concentration of 40 $mg \cdot mL^{-1}$, lactate oxidase (LOx) at a concentration of 40 $mg \cdot mL^{-1}$, and bilirubin oxidase (BOx) at a concentration of 10 $mg \cdot mL^{-1}$ were prepared. The GOD or LOx solutions were dissolved in 20 $mg \cdot mL^{-1}$ solutions of bovine serum albumin (BSA) using 1 x phosphate-buffered saline (PBS) as the solvent. We deposited 2 µL of the enzymatic solution onto each electrode and allowed them to dry at 4 ℃.

For the cathodes, we applied a solution of 40 mM protoporphyrin IX (PPIX) in a 9:1 v/v ethanol/acetone mixture onto the electrodes and allowed them to dry under ambient conditions. To prolong the lifespan of the biofuel cell (BFC), chitosan hydrogel was used to immobilize the enzymes. We prepared 6% solutions of hydroxypropyl chitosan (300 mg in 5 mL 1 x PBS) and 6% solutions of carboxymethyl cellulose (300 mg in 5 mL 1 x PBS). The carboxymethyl cellulose and hydroxypropyl chitosan solutions were mixed, with 4 parts of carboxymethyl cellulose solution and 1 part of hydroxypropyl chitosan solution. Before forming the hydrogel, a 5 µL mixture was dropped onto each bio-anode electrode, and the BFC was then stored at 4 ℃.

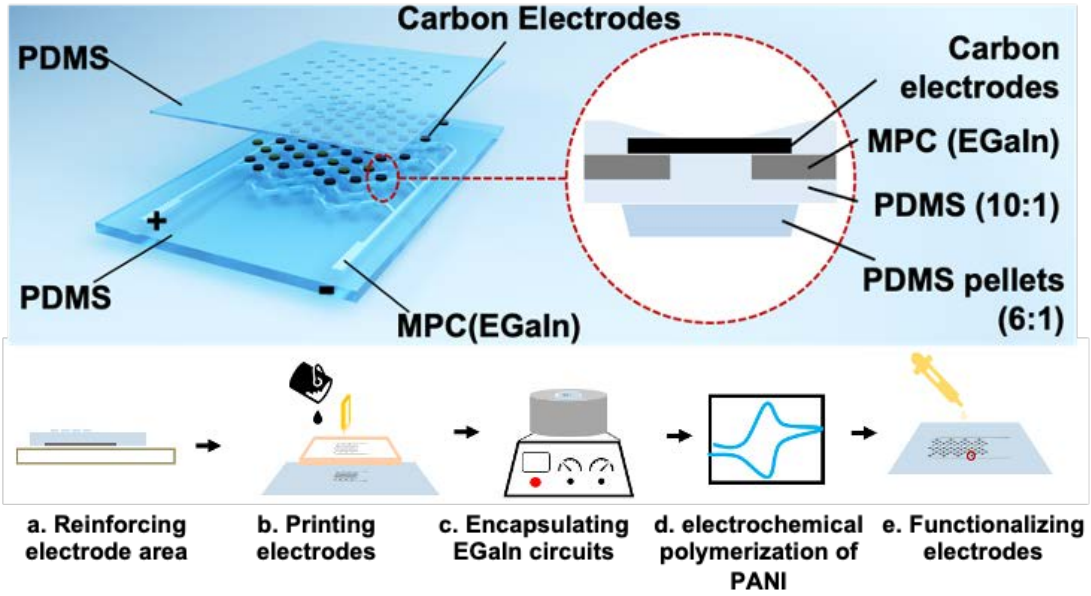

Figure 4.4 Scheme of fabricating stretchable liquid metal-based biofuel cells

4.3 Results and Discussions

4.3.1 Morphology of Stretchable Liquid Metal-Based Biofuel Cells

The morphology of the BFC was characterized using optical microscopy and SEM, with a particular focus on any changes in detail before and after stretching. The electrode structure was designed as shown in Figure 4.4 for specific reasons: firstly, the presence of PDMS pellets on the backside of the electrodes helped to limit the deformation of the electrode during stretching. Secondly, the printed carbon electrode was unable to completely seal the MPC layer, potentially allowing electrolyte to penetrate the gallium-based MPC and causing unexpected electrochemical signals. Thus, the electrode portion of the MPC circuit was designed in a toroidal shape, with the circular carbon electrode printed on the toroidal structure to maintain electrical conductivity. Lastly, the PDMS encapsulated layer covered the entire area containing the MPC, including the overlap area between the carbon electrodes and the MPC, apart from the interface for the adapter. Figure 4.5 displayed photos of the BFC from various

perspectives (top, cross-section, and oblique view) to provide a clearer understanding of the structure for readers.

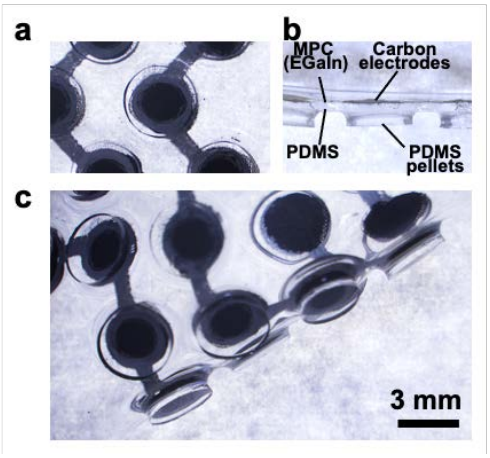

Figure 4.5 Photos of electrodes of biofuel cells. (a) top view, (b) cross-section view, and (c) oblique view of the electrode.

SEM was employed to observe the morphological characteristics of each material layer and analyze any changes that occurred after stretching. The MPC surface exhibited the presence of numerous liquid metal particles embedded within it. Despite slight differences in shape before and after stretching, a connected network of particles was formed within the MPC, enabling electrical conductivity. The carbon electrode possessed a sheet-like structure with small perforations, and the deposition of PANI resulted in the emergence of burr-like structures on the electrode surface, increasing its specific surface area. Moreover, a thin film layer formed on the functionalized electrode surface. Notably, after stretching, the carbon, PANI, and enzyme layers remained intact, indicating that the design strategy was partially successful in preventing damage to these layers due to stress.

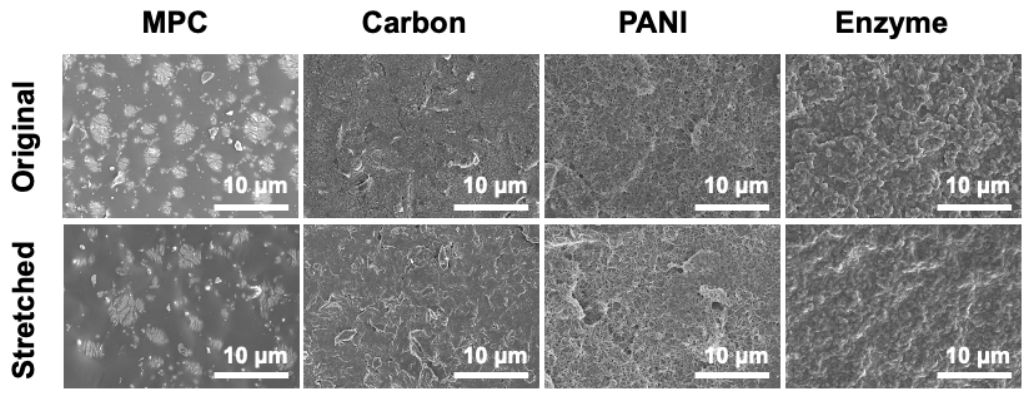

Figure 4.6 SEM images of different layers of the electrode before and after being stretched.

4.3.2 Mechanical Performance of Stretchable Liquid Metal-Based Biofuel Cells

Based on the aforementioned electrode structure (Figure 4.4), the electrodes were found to withstand a strain of up to 40% without sustaining damage, as illustrated in Figure 4.6. As exemplified in Figure 4.7, the stretchable and bendable nature of the liquid metal-based biofuel cell indicated its ability to conform to and wrap around limbs and the human body. Additionally, this design ensured that the PDMS pellet was positioned on the side opposite to the body.

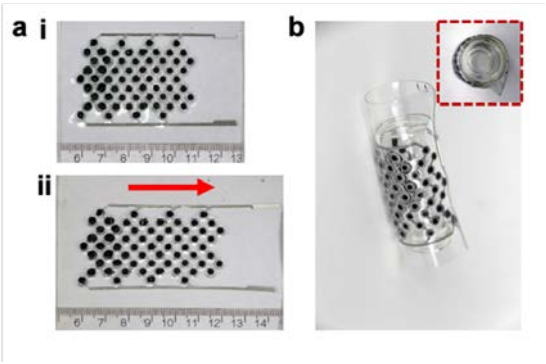

Figure 4.7 Stretchability and bendability of the biofuel cell patch.

To assess the effectiveness of the pellets in limiting the deformation of the electrode section, we employed a camera to record the changes in diameter of the carbon electrode at 40% and 0% strain, respectively. Subsequently, we calculated the ratio of

the electrode diameters in these two states ($D_{40\%}/D_{0\%}$). The raw data of the $D_{40\%}/D_{0\%}$ ratio within a BFC is presented in Table 4.2. The analysis revealed that the changes in electrode diameter were measured to be 99.27±9.61%. This indicates that under a strain of 40% within the BFC, the electrode part remained free from deformation.

Table 4.2 Strain of diameter of electrodes. When the BFC was with a strain of 40%, the change in diameter of electrodes was 99.27±9.61%.

$D_{0\,\%}$ (cm)	$D_{40\,\%}$ (cm)	$D_{40\,\%}/D_{0\,\%}$	$D_{0\,\%}$ (cm)	$D_{40\,\%}$ (cm)	$D_{40\,\%}/D_{0\,\%}$
0.159	0.245	154.09	0.278	0.255	91.73
0.283	0.26	91.87	0.278	0.276	99.28
0.303	0.281	92.74	0.283	0.266	93.99
0.288	0.266	92.36	0.288	0.271	94.10
0.278	0.292	105.04	0.283	0.292	103.18
0.263	0.266	101.14	0.268	0.25	93.28
0.278	0.245	88.13	0.274	0.261	95.26
0.263	0.271	103.04	0.298	0.281	94.30
0.313	0.281	89.78	0.278	0.281	101.08
0.248	0.255	102.82	0.263	0.255	96.96
0.263	0.276	104.94	0.268	0.255	95.15
0.283	0.25	88.34	0.258	0.255	98.84
0.264	0.261	98.86	0.258	0.245	94.96
0.263	0.26	98.86	0.258	0.255	98.84
0.288	0.271	94.10	0.293	0.297	101.37
0.273	0.276	101.10	0.283	0.255	90.11
0.288	0.261	90.63	0.283	0.255	90.11
0.278	0.266	95.68	0.288	0.266	92.36
0.258	0.26	100.78	0.273	0.266	97.44
0.293	0.292	99.66	0.273	0.261	95.60
0.303	0.307	101.32	0.268	0.255	95.15
0.273	0.281	102.93	0.273	0.25	91.58
0.293	0.281	95.90	0.273	0.266	97.44
0.303	0.287	94.72	0.268	0.292	108.96

0.278	0.266	95.68	0.248	0.246	99.19
0.248	0.266	107.26	0.253	0.245	96.84
0.278	0.271	97.48	0.263	0.245	93.16
0.248	0.266	107.26	0.264	0.271	102.65
0.249	0.266	106.83	0.248	0.302	121.77
0.273	0.281	102.93	0.258	0.318	123.26
0.288	0.271	94.10	0.268	0.266	99.25
0.243	0.255	104.94	0.278	0.281	101.08

4.3.3 Electrochemical Performance of Stretchable Liquid Metal-Based Biofuel Cells

The CV method was employed to estimate the electrochemical active surface area (ECSA) of the electrode (Figure 4.8 a). To enhance the electrical performance of the device, a layer of PANI was electrochemically polymerized on the electrode using cyclic voltammetry, ranging from -0.2 V to 1.0 V for 25 cycles (Figure 4.8b). A three-electrode system was utilized, with the carbon electrode immersed in 0.1 M aniline and 1 M HCl solutions and connected to an Ag/AgCl reference electrode and Pt counter electrode. PANI, which exhibits multiple redox states and pseudocapacitance traits, facilitated the transfer of electrons from enzymes to conductors. Subsequent to the coating process, the current density of the electrode increased, indicating enhanced conductivity (Figure 4.8c). The PANI nanowire structure was positioned at the top of the carbon electrode, effectively filling the gaps within it. We hypothesized that the presence of PANI resulted in an increased ECSA by filling the carbon electrode gaps, while the nanostructure further facilitated direct electron transfer from enzymes to electrodes. The ECSA of the carbon electrode was characterized both before and after the PANI coating. By evaluating the slope of the current density curves at 0.0 V against scanning rates, the double-layer capacitance per square centimeter (C_{dl}) was determined to be 0.080 μF and 0.500 μF, respectively. The PANI-coated carbon electrode exhibited a higher C_{dl} value (Figure 4.8d).

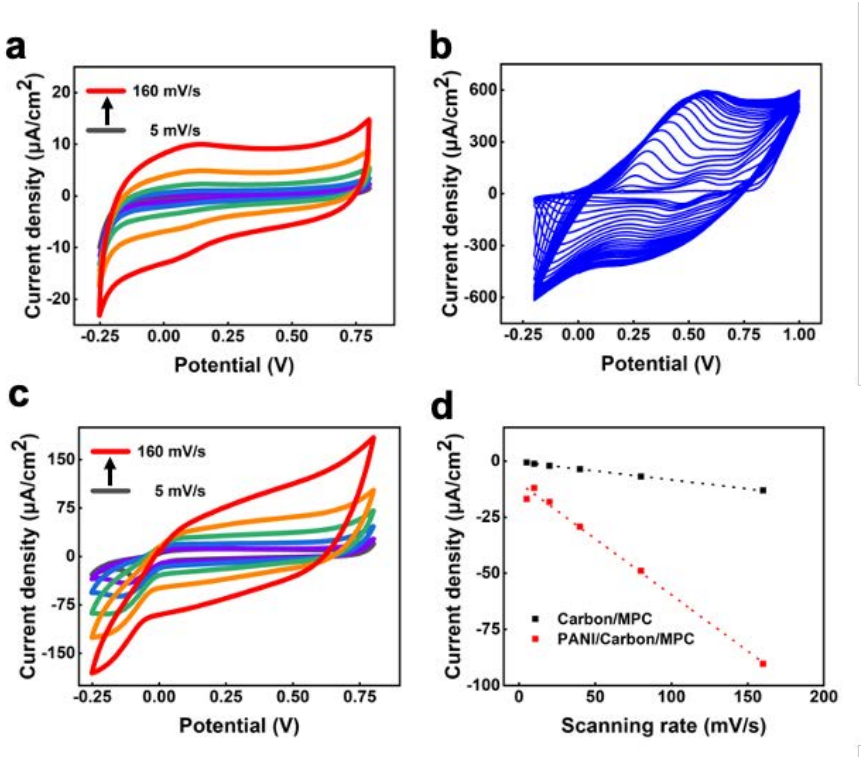

Figure 4.8 Electrochemical performance of electrodes of the biofuel cell. (a) CV of the carbon electrodes (scanning rate at range of 5 $mV \cdot s^{-1}$ to 160 $mV \cdot s^{-1}$); (b) electropolymerization of PANI on the carbon electrodes; (c) CV of the carbon electrode coated with PANI (scanning rate at range of at 5 $mV \cdot s^{-1}$ to 160 $mV \cdot s^{-1}$); (d) Linear fit of current densities of the carbon electrode without/with PANI at 0 V position against scanning rate.

The electrochemical characteristics of the anode were evaluated using an electrochemical workstation. In the bioanodes, modified electrodes containing either GOD or LOx were employed to facilitate electron transfer through the oxidation of glucose or lactate. The enzymes were dissolved in PBS solutions containing bovine BSA. For the glucose-burning biofuel cell, each anode was coated with 2 μL of GOD. Consequently, glucose underwent catalysis by GOD, leading to the production of gluconolactone and the release of electrons (Figure 4.9a). On the cathodes, BOx facilitated the oxygen reduction reaction (ORR) to capture and accept electrons.

Similarly, in the lactate biofuel cell, lactate was converted to pyruvate. The specific half-reaction mechanisms for the biofuel cells are illustrated in Formulas 4.1 to 4.3.

$$Glucose \xrightarrow{GOD} e^- + Glucono\ lactone \qquad (4.1)$$

$$Lactate \xrightarrow{LOx} e^- + Pyruvate \qquad (4.2)$$

$$O_2 + e^- \xrightarrow{BOx} H_2O \qquad (4.3)$$

LSV was utilized to examine the polarization curves of the anodes (containing GOD or LOx) as well as the cathodes, with a scanning rate of 10 $mV \cdot s^{-1}$. The electrodes containing GOD displayed an increase in current until it reached a maximum value of 79 $\mu A \cdot cm^{-2}$ at 0.31 V (vs. Ag/AgCl) when the glucose concentration was raised to 0.2 mM (Figure 4.9b). Given that the concentration of lactate in sweat from a healthy adult is approximately 15 mM, we focused on the outcomes obtained with 15 mM lactate. Interestingly, the results indicated that in the presence of 15 mM lactate, the primary peak was observed at 0.32 V (vs. Ag/AgCl), with a maximum current density of 423.4 $\mu A \cdot cm^{-2}$ (Figure 4.9b), suggesting that lactate oxidation occurred at this potential. To investigate the influence of O_2 the cathodic current density, LSV measurements were conducted on the cathode in both pristine PBS solution and N_2-saturated PBS solution. As demonstrated in Figure 4.9d, the current density at -0.28 V in pristine PBS solution was approximately -100.2 $\mu A \cdot cm^{-2}$. Notably, the reduction peak current density at -0.28 V decreased. However, the current density at -0.28 V increased upon retesting the cathode in pristine PBS (p-PBS) once again (p-PBS, 2nd time). The relationship between cathodic behavior and the level of O_2 indicated the normal functioning of the enzyme (Figure 4.9d).

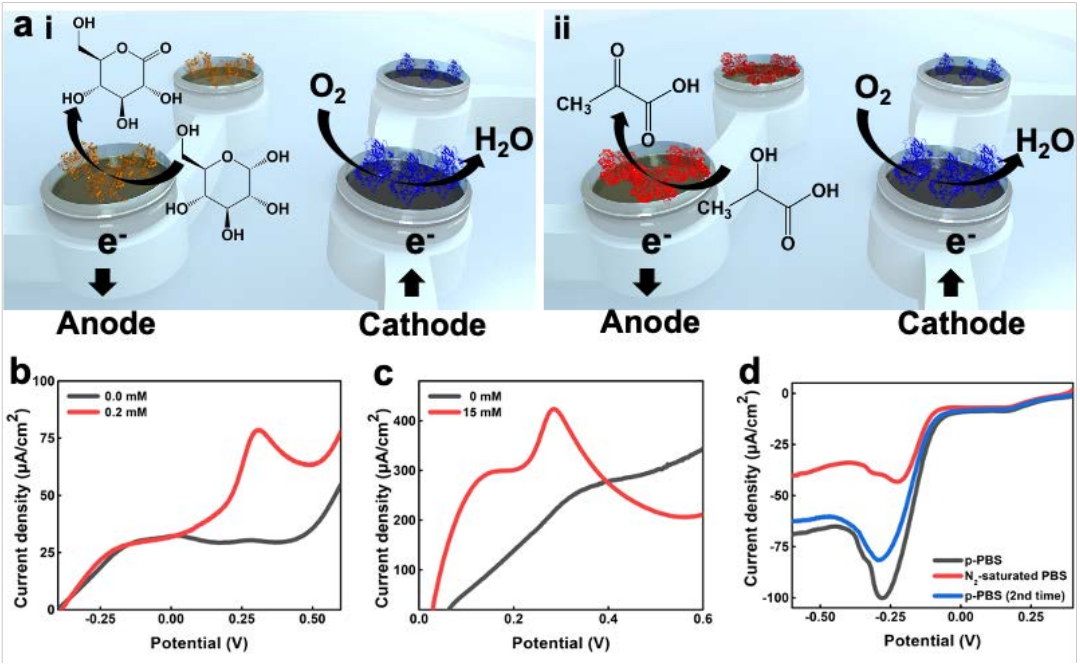

Figure 4.9 Electrochemical performance of anodes and cathodes. (a) mechanism of glucose or lactate biofuel cells; (b) LSV of anodes of glucose biofuel cells (in 0.0 mM and 0.2 mM glucose); (c) LSV of anodes of lactate biofuel cells (in 0 mM and 15 mM lactate); (d) LSV of cathode of glucose biofuel cells (in PBS, N_2 saturated PBS, and return to PBS).

To assess the electrical performance of the glucose biofuel cell, we established a connection between the anode and the working electrode, while the cathode was connected to the reference and counter electrodes. The electrolyte employed was a 1×PBS solution with KCl concentration of 0.5 M and a pH of approximately 7.2. The open-circuit potential (OCP) of the glucose biofuel cell stabilized at an average value of 0.484 V over 5 minutes. To calculate the power density, we utilized Formula 4.4.

$$P = V \times I \qquad (4.4)$$

In this formula, P represents the power density in μW, V denotes the potential in V, and I represents the current in μA. The values for *V* and *I* were obtained from the LSV data. We conducted LSV measurements on the glucose biofuel cell for various glucose

concentrations (0.2, 0.4, 0.8, 1.6, and 3.2 mM). As shown in Figure 4.10a, the current density increased proportionally with the glucose concentration. Although the power density trend of the glucose biofuel cells exhibited a mild increment with increasing glucose concentration (Figure 4.10b), we focused particularly on the results obtained with a glucose concentration of 0.2 mM as it closely approximated the average value found in a healthy adult. Analyzing the LSV curve and employing Formula 4, we determined that the potential of 0.31 V corresponded to the maximum power density of 14.11 $\mu W \cdot cm^{-2}$. Concurrently, the CV curve demonstrated that with 0.2 mM glucose, the cell attained a maximum current density of 80 $\mu A \cdot cm^{-2}$ at 0.31 V (Figure 4.10d).

In lactate biofuel cells, there was a positive correlation between the peak current density of the bioanodes and the concentration of lactate. As shown in Figure 4.10e, as the concentration of lactate increased from 0 mM to 20 mM, the current density at the oxidizing peak (0.31 V) also increased. Moreover, the power density of the lactate biofuel cell exhibited a similar trend, increasing with higher lactate concentrations (Figure 4.10f). Considering that 15 mM lactate closely approximates the average value found in sweat from a healthy adult, we focused on the results obtained with a concentration of 15 mM lactate. In this case, the lactate biofuel cell exhibited an OCP of 0.73 V. At a potential of 0.51 V, the lactate biofuel cell achieved a maximum power density of 31.00 $\mu A \cdot cm^{-2}$ (Figure 4.10g). The CV analysis illustrated that with a concentration of 15 mM lactate, the current density of the biofuel cell was significantly higher compared to the absence of lactate (Figure 4.10h).

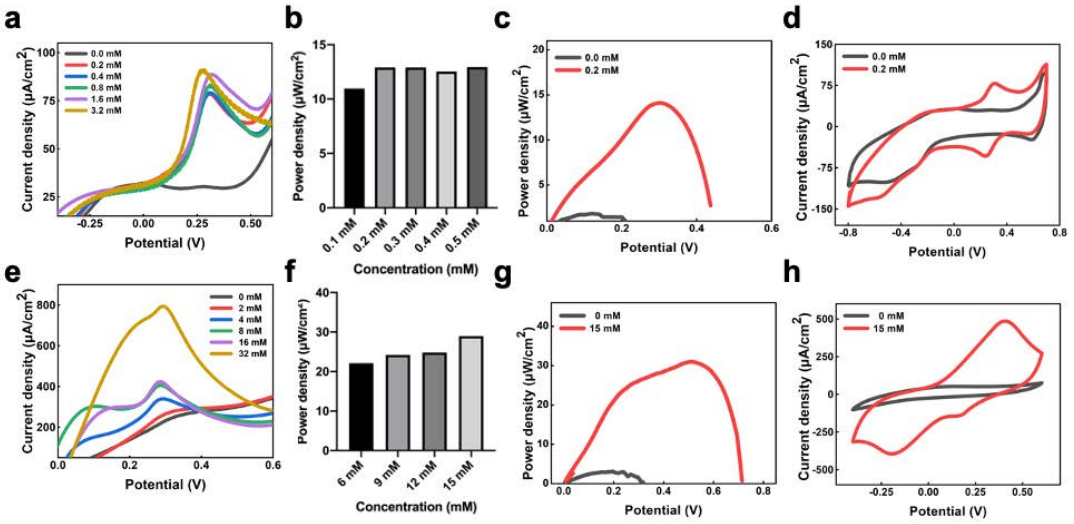

Figure 4.10 Electrochemical performance of glucose and lactate biofuel cells against concentration of substrates (glucose or lactate). (a) LSV of the anode of glucose BFCs against the concentration of glucose; (b) Maximum power density of glucose BFCs with the concentration of glucose of 0.1 - 0.5 mM; (c) power densities of glucose biofuel cell in 0.0 mM and 0.2 mM glucose; (d) CV of glucose biofuel cells (in 0.0 mM and 0.2 mM glucose); (e) LSV of anode of lactate BFCs against concentration of lactate; (f) Maximum power density of lactate BFCs with concentration of lactate of 6-15 mM; (g) power densities of lactate biofuel cell in 0 mM and 15 mM lactate; (h) CV of lactate biofuel cells (in 0 mM and 15 mM lactate);

The objective of our investigation was to assess the stretchability of the biofuel cell. Upon initiating strain, we observed a noticeable shift in the position of the maximum power density, as depicted in Figure 4.11a. As the biofuel cell experienced a strain of 30%, we observed a minimal increase in the maximum power density, accompanied by a slight decrease in the open circuit potential, as illustrated in Figure 4.11b. We hypothesized that these changes may be attributed to a reduction in the internal resistance of the MPC. Specifically, despite the strain of 30%, the maximum power density value remained constant at 8.4 $\mu W \cdot cm^{-2}$.

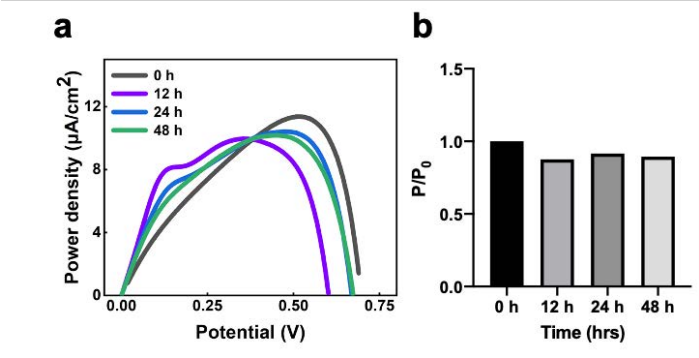

Figure 4.11 Stability of the biofuel cells against time. (a) Power density curves of glucose BFCs in 0, 12, 24, and 48 hrs; (b) the power efficiency of glucose BFC in 0, 12, 24, and 48 hrs.

We investigated the stability of the biofuel cell. Specifically, we assessed the power density of the glucose biofuel cell with an electrolyte containing 0.2 mM glucose, as presented in Figure 4.12a. It was observed that as the usage time increased, the maximum power density exhibited a decrease. After 48 hours, the power density remained at 89% of its original value (Figure 4.12b).

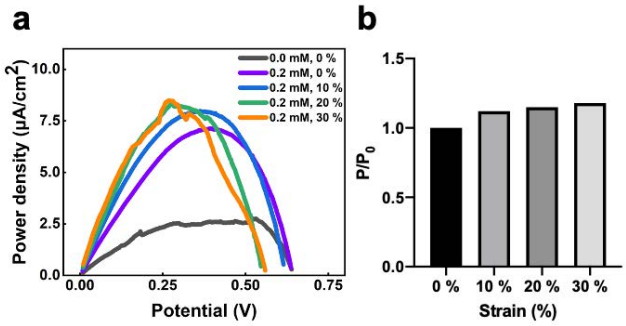

Figure 4.12 Stability of the biofuel cells against strain. (a) Power density curves of glucose BFCs with strains of 0 %, 10 %, 20 %, and 30 %; (b) the trend of power efficiency of glucose BFC with strains of 0 %, 10 %, 20 %, and 30 %.

Furthermore, we conducted an examination of the short circuit current of the lactate biofuel cell. This evaluation was carried out in a stationary electrolyte solution containing 32 mM lactate, which ensured a sufficient supply of substrate for the

catalysts (Figure 4.13). The results indicated that the current density reached its maximum value of 93 μA·cm^{-2} at the 12th minute, but progressively decreased to zero by the 6th hour. However, when the electrolyte solution was stirred and the substrate at the electrode interface was replenished, the current density recovered to 18 μA·cm^{-2}. Interestingly, a gradual decline in current density was observed after the 21st hour. Importantly, the patch demonstrated satisfactory durability for 21 hours, which is sufficient for a single-day application.

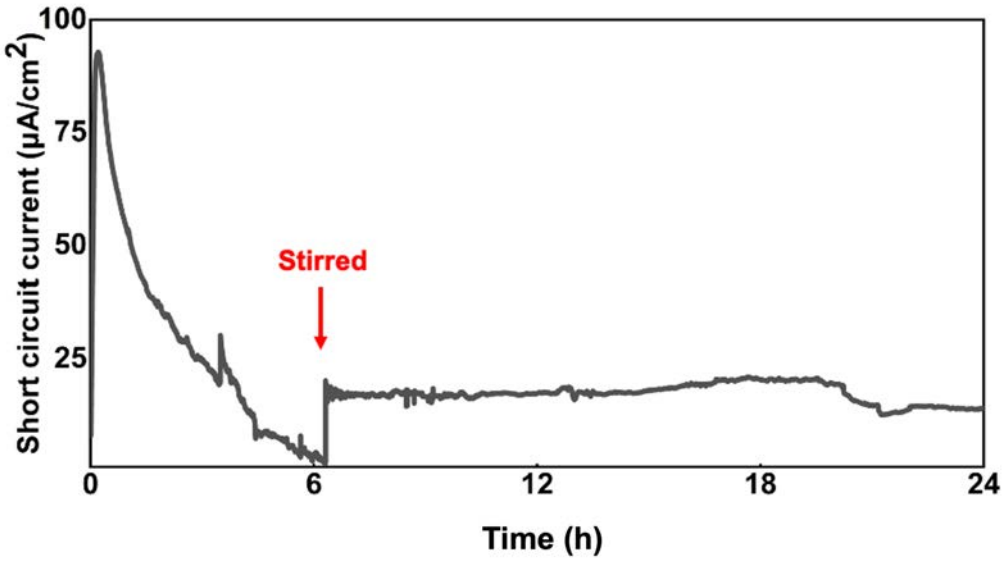

Figure 4.13 Short circuit current of the lactate biofuel cell with 32 mM lactate for 24 hrs.

4.3.4 Application of Stretchable Liquid Metal-Based Biofuel Cells

To further explore the potential application of biofuel cells in wearable devices, we conducted an integration of biofuel cells with an energy harvesting module for sensor power. Considering the insufficient output voltage of the fuel cell alone to meet the typical operating voltage range of wearable electronic modules (usually 3-5 V), we connected a low-power energy harvesting module (Figure 4.14) to the biofuel cell. This enabled continuous collection and storage of electricity generated by the biofuel cell. To simplify terminology, we referred to this combination of the energy harvesting

module and the biofuel cell as the power supply module. The voltage output of the power supply module reached 4.6 V, which met the power supply requirement of the wearable electronic module. This configuration was utilized to illuminate LEDs and power various modules such as the body temperature module, blood oxygen module, and heart rate module (Figure 4.15a, d).

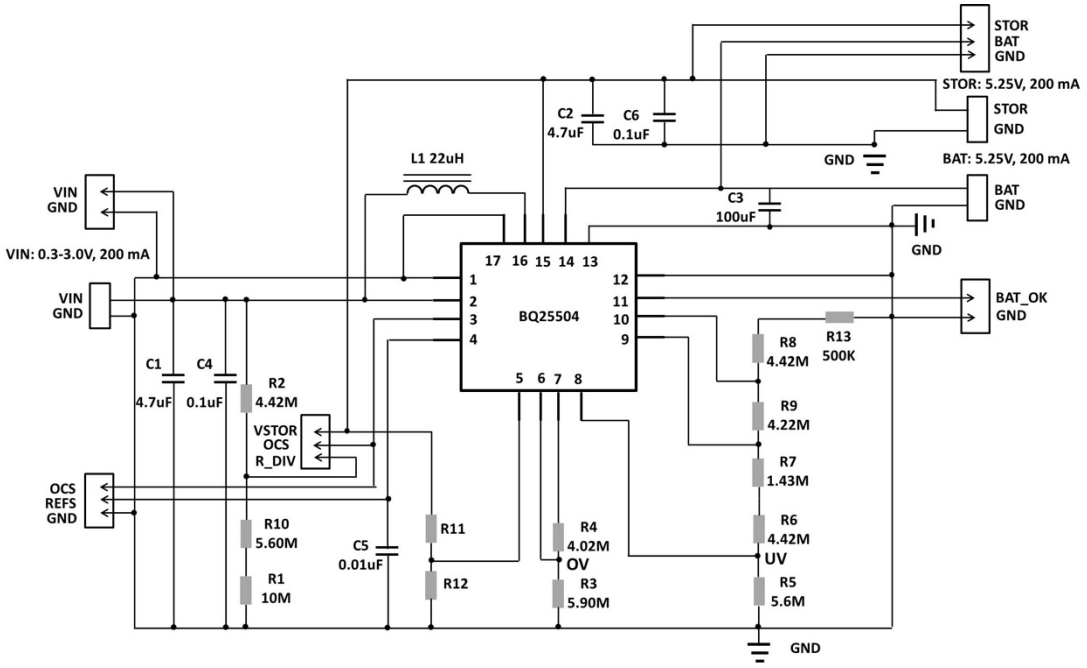

Figure 4.14 Circuit of the low-power energy harvesting module.

The power supply module was integrated with wearable sensors and positioned on the subject's arm to collect data before and after exercise (Figure 4.15d). The results demonstrated a decrease in blood oxygen levels after exercise (Figure 4.14b), an increase in skin surface temperature from 30.4 ^{o}C to 33.7 ^{o}C (Figure 4.15c), and an elevation in heart rate from an average of 74 beats per minute (b.m.p.) to an average of 112 b.m.p. (Figure 4.15e), which was also confirmed by photoplethysmography (PPG) signals (Figure 4.15f). These observed trends in the data align with our expectations. In future research, we anticipate using the biofuel cell to power additional wearable electronic modules, thereby achieving a highly integrated system for detection and analysis.

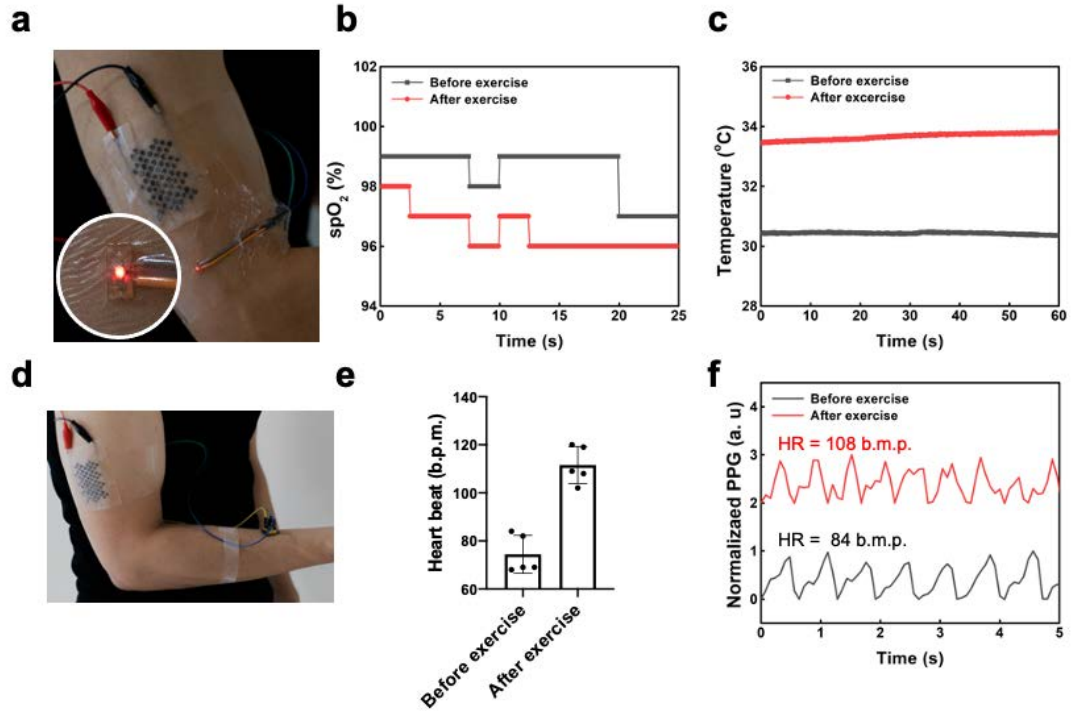

Figure 4.15 Application of biofuel cells. (a) A LED lightened by the liquid metal-based biofuel cells; (b) spO_2 data (c) temperature (e) the heart rates and (f) PPG signals of the subject before and after exercise of the subject before and after exercise (d) the photo of the subject wearing the liquid metal-based biofuel cell and the oximeter module.

4.4 Conclusions

In this chapter, we propose a straightforward method for developing wearable biofuel cells using the screen-printing technique. The biofuel cells are created by screen-printing highly conductive MPCs onto a PDMS substrate. These MPCs exhibit excellent electrical conductivity (2.7×10^5 $S\cdot m^{-1}$), ensuring optimal performance of the biofuel cells. Moreover, their exceptional biocompatibility and stretchability (with a strain exceeding 200%) allow the bio-interface to effectively conform to human skin. To enhance the stretchability of the carbon electrodes, additional pellets made of PDMS were introduced on the backside of the electrodes. This incorporation of PDMS pellets allowed the carbon electrodes to retain their shape even when subjected to a strain of 40%. By modifying glucose oxidase or lactate oxidase, we fabricated glucose biofuel

cells and lactate biofuel cells, respectively. with 0.2 mM glucose, the glucose biofuel cell attained a maximum power density of 14.11 $\mu W \cdot cm^{-2}$. With the lactate concentration of 15 mM, the lactate biofuel cell achieved a maximum power density of 31.00 $\mu A \cdot cm^{-2}$. We successfully utilized the fabricated biofuel cells to power wearable sensors, such as temperature, oximeter, and heart rate sensors, for monitoring physical metrics of subjects during exercise. In the future, these biofuel cells have the potential to be integrated into more stretchable wearable analytical electronic devices, such as electronic tattoos, epicardial pacing wires, and displays. This integration would enable them to serve as sustainable and environmentally friendly power sources.

Chapter 5 Air-Permeable Liquid Metal-based Sweat Biofuel Cells

This chapter delves into the utilization of air-permeable electrospun mats in the development of an air-permeable sweat biofuel cell, utilizing liquid metal as its foundation. In contrast to the previous chapter, this study incorporates 3D stretchable sponge-like carbon electrodes (SLCEs), which offer a larger specific surface area for enhanced electrochemical reactions and increased active site availability. Furthermore, the porous structure of the SLCEs facilitates the effective attachment of enzymes and mediators, reducing the loss of active substances and prolonging the overall lifespan of the cell. Similar to previous chapters, this section conducts thorough characterizations of the air-permeable liquid metal-based sweat biofuel cell, focusing on morphology, mechanical performance, electrochemical performance, and breathability properties. Finally, the strain sensor and the air-permeable liquid metal-based sweat biofuel cell are interconnected in a series arrangement, recording current signals to determine the deformation of the strain sensors and enabling gesture recognition.

5.1 Introduction

In the past twenty years, significant research efforts have focused on the development of flexible and stretchable electronics, particularly in improving the flexibility, stretchability, conductivity, and reliability of high-performance conductors. However, the influence of breathability on wearing comfort, which can have a direct impact on user satisfaction, has often been disregarded. The conductors used in wearable and skin electronics commonly consist of water-impermeable elastic films.[20, 218] In normal circumstances, the human body regulates temperature by continuously evaporating sweat from the skin's surface into the surrounding environment in the form of water vapor. This process typically occurs at a rate of approximately 200-600 $g \cdot m^{-2} \cdot day^{-1}$. When the device is attached to the skin and tissue surface for a long time, it will cause thermal physiological discomfort, such as stickiness, moisture, and even inflammation. Thus, when designing flexible stretchable conductors, their permeability to gases, water

vapor, and liquids needs to be considered. Previous studies in the field of textiles and films have established that the permeability of air and water vapor in materials is primarily determined by their geometric structure, including factors such as thickness and porosity. Additionally, the permeability to water vapor and liquids is influenced by material properties, which can be altered to achieve liquid permeability by rendering the conductors hydrophilic. The ability of a material to allow the passage of liquids can be assessed by its wettability, while the permeability of water vapor is typically evaluated using the water vapor transmission rate (WVTR).[161] The WVTR measures the quantity of water vapor that passes through a material within a specific timeframe. In the context of wearable and on-skin electronics, it is desirable for the WVTR to exceed 200 $g \cdot m^{-2} \cdot day^{-1}$ to ensure normal skin respiration without obstruction.

Permeable and stretchable conductors can be developed through two primary methods: (1) using fiber materials and (2) manipulating the porosity of film-type conductors. Fiber materials are composed of fiber aggregates with high aspect ratios and diameters ranging from nanometers to millimeters. Depending on their structure, flexible conductors made from fiber materials can be classified into three categories: one-dimensional linear conductors, two-dimensional fabric conductors, and nanofiber membranes. Given the objective of our project to enable flexible electronic sensing both internally and externally, it is essential for the conductors to conform to the in vitro skin and adapt to millimeter-scale blood vessels within the body. Our specific area of interest is controlling the permeability of nanofiber membranes. These membranes serve as temporary templates for the creation of flexible and stretchable conductor networks (Figure 5.1a)[219] and as base materials for permeable stretchable conductors (Figure 5.1 b). Typically, soluble polymers like PVA are employed as temporary nanostructure templates to build flexible conductor networks. Subsequently, a thin layer of metal, such as Au, Cu, Ag, or Al, is deposited onto the nanofiber membrane. Afterward, the nanofiber film is dissolved, leaving behind a transparent, flexible metal nanonetwork.[219] The resulting gold nanonetwork displays a maximum strain capacity of 48% and experiences only a threefold increase in resistance (at a strain rate of

approximately 40%) after nearly 10,000 cycles of tensile and bending experiments. In moisture permeability experiments, the gold nanonetwork exhibits similar performance to the uncoated control group, demonstrating excellent air and water vapor permeability without hindering sweat evaporation. Elastic materials like styrene-butadiene-styrene (SBS), polyurethane (PU), and PDMS can be electrospun into nanofiber membranes with porous structures, endowing them with elasticity. By integrating various conductive materials, such as metals, carbon-based substances, and conductive polymers, into these elastic nanofiber membranes during or after the electrospinning process, it is possible to create permeable and stretchable conductor composites. These composites hold potential for applications in epidermal electronics and electronic tattoos. Ag nanowires can be distributed within nanofiber membranes using vacuum filtration, spraying, screen printing, and other techniques, resulting in the formation of conductive fiber membranes.[220] An alternative approach involves electrospinning TPU elastic nanofibers and utilizing electrospray with AgNW dispersion to introduce metal conductors into the nanofibers.[221] This layered structure enables the composite nanofiber mat to possess remarkable properties, such as high electrical conductivity (4.8×10^5 $S\cdot m^{-1}$), exceptional stretchability (500 %), sustained performance during extended strain deformation over 30,000 cycles at 50% strain, and durability in washing tests. The composite mat also exhibits significant air permeability with a value of 5.6 $cm^3\cdot s^{-1}\cdot cm^{-2}$. Furthermore, the nanofiber membrane can be immersed in a solution containing a metal precursor, facilitating uniform coating of the metal around the fiber membrane's surface and within the gaps between the fibers through chemical reduction. The resulting SBS nanofiber mat coated with AgNPs demonstrates high conductivity (5.4×10^5 $S\cdot m^{-1}$) even under substantial deformation (2.2×10^5 $S\cdot m^{-1}$ at 100% strain).[222, 223]

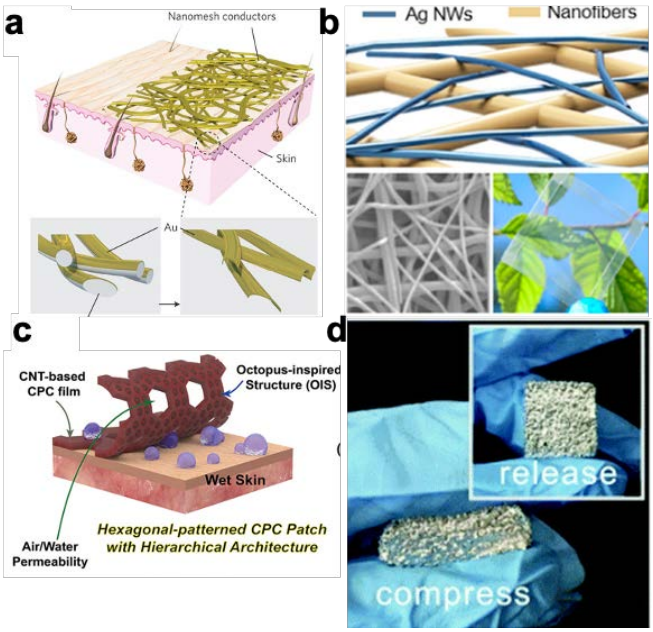

Figure 5.1 Preparation method of permeable stretchable conductor; (a) the nanofiber membrane is used as a temporary template to form a flexible or stretchable conductor network;[219] (b) the nanofiber membrane is used as a base material for a permeable stretchable conductor;[220] (c) the template is used as a porous mold or scaffold;[224] (d) easily soluble materials can be used as sacrificial templates for preparing porous film conductors.[27]

The air and water permeability of dense elastic materials like SBS, PU, and PDMS is limited, resulting in poor physiological comfort. However, by employing structural modification techniques such as kirigami structures and templating methods, it is possible to create pores with controllable dimensions (ranging from microns to millimeters) within the conductor. This allows for gas and water penetration while maintaining the desired characteristics of flexibility, stretchability, and conductivity. Kirigami structures, as discussed earlier, have been applied in the field of stretchable electronics. Additionally, porous film conductors can be manufactured using templates as porous molds or scaffolds (Figure 5.1 c).[224] By selectively dissolving or stripping the components in the film, a network or porous structure can be obtained. For instance, a highly permeable, stretchable, and adhesive hierarchical mesh conductive electrode can

be created by directly casting a mixed solution of PU and conductive materials (such as CNT or Ag flakes) onto a PDMS master mold with a hexagonal structural pattern. After curing and removal of the electrode, an elastic film with a hexagonal network structure is obtained. This film demonstrates durability through 1000 stretch-release cycles under 100% strain and exhibits water permeability and stable electrical conductivity. Furthermore, easily soluble materials like salt crystals, sugar cubes, metal oxides, and ice can serve as sacrificial templates for producing porous thin film conductors.[225] For example, porous PDMS sponges have been developed by dissolving sugar cubes in an elastomeric matrix (Figure 5.1d).[27] These sponges can be further made conductive using methods like the PAMD approach or vacuum filling with a liquid metal. These strategies offer the potential to create permeable and stretchable conductors with improved comfort and functionality, making them suitable for various applications in the domain of stretchable electronics.

Herein, we reported an air-permeable liquid metal-based biofuel cells (BFCs) by using electrospun mat as substrate material, liquid metal-polymer composite as stretchable conductors, and sponge-like carbon electrodes (SLCEs) as stretchable electrode materials. Such liquid metal-based BFCs could realize energy harvesting as well as air permeability to enhance the power density and wearable comfortability.

5.2 Experimental Section

5.2.1 Fabrication of TPU electrospun mat

A solution was prepared by dissolving 2.25 g of thermoplastic polyurethane pellets in a mixture of 7.169 mL of THF and 6.753 mL of DMF solvents. The solution was subjected to stirring at 60 °C and 500 rpm on a hot plate overnight until complete dissolution was achieved. For the electrospinning process, a voltage of -2.0 kV was applied to the collector, which was rotating at a speed of 200 rpm. Simultaneously, the syringe needle (21G) was set at a voltage of 18.0 kV. The distance between the collector

and the syringe needle tip was maintained at 15 cm. The electrospun mat was fabricated by continuously extruding the solution at a controlled flow rate of 1 $mL \cdot h^{-1}$ for a total duration of 8 hours.

The polyvinyl alcohol (PVA) electrospun mat was fabricated with a setting voltage of 18 kV. The collector was rotating at a speed of 200 rpm with applied – 2.0 kV potential. The distance between the collector and the needle was 16 cm. The flow rate of the PVA solution (9% in DI water) was 0.7 $mL \cdot h^{-1}$.

5.2.2 Fabrication of MPCs

The MPC ink was prepared by subjecting a mixture of 750 μL of 10% PVB and 750 μL of EGaIn to sonication for 90 seconds. The resultant ink was then screen-printed onto the substrate and subsequently dried in an oven at a temperature of 80 ℃.

5.2.3 Fabrication of SLCEs

The fabrication process of the SLCEs involved the combination of various materials. Specifically, 0.3 g of MWCNT, 0.06 g of graphite, 5.5 g of $NaHCO_3$, 1 g of sugar, 1.5 g of a 27.5% solution of styrene-ethylene/butylene-styrene (SEBS), and 3 mL of toluene were mixed together. The resulting mixture was then placed into a rectangular mold, which was subsequently immersed in ethanol for a duration of one hour. After completing the solvent replacement, the mixture containing the mold was soaked in a 1 M HCl solution to dissolve $NaHCO_3$ and sugar components, thus creating a porous structure within the electrodes. The SLCEs were then cleaned using deionized water and subsequently dried in the ambient environment.

5.2.4 The Assemble of Air Permeable Biofuel Cells

The TPU mat was assembled from a piece of PVA electrospun mat at the electrode area via the thermal trans-printing method. A layer of water-soluble TPU paste was spin-coated on the liquid metal-patterning area at 1000 rpm to encapsulate liquid metal-

polymer conductors (MPC). MPC was screen printing on the spin-coating TPU layer and sandwiched by another spin-coating TPU layer. The SLCEs were cut into a 4 mm × 3 mm piece and glued to the MPC with conductive graphene paste. The device is placed in an ambient environment for drying.

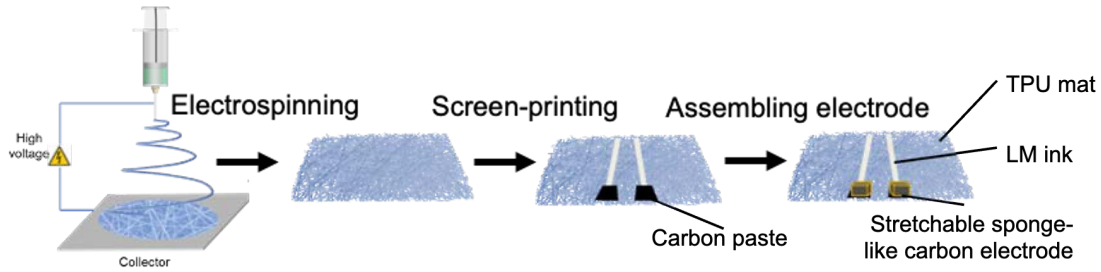

Figure 5.2 Scheme of fabricating permeable sweat fuel cells.

5.2.5 Deposition Au on SLCEs

The SLCEs were affixed onto the TPU mat using carbon paste. Once dried, the assembled electrodes underwent a cleaning process using plasma, followed by the electrodeposition of gold particles from a 5 mM $HAuCl_4$ solution for a total duration of 120 s. Every 20 s, the SLCEs absorbed a fresh solution of $HAuCl_4$. Subsequently, the electrodes were washed with DI water.

5.2.6 Functionalization of Au-SLCEs

The Au-SLCEs were treated with 200 mM 1,4-naphthoquinone dissolved in a solution of EtOH/Acetone with a ratio of 9/1. Subsequently, 10 uL of a LOx solution containing 40 $mg \cdot mL^{-1}$ (with 10 $mg \cdot mL^{-1}$ BSA in PBS) was added. The electrode was allowed to dry, after which 10 uL of 1% glutaraldehyde was used to immobilize the enzyme. A thin film was formed by applying 1% chitosan in 0.1 M acetic acid to encapsulate the enzyme. The functionalized Au-SLCEs were then stored overnight at a temperature of 4 °C.

5.3 Results and Discussions

5.3.1 Morphology of the TPU Mat

The SEM was employed to observe the electrospun fibers in the electrospun mat. These fibers exhibited a random arrangement and were observed to assemble together. ImageJ software was utilized to accurately measure the diameter of the fibers, which was found to be approximately 2 μm. To fabricate an electrospun mat with low batch-to-batch variation and standard deviation, we maintain the electrospinning environment at 20-25 ℃ and with a humidity of 55-65 %. The results showed that the average density of the mat was 0.52 $g \cdot cm^{-3}$, the batch-to-batch variation was 0.059 $g \cdot cm^{-3}$, and the standard deviation was 0.022.

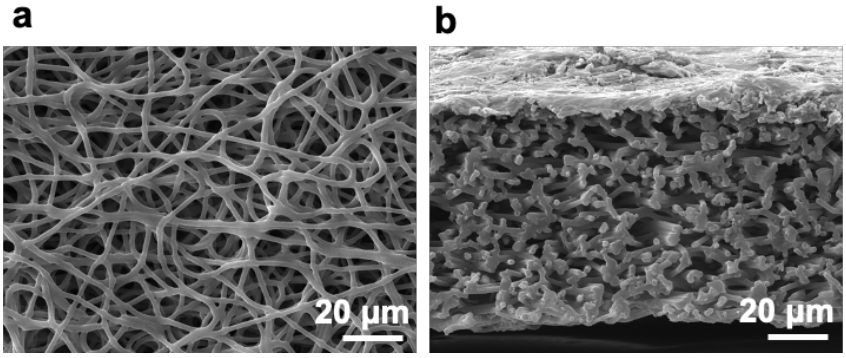

Figure 5.3 SEM photos of TPU mat; (a) top view and (b) cross-section view.

5.3.2 Water Permeability of the TPU Mat

The SEM results revealed that the electrospun TPU mat had a porous structure (Figure 5.2). It was also observed that the electrospun mat allowed for the permeability of water vapor. To further investigate the water permeability of the electrospun TPU mat and a TPU/ PVA) composite mat, a 5-day water permeability test was conducted. In order to facilitate absorption and establish a liquid-solid interface, a portion of the PVA mat was thermally transferred and printed on the electrode area. Six groups, consisting of six subjects each, were set up as follows (1) control group with no cover, (2) TPU mat

group, (3) TPU-PVA mat group with TPU on the top side, (4) PVA-TPU mat group with PVA on the top side, (5) PVA mat group, and (6) commercial TPU patch group. The control group was placed in an artificial environment with a static temperature of 25°C and humidity of 45%, while the TPU mat group was placed in an ambient environment (indoor with air-conditioning) with temperatures ranging from 21-23°C and humidity ranging from 61-67%. In the artificial environment (Figure 5.3b), , the electrospun mat had a water loss of 1273.9 $g \cdot m^{-2} \cdot day^{-1}$, which was also higher than the water loss of the commercial TPU patch (199.5 $g \cdot m^{-2} \cdot day^{-1}$). The water permeability of the PVA mat (1279.6 $g \cdot m^{-2} \cdot day^{-1}$) was slightly higher than that of the other electrospun mats. In the artificial environment (Figure 5.3c), the electrospun mat showed a water loss of 507.7 $g \cdot m^{-2} \cdot day^{-1}$, which was higher than the water loss of the commercial TPU patch (91.2 $g \cdot m^{-2} \cdot day^{-1}$). Overall, the electrospun mats with water permeability were comparable to the control group, indicating that they are suitable for skin-attached substrates, particularly in environments with relatively high humidity.

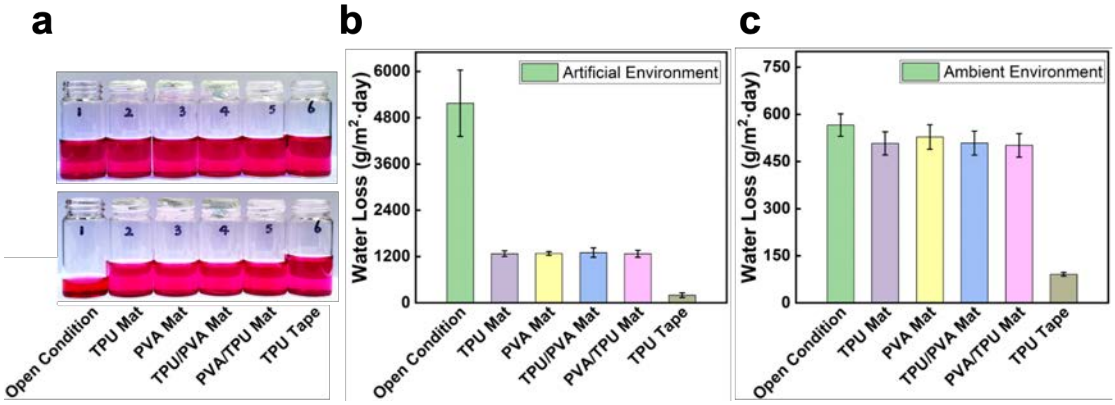

Figure 5.4 Comparison of the permeability of different electrospun mats. (a) Photos of water loss before and after the test; (b)(c) results of water loss in (b) artificial environment (25 °C, 45% humidity) and (c) ambient environment (21-23 °C, 61-67% humidity).

5.3.3 Mechanical Properties of TPU Mat

The mechanical performance of the electrospun TPU mat was assessed and presented in Figure 5.4a. The maximum tensile strain exhibited by the TPU mats ranged from 550% to 875%. The mechanical characterization of the electrospun mat revealed an average tensile strain of 700.90 ± 95.52%. The calculated Young's modulus was 0.44 MPa, which closely approximates the Young's modulus of human skin.

Table 5.1 Mechanical properties of TPU mats

	Unit	Average
Maximum load	(N)	4.13 ± 0.55
Extension at maximum load	(mm)	93.50 ± 13.69
Tensile strain at maximum load	(%)	700.90 ± 95.52
Tensile stress at maximum load	(MPa)	2.17 ± 0.31
The Young's modulus	(MPa)	0.44 ± 0.08

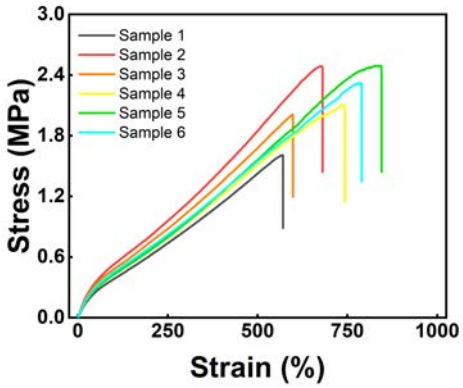

Figure 5.5 Tensile strain of TPU mats.

Cyclic tensile strain tests indicated that the TPU mats subjected to strains of 100%, 200%, 300%, and 400% in the first cycle were unable to fully recover their initial state. The cyclic tensile strain curves showed that during the subsequent 100 cycles, the 2nd cycle and 100th cycle of 300% and 400% differ greatly, indicating that the mechanical properties of the TPU mat are not stable under this stress. Under 100% and 200% stress, the curve difference between the 2nd cycle and the 100th cycle is small. The electrospun

mat displayed a greater likelihood of returning to its original state within a 100% tensile strain range, which is sufficient for accommodating the skin's daily strain values of 0% to 50% [161].

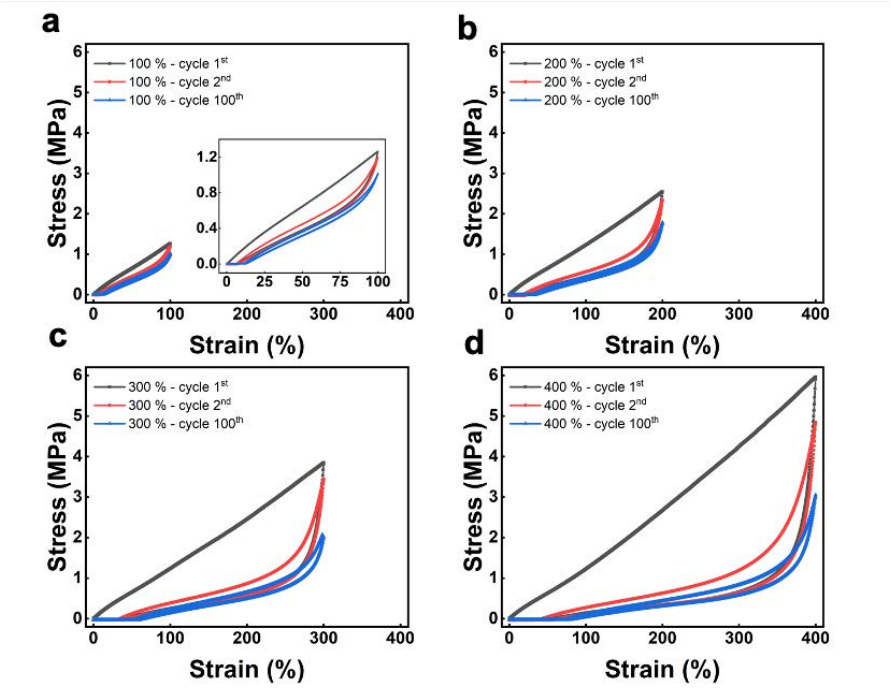

Figure 5.6 Cyclic tensile strain of TPU mat; (a) 100 %, (b) 200 %, (c) 300 %, and (d) 400 % of strain with 100 cycles. The inserted figure showed details of cyclic tensile strain at the strain of 100 %.

5.3.4 Mechanical Properties of SLCEs

The SLCEs employed in this study exhibit notable properties such as flexibility, stretchability, and bendability, as indicated in Figure 5a, b and c. Tensile strain characterization revealed that these electrodes exhibited an average maximum tensile strain of 35.11%, while the stress of 0.426 MPa. The young's modulus of the electrode was 1.19 ± 0.42 MPa. Moreover, a bending test was conducted to simulate the fatigue experienced by conductors during usage, with a bendable radius set at 5 mm. Figure 5.5 c demonstrates that, upon bending, the resistance of the electrode increases until reaching the maximum bending angle and subsequently decreases as the next bending

cycle commences. Remarkably, even after 2000 bending cycles, the resistance of the SLCEs (10 mm × 1 mm × 30 mm) remained consistently between 33 to 34 Ω.

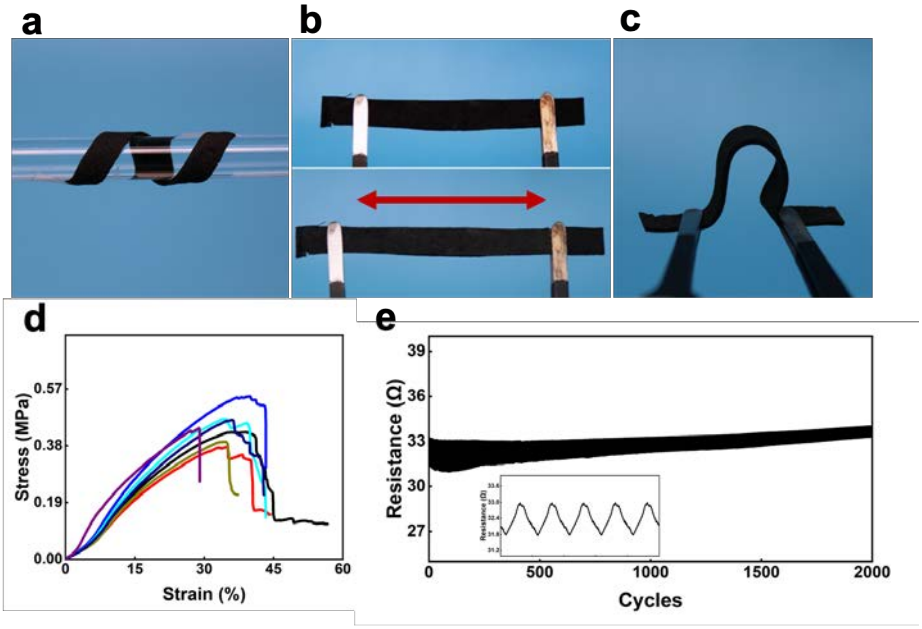

Figure 5.7 Mechanical properties of sponge-like carbon electrodes; the sponge-like carbon electrode was twisted (a), stretchable (b), and bendable (c); (d) tensile strain of the sponge-like carbon electrodes; (e) the resistance of the sponge-like carbon electrode.

5.3.5 Electrochemical Properties of SLCEs

To enhance the current density of the electrode, a technique involving the electrochemical deposition of Au particles was employed on the SLCEs. To assess the electrochemical activity of the electrodes before and after Au deposition, cyclic voltammetry (CV) experiments were conducted using $Fe[CN]_6^{3-}$ solutions(Figure 5.7a). The results of the CV experiments showed that the bare SLCEs did not exhibit clear oxidative peaks but did display a reduced peak at -0.125V. However, upon deposition of Au particles, distinct redox peaks became apparent, and the current response increased by a few times, with the reducing peak shifting to lower potential and the oxidizing peak shifting to higher potential. We used 0.5 M sulfuric acid (H_2SO_4) to acive the electrodes. It is found the current response of the bare SLCEs increased 1-fold

after being active, while the current response of the Au-SLCEs increased mildly. EIS was conducted to evaluate the electrochemical performance of the active Au-SLCEs (Figure 5.7b). Furthermore, to compare the electrochemical active surface area (ECSA) of the Au-SLCEs before/after being active, CV experiments were performed with varying scanning rates (Figure 5.7c). By analyzing the resulting CV curve (Figure 5.7d), an overpotential of -0.3V was chosen for the reduction process. The current observed at -0.3V was plotted against the scanning rate, and a linear fit was obtained. The slope of this linear fit, which is indicative of the ECSA, was found to be larger for the active Au-SLCEs.

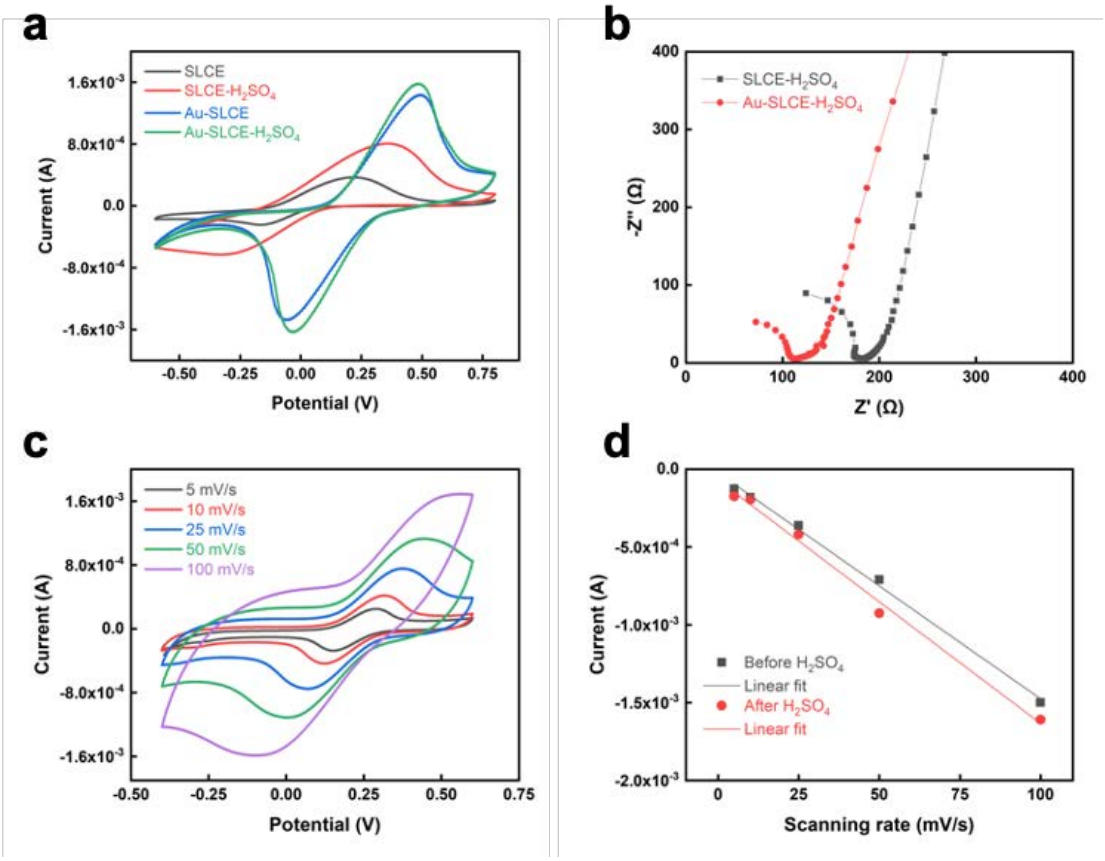

Figure 5.8 Electrochemical performance of the sponge-like carbon electrode; (a) CV of the SLCEs before/after depositing Au and with/without being active with H_2SO_4; (b) EIS of SLCEs and Au-SLCEs after being active with H_2SO_4; (c) CV of the sponge-like carbon electrode against scanning rate; (d) comparison of the electrochemical active

surfaces of the Au-SLCEs before/after being active with H_2SO_4. Tests operated in potassium ferricyanide solutions in a three-electrode system (vs. Ag/AgCl).

5.3.6 Morphology of the Sponge-Like Carbon Electrodes

Utilizing SEM and EDS, the morphology of Au-deposited SLCEs was examined (Figure 5.8). The SLCEs, being three-dimensionally porous and conductive, exhibited distinct diffusion properties for $AuCl_4^-$ ions inside and outside the SLCEs. During the electrodepositing process in a static electrolytic tank under constant potential, it was observed that the deposition of Au particles on the inner SLCEs was hindered. To overcome this, the electrodepositing process was divided into five repeated sections, in which the remaining $HAuCl_4$ electrolyte solution within the SLCEs was eliminated, fresh solution was introduced, and a 20-second electrodeposition was performed at -0.2 V. SEM analysis revealed the presence of particles with a diameter ranging from 1 to 2 μm on the surface as well as the interior of the SLCEs. EDS analysis corroborated that these particles were composed of Au.

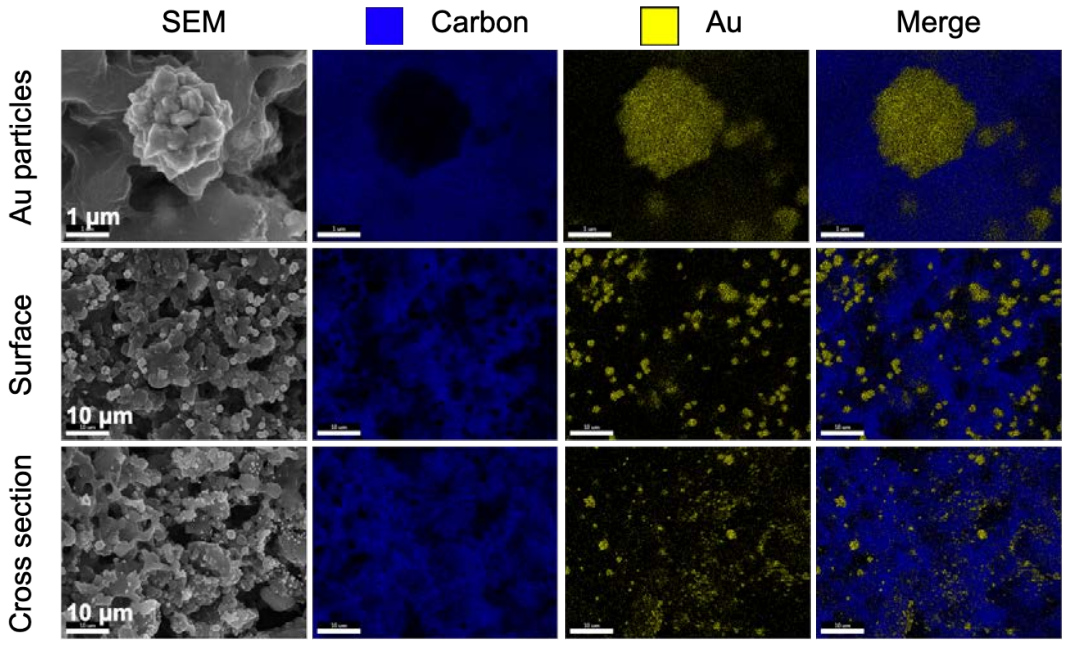

Figure 5.9 SEM photos and EDS of deposited Au on sponge-like carbon electrodes

The macroscopic morphological changes of SLCEs were characterized using optical microscopy in this study (Figure 5.9). The original SLCEs exhibited a black coloration and possessed a rough surface (Figure 5.9a). Electrochemical deposition resulted in significant changes in the surface color of SLCEs, appearing brown to the naked eye (Figure 5.9b). To enable functionalization of the SLCEs, corresponding enzyme solutions were introduced onto the surface, followed by fixation using 1% glutaraldehyde and encapsulation with a layer of 1% chitosan. Following the encapsulation of the enzyme solution, a gel-like material was observed on the surface of SLCEs, exhibiting a brown hue and slight reflectivity (Figure 5.9c).

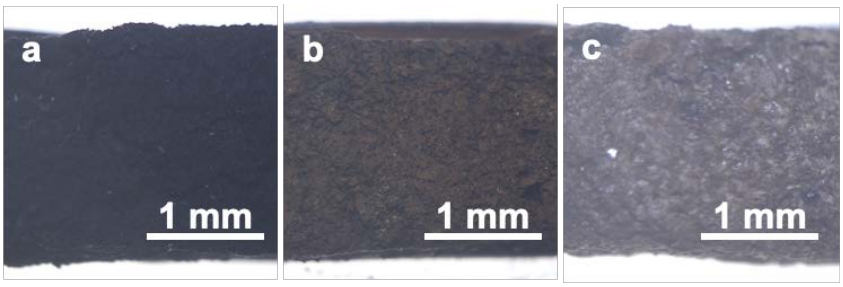

Figure 5.10 Photos of each layer of sponge-like carbon electrode; (a) the sponge-like

carbon electrodes; (b) the sponge-like carbon electrodes were deposited with Au; (c) the Au-deposited sponge-like carbon electrodes were functionalized with LOx and encapsulated with chitosan.

5.3.7 Electrochemical Properties of the Permeable Sweat Biofuel Cells

In this study, we utilized the lactate oxidase and bilirubin oxidase systems as the fundamental mechanisms in sweat fuel cells. The 1,4-NQ was employed as an electron mediator for lactate oxidase in the anodes, while PPIX served as an electron mediator for bilirubin oxidase in the cathodes, additionally controlling the spatial direction of bilirubin oxidase. The CV curves of the anodes were conducted to characterize the redox performance of 1,4-NQ against the increasing concentration of lactate in the PBS solutions. When the lactate increased, realizing by adding lactic acid, the pH of the electrolyte decreased, and both the redox peaks shifted to the right (Figure 5.10a). At the same time, the current response increased as the concentration of lactate increased. At the lactate concentration of 50 mM, with the potential range from -0.3 V to 0.3 V, the electron transfer of 1,4-NQ was close to a reversible reaction. The oxidation of lactate, reduction of oxygen, and polarization curve of the biofuel cells were characterized using LSV. The oxidation of 1,4-NQ occurred at -0.08 V, as depicted in Figure 5.10b, when using a scanning rate of 5 $mV \cdot s^{-1}$ and varying the potential from -0.3 to 0.2 V. In the cathode, the reduction of oxygen took place at -0.375 V in PBS solutions, yielding a maximum current of -900 μA (Figure 5.10c). When oxygen was absent, the maximum reduced current decreased to -35 μA. This decrease in current can be attributed to the porous structure of the SLCE, allowing the internal voids to store a portion of the air.

We evaluated the power density of the fuel cells within a two-electrode system, applying a scanning rate of 5 $mV \cdot s^{-1}$ from the open circuit voltage state to 0 V to obtain the polarization curve. Using the formula:

$$P = V \times I \qquad (5.1)$$

where *P* is the power in W, *V* is the applied potential in V, and I is the current response in A, we determined the power density of the fuel cell, as shown in Figure 5.10d. Compared to the previous work in chapter 4, which achieved a maximum power density of 30 $\mu W \cdot cm^{-2}$ at 0.31 V, this study achieved a higher maximum power density of 219 $\mu W \cdot cm^{-3}$ at 0.123 V. Despite the reduction in potential, the power density was improved. However, the scanning rate of LSV would affect the calculating *P* by changing the *I* which was contributed by the capacitive current from double-layer capacitance.[203] To reduce the impact, a low scanning rate of 2 $mV \cdot s^{-1}$ was chosen to conduct LSV of the biofuel cells. Also, the ion conductivity of electrolytes in the system would affect the current response. To compare the real performance of the biofuel cell in PBS, artificial sweat, and human sweat, we conducted the LSV with the scanning rate of 2 $mV \cdot s^{-1}$ (Figure 5.10 e). The result showed that without lactate and extra KCl ions in the PBS, the power density of the biofuel cell was close to 0, which meant with such set-up parameters, the calculated power density of the biofuel cell was acceptable. The artificial sweat here was with 20 mM lactate and human sweat was with 42.6 mM lactate (detected by assay kit). The power density was increased by the increasing concentration of electrolyte. In particular, the maximum power density of biofuel cells in human sweat was 20.3 $\mu W \cdot cm^{-3,}$ and in artificial sweat was 10.3 $\mu W \cdot cm^{-3}$.

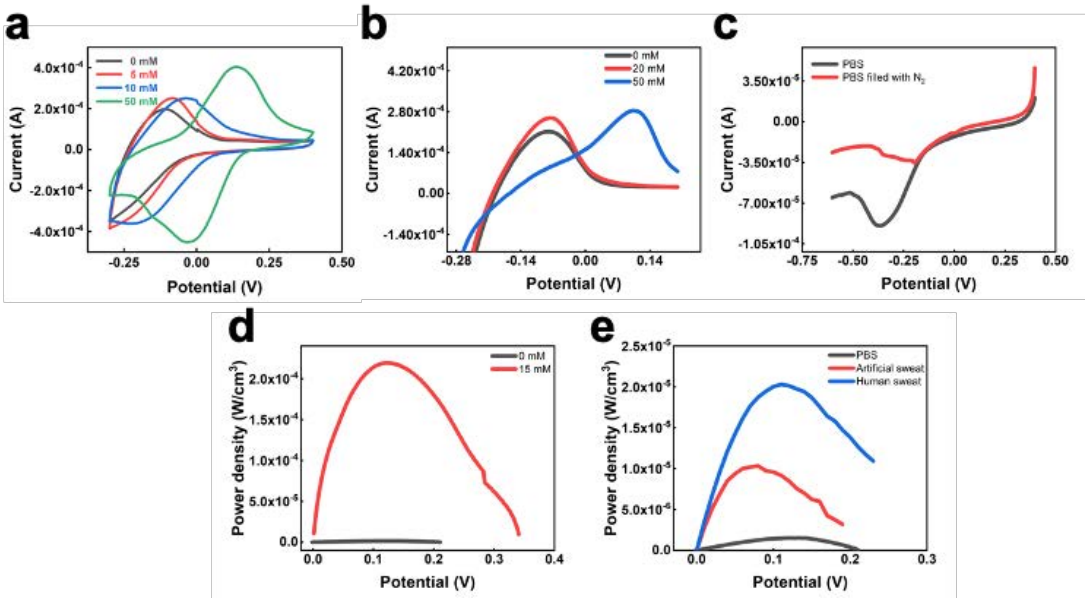

Figure 5.11 Electrochemical performance of anodes and cathodes;(a) CV and (b) LSV of anodes; (c) LSV of the cathode; (d) power density of lactate biofuel cells in the electrolyte of 0.5 M KCl phosphate buffer solutions with 0 mM and 15 mM lactate; (e) power density of lactate biofuel cells in the PBS, artificial sweat, and human sweat.

In the fourth chapter of our study, we established a connection between a biofuel cell and a booster to generate energy for modular electronic components responsible for detecting heart rate, blood oxygen levels, and body temperature. In this chapter, we explore a direct integration of the biofuel cell with a flexible strain sensor for the purpose of achieving gesture recognition. The device consists of a fuel cell (Figure 5.12a), a stretchable MPC resistance acting as the strain sensor (Figure 5.12b), and an external electricity meter for data recording.

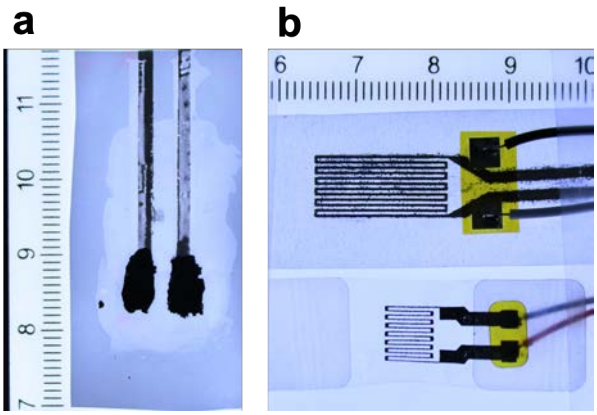

Figure 5.12 Photos of the air-permeable BFCs (a) and strain sensors (b).

Our initial experimentation involved analyzing the resistance variations of the strain sensor when subjected to different levels of strain. Subsequently, we connected the biofuel cell and the strain sensor in series and observed that the current in the circuit decreased proportionally with the increase in deformation (Figure 5.13). The current change per 100 strain was 0.445 ± 0.09 μA. These findings demonstrate the potential application of biofuel cells in strain-sensing technology.

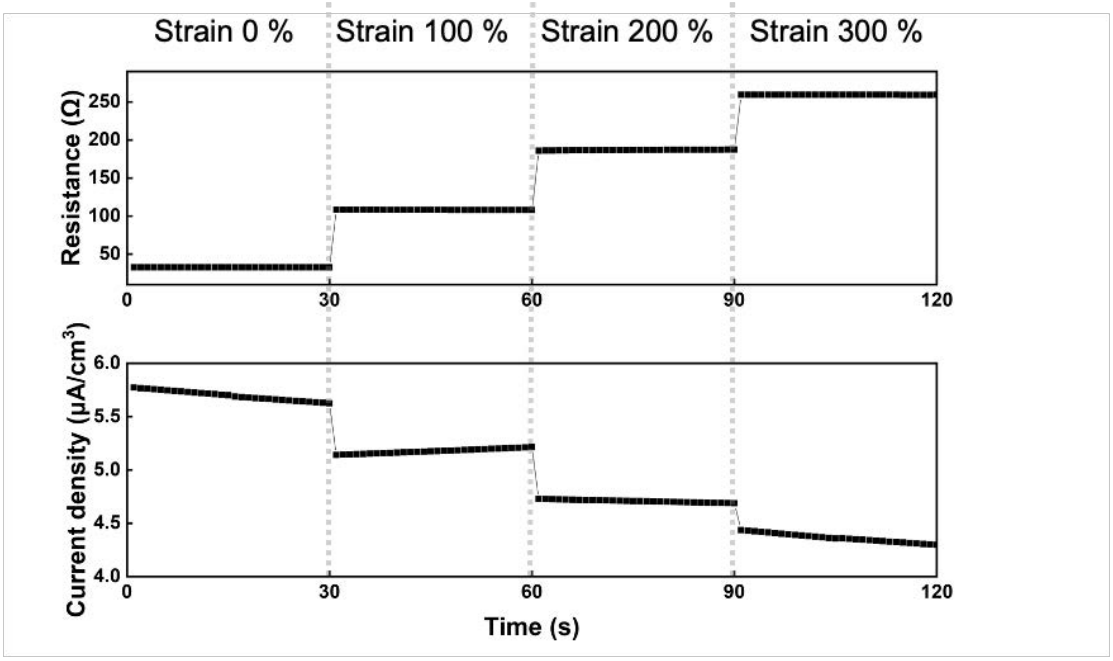

Figure 5.13 Strain sensors powered by biofuel cells.

Moreover, we affixed the strain sensor to the second metacarpophalangeal joint of the index finger and harnessed biofuel cells as an energy source for the sensor (Figure 5.14). Subsequently, we recorded the current flowing through the circuit. By analyzing the data, we observed distinct current responses in three distinct states: no bending at any knuckle, bending one knuckle, and bending two knuckles. This finding suggests that when a strain sensor can generate varying resistance responses to different finger gestures, the circuit, energized by the biofuel cell, can generate corresponding current signals. Considering the nature of biofuel cells, once an electrochemical system achieves stability, a consistent and stable output current can be obtained as long as the fuel supply is adequate, and the catalytic system operates at optimal efficiency. Thus, a wide array of applications in motion capture and human-computer interaction can be envisioned in the future by leveraging highly integrated hardware systems and algorithmic support, such as neural algorithms.

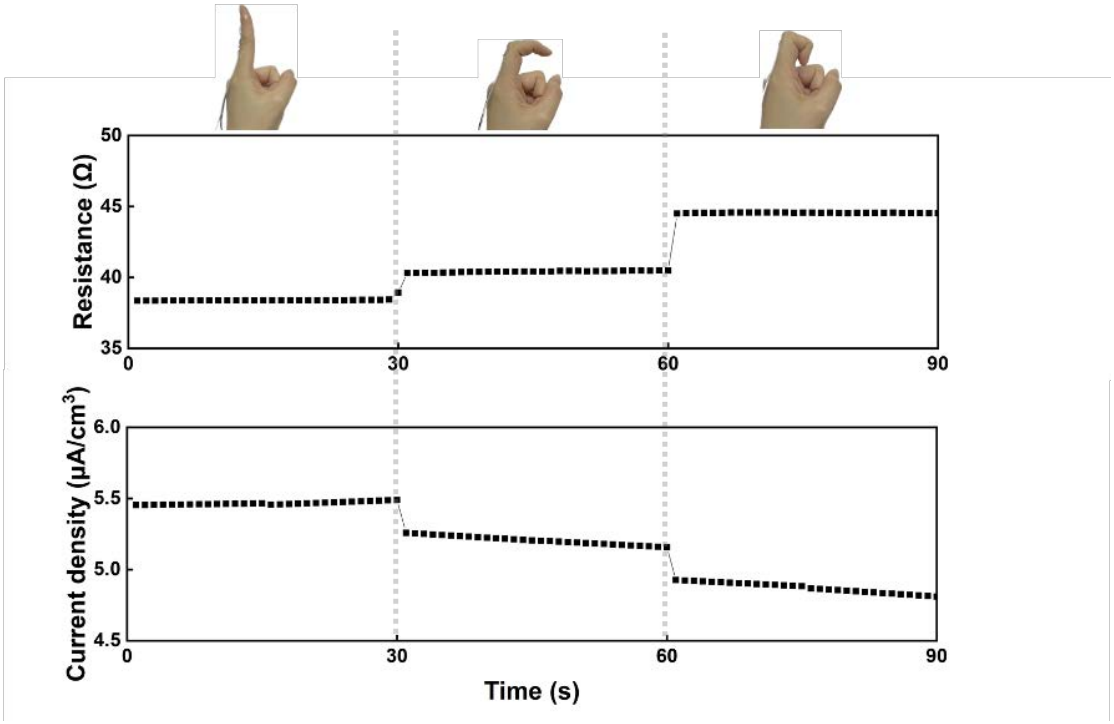

Figure 5.14 The gesture is detected by strain sensors that are powered by biofuel cells.

5.4 Conclusions

To summarize, we successfully developed a stretchable and breathable spinning membrane (1273.9 $g \cdot m^{-2} \cdot h^{-1}$ in 45% humidity, 507.7 $g \cdot m^{-2} \cdot h^{-1}$ in 60% humidity) via the electrospinning technique as a foundational material. Through an etching method, we fabricated sponge-like carbon electrodes with low electrical resistivity (6 $\Omega \cdot mm^{-1}$), high specific surface area, and a certain level of stretchability (tensile strain of 35%). Leveraging these two materials, we constructed sweat biofuel cells with breathable properties. These biofuel cells demonstrated the maximum power density of 219 $\mu W \cdot cm^{-3}$ at a voltage of 0.123V. To harness their potential, we utilized the sweat fuel cell to power strain sensors capable of detecting deformation through changes in current (0.445 ± 0.09 μA for 100% deformation). We directly connected the biofuel cell and the strain sensor in series, with the sensor component attached to the finger joint to detect finger bending by recording the current. Moving forward, this application may

be integrated with neural networks and machine learning algorithms to achieve advanced gesture recognition based on variations in current values.

Chapter 6 Sweat Analysis with Liquid Metal-Based Sensors

In this chapter, we provide a concise overview of the physiological significance associated with the detection of sweat. Additionally, we established a preliminary characterization of human sweat by employing various analytical techniques such as pH meter, ICP-MS, and spectrophotometer. These methods allowed for the quantitative determination of parameters including pH value, glucose, lactic acid, as well as concentrations of Na ions, potassium ions, magnesium ions, and calcium ions within sweat samples. Furthermore, we developed liquid metal-based sweat sensors via a screen-printing process for the purpose of conducting electrochemical analysis of sweat. Due to potential variations in the composition of different sample systems, we proposed the utilization of a dual working electrode method to minimize the impact of individual differences. The electrochemical characterization of the sweat sensors primarily relied on techniques such as EIS, CA, and OCP methods.

6.1 Introduction

Sweat analysis is significant in various fields, including sports science, clinical diagnostics, and wearable technology. The analysis of sweat provides valuable insights into an individual's physiological state, such as hydration levels, electrolyte balance, and metabolic activity. This information can be utilized for optimizing athletic performance, monitoring health conditions, and developing personalized healthcare interventions.

To conduct sweat analysis, several methods are commonly employed. One approach involves collecting sweat samples using non-invasive techniques such as sweat patches or microfluidic devices. These devices are designed to be worn on the skin and can passively collect sweat without causing discomfort to the individual.

Once the sweat samples are collected, they can be analyzed using various techniques. Chemical analysis methods, such as spectrophotometry or chromatography, can be employed to measure the concentration of specific analytes in sweat, such as electrolytes, metabolites, and hormones. Additionally, biosensors can be utilized to detect and quantify analytes in sweat using biorecognition elements such as enzymes or antibodies.

Advances in miniaturization and wearable technology have also led to the development of wearable sweat sensors. These sensors are integrated into wearable devices, such as smartwatches or fitness trackers, and can continuously monitor sweat parameters in real-time. These devices often use non-invasive techniques, such as impedance or sweat rate measurements, to indirectly assess sweat composition and changes over time.

Overall, sweat analysis methods play a crucial role in understanding an individual's physiological condition. Here we use low-cost screen-printing technology to print liquid metal onto flexible substrates to achieve in-situ electrochemical sensing of sweat. Biomarkers tested include glucose, which is related to blood sugar concentration, lactate, which is related to exercise and fitness, and Na^+ and K^+, which are related to the sweat discharge mechanism.

6.2 Experimental Section

6.2.1 Fabrication of MPCs

The MPC ink was prepared by subjecting a combination of 750 μL of 10% PVB and 750 μL of EGaIn to sonication for 90 seconds. The resulting MPC ink was subsequently deposited onto the substrate using the screen-printing technique, followed by drying in an oven set to a temperature of 80 ℃.

6.2.2 Fabrication of Sponge-Like Carbon Electrodes

The sponge-like carbon electrodes were prepared by blending 0.3 g of MWCNT, 0.06 g of graphite, 5.5 g of $NaHCO_3$, 1 g of sugar, 1.5 g of a 27.5% solution of SEBS, and 3 ml of toluene. The resulting mixture was poured into a rectangular mold and subsequently submerged in ethanol for one hour to replace the solvent. After this step, the mixture was immersed in a 1 M HCl solution to dissolve the $NaHCO_3$ and sugar, thereby creating a porous structure. Following a rinse with DI water for cleaning purposes, the sponge-like carbon electrodes were dried in an ambient environment.

6.2.3 Functionalization of Sponge-Like Carbon Electrodes

For glucose sensors, the enzyme solution consisted of 2.5 mL of 200 mM ACES, 2.5 mL of 30 mM hexamine-ruthenium (III) chloride, 1.5 μL of 35 $mg \cdot mL^{-1}$ phenazine ethosulfate, and 800 μL of 1 $kU \cdot mL^{-1}$ glucose dehydrogenase. All components were dissolved or diluted by using PBS. For lactate sensors, the enzyme solution consisted of 40 $mg \cdot mL^{-1}$ lactate oxidase and 10 $mg \cdot mL^{-1}$ BSA in 0.01 M PBS. 10 μL of enzyme solution was introduced to the working electrodes and dried at room temperature. 5 μL of 1 % glutaraldehyde was introduced to the enzyme-modified working electrodes followed by 1 % chitosan solution.

For sodium ionic sensor, the polymer solution of ionic selected membrane consisted of 1 mg Na ionophere X, 0.55 mg sodium tetraki[3,5-bis(trifluoromethyl)phenyl]borate (Na-TFPB), 65.45 mg bis(2-ethylehexyl)sebacate (DOS), 33 mg PVC, and 660 μL cyclohexanone. For potassium sensors, the polymer solution of ionic selected membrane consisted of 2 mg valinomycin, 0.55 mg sodium tetraphenylborate (Na-TPB), 64.7 mg DOS, 32.7 mg PVC, and 660 μL cyclohexanone. 5 μL of polymer solution was introduced into screen-printing working electrodes, while 10 μL being introduced into sponge-like carbon electrodes, followed by drying at room temperature overnight.

To protect the screen-printing referencing electrodes from outside interference, the encapsulated layer, 1 μL of PVB solution, was introduced into the surface of every referencing electrode. The PVB solution consisted of 79.1 mg PVB, 2 mg Pluronic F127, 0.2 mg MWCNTs, 50 mg NaCl, and 1 mL methanol.

6.2.4 Detection of Biomarkers of Human Sweat *in vitro*

Before sweat collection, participants were instructed to cleanse their bodies by either rinsing or scrubbing with clean water. Sweat samples were collected between 15 to 30 minutes following exercise. In specific cases, individuals who had consumed food or ingested a sugar supplement did so 30 minutes prior to exercise, after which sweat samples were obtained.

The concentration of ions present in the sweat samples was analyzed using inductively coupled plasma mass spectrometry (ICP-MS). To facilitate this analysis, the collected sweat was diluted with DI water at dilution ratios of 1000 and 10000. Additionally, the concentration of glucose and lactate within the sweat samples was determined using commercially available assay kits and measured using an ultraviolet-visible spectrophotometer.

6.2.5 Detection of Biomarkers of Human Sweat *in situ*

The sweat sensor was positioned appropriately on the cleansed skin surface. To stimulate sweat secretion, the subject engaged in a 10-minute exercise, which was considered as the baseline (0 min) time. Throughout the experiment, the subject remained stationary while the current response of the glucose and lactate sensors, as well as the open circuit potential of the sodium and potassium sensors, were continuously recorded. Following this, the subject consumed Cola and chocolate. After 10 minutes, the electrochemical signals were recorded for the second time, representing the 10-minute mark. Subsequently, at the 20-minute mark, the subject drank water to

prevent dehydration. Following a 10-minute waiting period, the electrochemical signals were recorded again at the 30-minute mark.

6.3 Results and Discussions

6.3.1 Morphology of the Electrodes of Sweat Sensors

Based on the high permeability of the TPU electrospun mat and the conductive properties of the SLCEs, the sweat sensor was assembled by using MPC circuits, TPU electrospun mat, SLCEs, Ag/AgCl ink, and conductive carbon paste. The sweat sensors were designed for traditional three-electrode system (Figure 6.1). Each MPC had a rectangular shape with a length of 30 mm and a width 1.7 mm, with a gap of 1 mm. Because of the large surface area of the porous SLCEs, the counting electrodes were designed with an area of 108 mm^2 in order to minimize the effect of polarization. The morphology of the electrodes in the sweat sensors was examined by using SEM (Figure 6.1). The porous structure of the SLCEs played a crucial role in enlarging the surface area and increasing the loading mass of active materials.

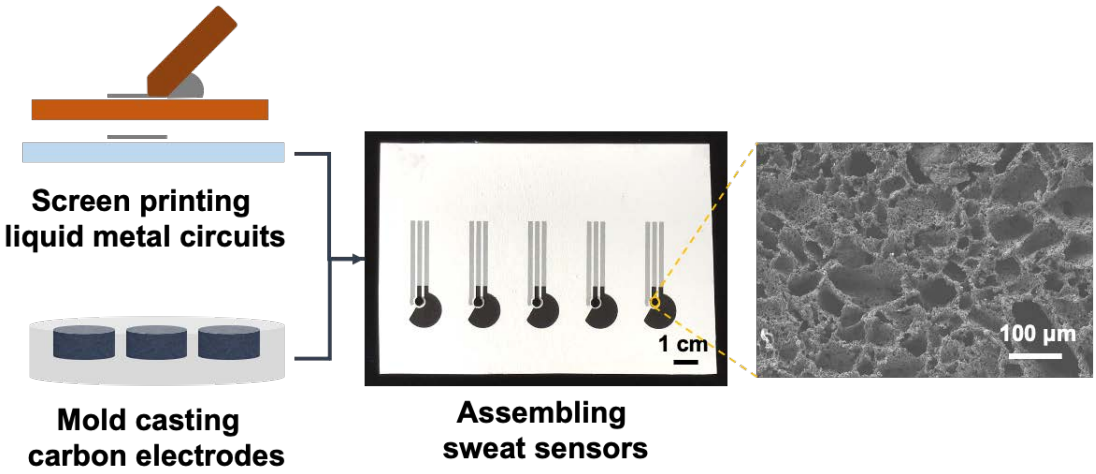

Figure 6.1 Morphology of the electrodes of sweat sensors.

6.3.2 Profile of Human Sweat

To better study the various components in sweat, we collected 12 samples to analyze the common pH value of sweat, sodium, potassium, magnesium, calcium ion concentration, and glucose and lactic acid concentration (Figure 6.2). The preliminary profile of human sweat shows that the pH value of sweat is acidic, with a mean of 4.75 and a median of 4.44. The maximum pH value observed was 5.72. The concentration of lactic acid in sweat was found to be within the range of 4 - 82 mM, consistent with previous literature reports (Table 2.3). The concentration of glucose in sweat was found to be within the range of 16 - 200 μM, which is lower than the detection limit of most commercial glucose sensors designed for blood glucose detection. Thus, the glucose sensor used for sweating detection needs to have a detection limit in the micromolar range.

Sodium ions were found to be one of the most concentrated components in sweat, with concentrations ranging from 52-266 mM. In contrast, the concentration of potassium ions in sweat was much lower, ranging from 10-39 mM. Calcium ions were also detected in sweat, with concentrations ranging from 80-453 μM, with a median of 250 μM. The concentration of magnesium ions in sweat was relatively scattered, with large individual differences, ranging from 76 - 569 μM. No iron ions were detected in the sweat samples.

This data will help expand the existing database of sweat components and provide guidance for further research in this field.

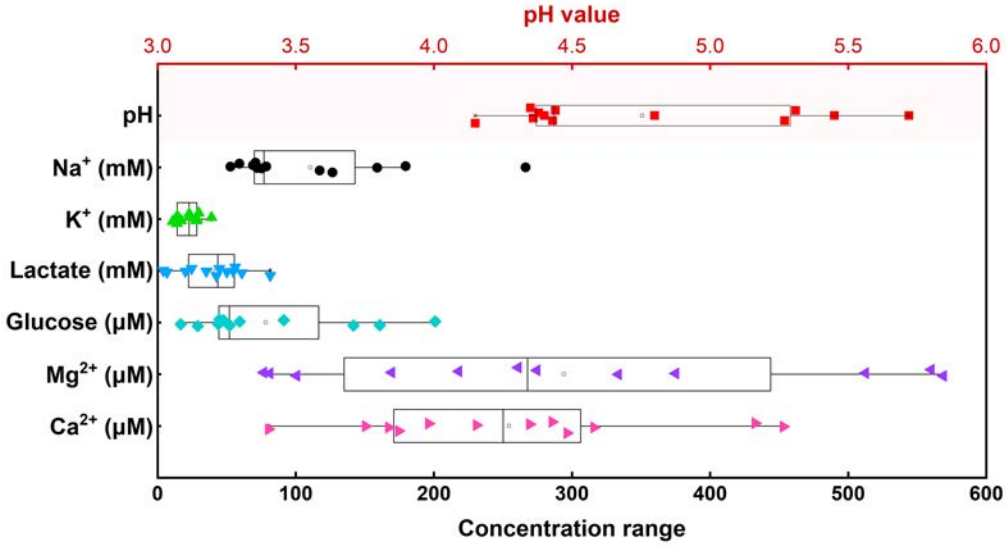

Figure 6.2 Profile of human sweat and twelve samples was analyzed.

To subsequent electrochemical analysis, a standard curve was established by researchers using either PBS or artificial sweat. However, due to the varying formulations of PBS, artificial sweat, and human sweat, the resulting baselines were inconsistent. In this study, we examined the electrochemical performance of biosensors in these three different electrolytes.

6.3.2 Comparison of PBS, Artificial Sweat, and Human Sweat

To evaluate the impedance of the aforementioned electrolytes, EIS was conducted. Figure 6.3 illustrates the values of internal resistance for PBS, artificial sweat, and human sweat. These values are presented as the x-axis intercepts, indicating the starting points of each curve in the figure. The internal resistance values for PBS, artificial sweat, and human sweat were determined to be 57.6 Ω, 92.5 Ω, and 93.5 Ω, respectively (Figure 6.3a). Thus, in many cases, if the PBS solution is used directly as the calibration curve, the current value is likely to be too large, making the calculated marker concentration smaller than the actual value. Compared with artificial sweat and human sweat, the impedance values are very close, but there are no potassium ions in artificial sweat (Figure 6.3b). Considering there are different artificial sweat formulas, thereby

we compared internal resistance of four types of artificial sweat (Figure 6.3c). We separately tested PBS and four types of artificial sweats by using commercial carbon electrodes, screen-printing electrodes (SPEs), and SPE-SLCEs. It found that no matter which kind of electrodes, the inner resistance of artificial with pH value of 4 is the lowest. It is assumed that the free H^+ contributes to the immigration of cations to decrease the inner resistance. The inner resistance of artificial with pH values of 5, 7, and 8 were closed to each other. In the real human sweat (Figure 6.2), the pH value was in the range of 4-5, but the inner resistance is near to the artificial sweat with pH value of 7 (Figure 6.3a), because the similar ionic concentration. In subsequent studies, we should avoid using PBS solutions for quantification.

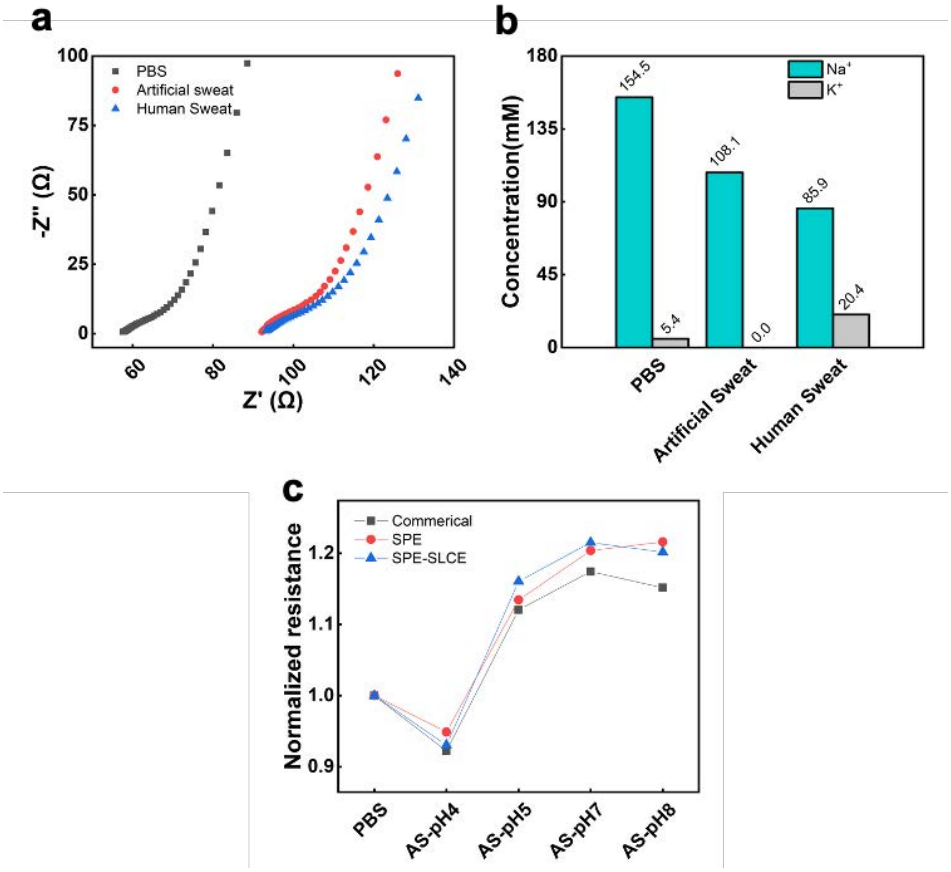

Figure 6.3 Difference of internal resistance of PBS, artificial sweat, and human sweat(a) EIS of PBS, artificial sweat, and human sweat on sponge-like carbon electrodes; (b) concentration of Na^+ and K^+ in PBS, artificial sweat, and human sweat; (c) normalized resistance of different artificial sweat.

6.3.3 Liquid Metal-based Glucose Sensors

Glucose sensing is achieved using chronoamperometry, where different voltages are applied to the glucose sensors and the corresponding response currents are measured. In this study, the researchers explored the linear relationship between the response currents and the potential values for glucose solutions with concentrations ranging from 0 to 640 μM (Figure 6.4).

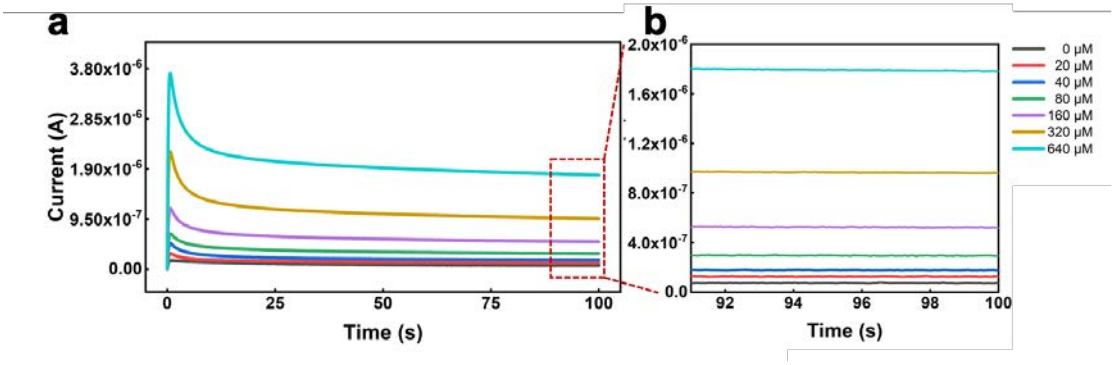

Figure 6.4 Analysis of glucose via chronoamperometry. (a) the whole and (b) parts of 90 s to 100 s process of chronoamperometry.

The principle of glucose sensors glucose was to use dehydrogenase (GDH) as the catalyst, hexammine ruthenium(III) chloride ($[Ru(NH_3)_6]Cl$) and phenazine ethosulfate (PES) as electron mediators.[226] PES can combine with the coenzyme factor (NADH) of GDH to transfer electrons, allowing quasi-diffusion-controlled electron transfer (2.5 generation quasi-DET)[132, 227] from the enzyme to the mediator. PES was chosen as the ideal mediator due to its low redox potential, which enables electrochemical detection at low operating potentials and reduces interference.[132, 228] The reaction can be described as chemical formulas 6.1 and 6.2.

$$Glucose + Ru(NH_3)_6{}^{3+} + + GDH \rightarrow Glucono\ Lactone + Ru(NH_3)_6{}^{2+} \quad (6.1)$$

$$Ru(NH_3)_6{}^{2+} \rightarrow Ru(NH_3)_6{}^{3+} + e - \quad (6.2)$$

To establish a standard curve, the researchers chose four potentials (0.10, 0.15, 0.20, and 0.25 V) assuming complete electron transport at these potentials. Figure 6.5 in the study showed that the responding current at 0.1 V was relatively lower than the others, making it difficult to distinguish from background signals. The Pearson's R values for 0.15 V, 0.20 V, and 0.25 V were similar, with values of 0.976, 0.979, and 0.980, respectively. Considering the resolution of the glucose sensor and the slope of the fitting line, the researchers chose 0.2 V as the standard potential for their analysis.

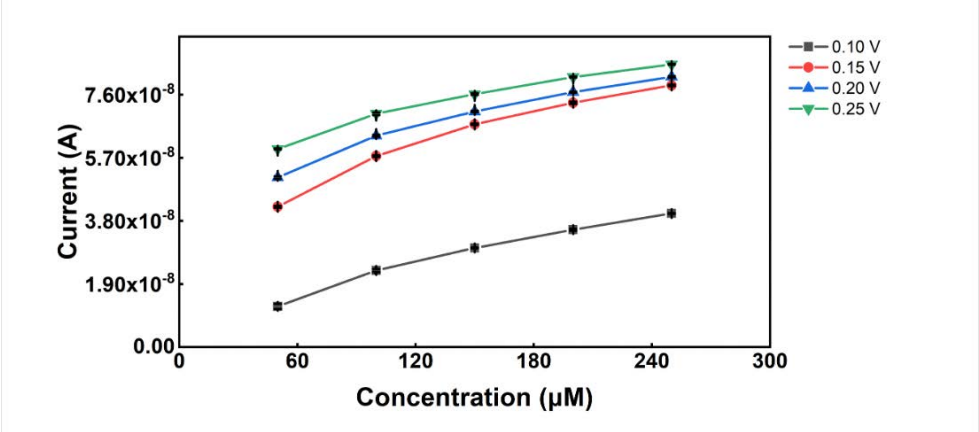

Figure 6.5 Establishment of standard curve of glucose sensors under different potential.

The chronoamperometry method was employed to establish the correlation between the concentration of glucose and the resulting response current in glucose sensors. This analysis was conducted at a potential of 0.2 V, utilizing PBS solution, artificial sweat, and human sweat as the electrolytes. Standard curves of glucose solutions were generated in different systems, including PBS, artificial sweat, and human sweat, with corresponding R-squares of 0.998, 0.999, and 0.999, respectively. This indicates that the glucose sensor can establish a specific range standard curve for glucose quantification under various electrolyte systems (Figure 6.6a-c). By comparing the linear curves, it was observed that the curves established in different systems exhibited distinct slopes and intercepts (Figure 6.6d). This finding demonstrates that the direct measurement of the current response of sensors cannot directly determine the glucose concentration in real sweat. However, through the process of normalization, it was observed that the normalized curves significantly overlapped, indicating a correlation

between the results obtained by the glucose sensors in different electrolyte systems (Figure 6.6e). The normalization was followed the formula 6.3,

$$I_N = \frac{\Delta\,(I_i - I_s)}{\Delta\,(I_e - I_s)} \qquad (6.3)$$

in which I_i means the testing current, I_o means the current of the starting concentration of the concentration range, I_e means the current of the ending concentration of the concentration range. Similarly, we can eliminate the differences between different sensors through normalization processing (Figure 6.6f)

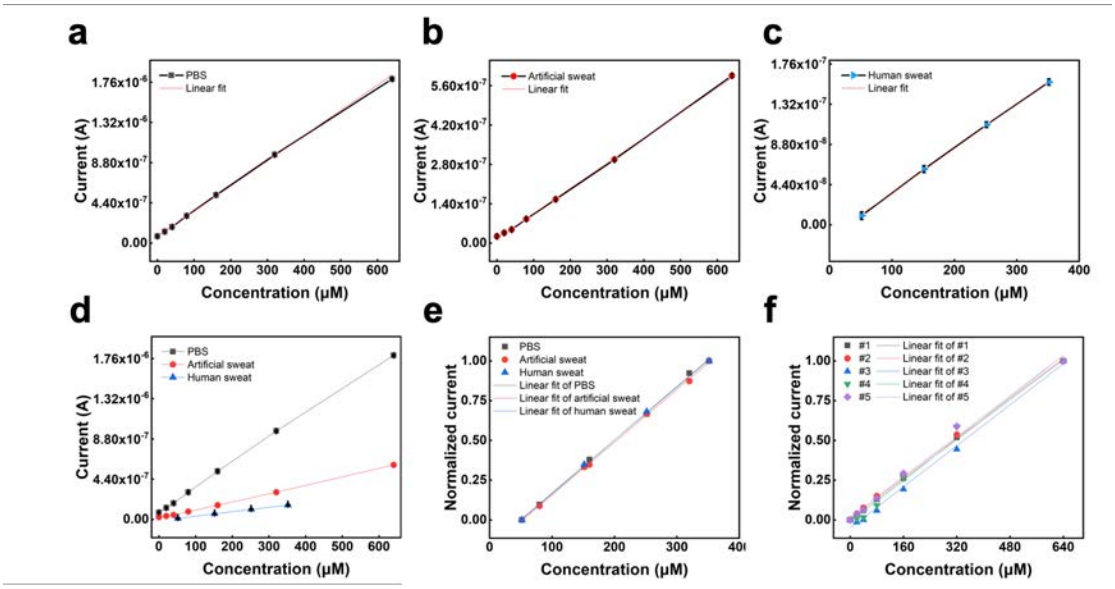

Figure 6.6 Standard curves of glucose sensors via chronoamperometry. Standard curves of different concentration of glucose solved in PBS (a), artificial sweat (b), and human sweat (c); (d) comparison of standard curves of glucose sensors in PBS, artificial sweat, human sweat; (e) normalization of standard curves of glucose sensors in PBS, artificial sweat, human sweat; (f) the reproducibility of the glucose sensors.

Nonetheless, the normalized calibration method presents certain challenges in the context of sweat systems. This method requires obtaining two electrochemical signals with well-known concentrations within the same system and subsequently estimating the concentration value of a third point. However, accomplishing this within the context

of sweat systems is inherently troublesome. While human skin is a delicate organ, its metabolic processes are expected to adhere to relatively stable patterns. However, sweat composition can be easily influenced by changes in dietary structure. Considering these challenges, we propose the inclusion of an external working electrode devoid of specific active substances. The intention behind this addition is to counterbalance the electrochemical response triggered by impurities present in sweat.

According to the Nernst-Planck Equation,

$$J_i(x) = -D_i \Delta C_i(x) - \frac{Z_i F}{RT} D_i C_i(x) \Delta\varphi(x) + C_i(x) v(x) \qquad (6.4)$$

where $J_i(x)$ is flux in (mol·s^{-1}·cm^2), D_i is the diffusion coefficient, $\Delta C_i(x)$ is the gradient of concentration of the material i on the x location, $\Delta\varphi(x)$ is the gradient of the electric field, Z_i is the ion charge of the material i, F is the Faraday constant in 9.6485332 ×10^4 C·mol^{-1}, T is temperature in kelvin is 298 K, R is the universal gas constant in 8.314 J·K^{-1}·mol^{-1}. Considering the electrolyte is static, the convection current part, $C_i(x)v(x)$, is equal to 0.

For linear ions transfer, the formula 6.4 can transform to:

$$J_{\mathrm{i}}(x) = -D_{\mathrm{i}} \left[\frac{C_{\mathrm{i}}(x)}{x}\right] - \frac{Z_{\mathrm{i}} F}{RT} D_{\mathrm{i}} C_{\mathrm{i}}(x) \left[\frac{\varphi(x)}{x}\right] \qquad (6.5)$$

If the material i is with charge, the flux $J_{\mathrm{i}}(x)$ is equal to the current density of the material i, the formula 6.5 is equal to:

$$J_{\mathrm{i}}(x) = \frac{I_{\mathrm{i}}}{Z_{\mathrm{i}} FA} = \frac{I_{d,\mathrm{i}}}{Z_{\mathrm{i}} FA} + \frac{I_{m,\mathrm{i}}}{Z_{\mathrm{i}} FA} \qquad (6.6)$$

where I_{i} is the current generating by the material i, $I_{d,\mathrm{i}}$ is the diffusing current and the $I_{m,\mathrm{i}}$ is the migration current of the material i.

During electrolysis, the current I is the sum of all materials:

$$I = \sum_{\mathrm{i}} I_{\mathrm{i}} \qquad (6.7)$$

According to the Einstein-Smoluchowski equation:

$$u_{\mathrm{i}} = \frac{|Z_{\mathrm{i}}|FD_{\mathrm{i}}}{RT} \qquad (6.8)$$

where the u_i is the mobility of the material i, thus the

$$I_{\mathrm{i}} = |Z_{\mathrm{i}}|FAu_{\mathrm{i}}\, C_{\mathrm{i}}(x)\frac{\varphi(x)}{x} \qquad (6.9)$$

For the linear electric field, the formula 6.9 is equal to

$$I_{\mathrm{i}} = |Z_{\mathrm{i}}|FAu_{\mathrm{i}}\, C_{\mathrm{i}}(x)\frac{\Delta E}{l} \qquad (6.10)$$

where the $\frac{\Delta E}{l}$ is the gradient of the electric field caused by the potential change in the distance l.

Combining the formula 6.7 and 6.10, we could obtain:

$$I = \frac{FA\Delta E}{l}\sum_{\mathrm{i}} |Z_{\mathrm{i}}|Fu_{\mathrm{i}}\, C_{\mathrm{i}}(x) \qquad (6.11)$$

The conductivity κ (Ω^{-1}) of the solution can be described as:

$$\kappa = F\sum_{\mathrm{i}} |Z_{\mathrm{i}}|u_{\mathrm{i}}\, C_{\mathrm{i}}(x) \qquad (6.12)$$

If there are few electroactive materials, the current I:

$$\frac{I}{FA} = -\sum_{k=1}^{q} n_k J_k(0,t) = -\sum_{k=1}^{q} n_k D_k \left[\frac{C_k(x,t)}{x}\right]_{x=0} \qquad (6.13)$$

The electrochemically active materials in sweat would contribute to migration current. In the same electrolyte system, we assume that the concentration of the electrochemically active impurities is stable. Consequently, the $I_{\text{impurities}}$ is stable. By

introducing another working electrode without enzyme, the total I_2 in this second working electrode is the sum of diffusing current and migration current without the target molecules. Thus, the calculating process can be taken as:

$$\frac{I_1}{FA} = -(n_{glucose}J_{glucose}(0,t) + \sum_{k=2}^{q} n_k J_k(0,t)) \qquad (6.14)$$

$$\frac{I_2}{FA} = -\sum_{k=2}^{q} n_k J_k(0,t) \qquad (6.15)$$

$$\Delta I = I_1 - I_2 = FAn_{glucose}J_{glucose}(0,t) = KC_{glucose}(x) \quad (6.16)$$

I_1 is the total current recorded by chronoamperometry on the electrode 1 with enzymes. I_2 is the total current recorded by chronoamperometry on the electrode 2 without enzymes. Here, according to 6.10 and 6.16, K is the constant relative to the conductivity of the electrolyte.

According to the formula above, we used ΔI to establish the linear relationship of the standard curve of artificial sweat and put the $\Delta I_{\text{sample i}}$ to calculate the concentration (fitting). The concentration (CA) was calculated by putting the I_1 from electrode 1 in the standard curve from artificial sweat. Concentration (fitting) had a lower variance than directly calculating concentration using a standard curve (Table 6.1).

Table 6.1 Comparison of concentration of glucose before/after fitting

	Concentration (Assay Kit)	Concentration (CA)	Δ (μM)	Concentration (Fitting)	Δ(μM)
Sample 1	44.72	123.93	79.21	20.57	24.15
Sample 2	13.7	63.27	46.57	30.35	13.65
Sample 3	29.08	67.76	61.86	28.85	0.23
Sample 4	44.02	48.15	4.13	25.82	18.19
Sample 5	52.26	58.55	6.29	27.43	24.82

Sample 6	91.40	84.01	7.39	91.92	0.52

6.3.4 Liquid Metal-based Lactate Sensors

The lactate sensors utilized in this study operate within a concentration range of 0-50 mM, focusing on analyzing the linear relationship between the concentration and response currents. Chronoamperometry method was conducted to analyze lactate (Figure 6.7). This investigation contributes to the development of a comprehensive sensing system for monitoring lactate concentrations, which can have significant implications in various applications such as exercise physiology, medical diagnostics, and sports performance optimization.

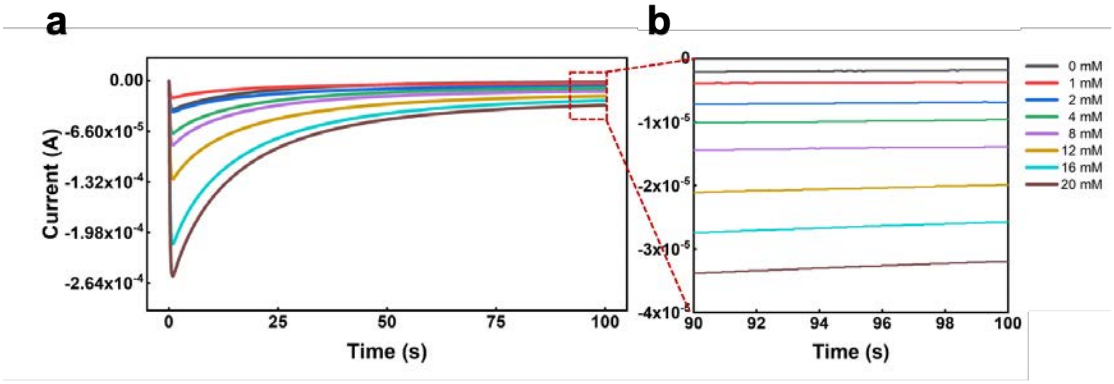

Figure 6.7 Analysis of lactate via chronoamperometry; (a) the whole and (b) parts of 90 s to 100 s process of chronoamperometry.

According to its low redox potential, we chose five potentials, -0.05, -0.085, -0.1, -0.125 and -0.150 V, to establish standard curve, for assuming the electron transporting completely at such potentials (Figure 6.8).

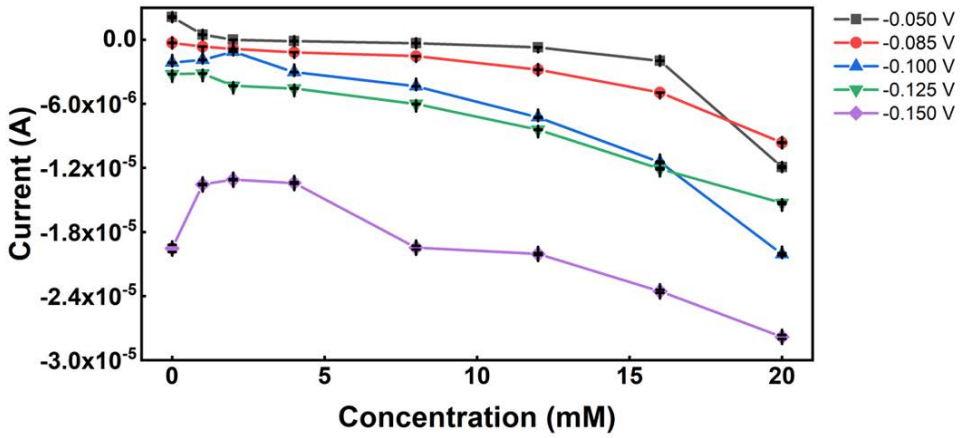

Figure 6.8 Establishment of standard curve of lactate sensors under different potentials.

Due to the high lactate content in real sweat, it is difficult to establish a standard curve for lactate detection in real human sweat by adding lactic acid. Thus, we used the chronoamperometry method (potential was -0.125 V) to establish the relationship between the lactic acid concentration and the reaction current of the lactic acid sensor in PBS solution and artificial sweat. Similarly, when we compared the standard curves of lactate in PBS and artificial sweat, we can see that the slope of the standard curve in artificial sweat is smaller (Figure 6.9a-c). The current response measured in actual sweat was also smaller than that in artificial sweat. Through normalization, sensors in different solution systems can obtain similar current response and concentration curves (Figure 6.9d). We tested five different electrodes. Through normalization processing, part of the error can be eliminated, and the same sample can be measured by different electrodes (Figure 6.9e).

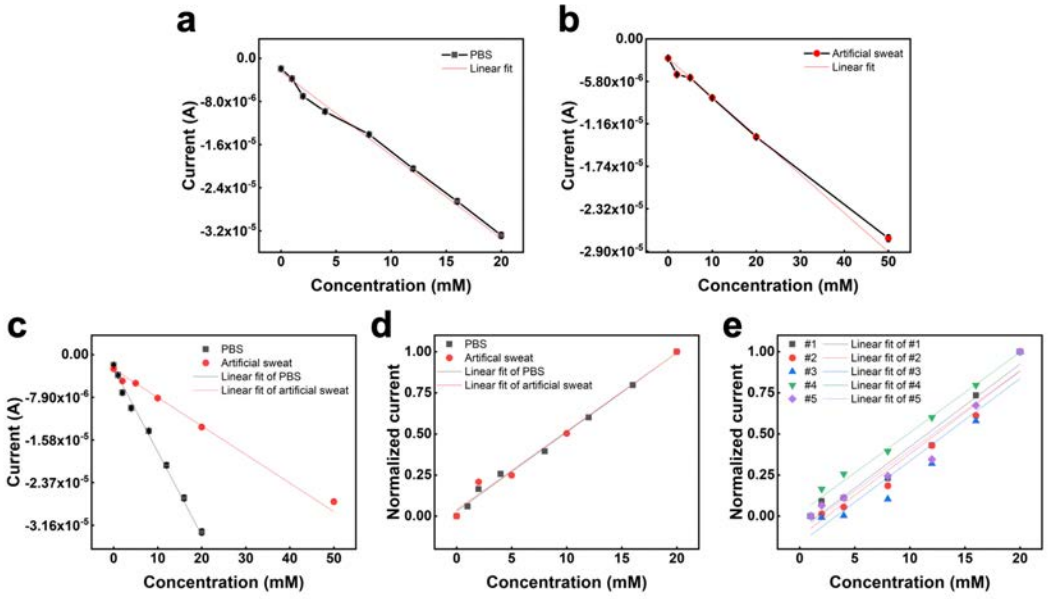

Figure 6.9 Standard curves of different concentration of lactate in PBS (a) and artificial sweat (b); (c) comparison of standard curves of glucose sensors in PBS, artificial sweat, (d) normalized standard curves; (e) the reproducibility of the lactate sensors.

Based on the aforementioned formula, we employed the change in current (ΔI) to establish a linear correlation in the standard curve. Subsequently, we obtained the ΔI value for each sample (labeled as $\Delta I_{\text{sample i}}$ and utilized it to determine the concentration via a fitting process. Notably, the variance in concentration (fitting) exhibited lower levels when compared to the direct calculation of concentration using the standard curve, as indicated in Table 6.2.

Table 6.2 Comparison of concentration of lactate before/after fitting

	Concentration (Assay Kit)	Concentration (CA)	Δ(mM)	Concentration (Fitting)	Δ (mM)
Sample 1	42.59	46.08	3.49	43.61	1.02
Sample 2	20.13	34.14	14.01	25.87	5.74
Sample 3	6.71	9.02	2.31	4.19	2.52

Sample 4	4.05	17.37	13.32	13.51	9.46
Sample 5	35.22	25.83	9.39	25.31	9.91
Sample 6	26.97	23.63	3.35	22.61	4.37

6.3.5 Liquid Metal-based Ionic Sensors

The methodology employed in the Na^+ and K^+ sensors relies on the measurement of the open circuit potential, which is altered by the ion-selective permeability membrane. To establish a standard curve, we dissolved NaCl or KCl directly in deionized water.

The magnitude of the open circuit potential is influenced by the concentration of ions, generally escalating as the ion concentration increases. Here, we characterized the performance of the Na^+ sensors. The OCP of Na^+ sensor was recorded against time. When the concentration of Na^+ increased, the OCP increased as well (refer to Figure 6.9a). The linear fit of the standard curve exhibited 0.999 value of the R-square, which meant in the range of 8 - 256 mM of Na^+, the logarithm of the concentration had a linear relationship with the OCP value (Figure 6.10b). The repeatability of 5 samples of Na^+ sensors has been shown in Figure 6.10c.

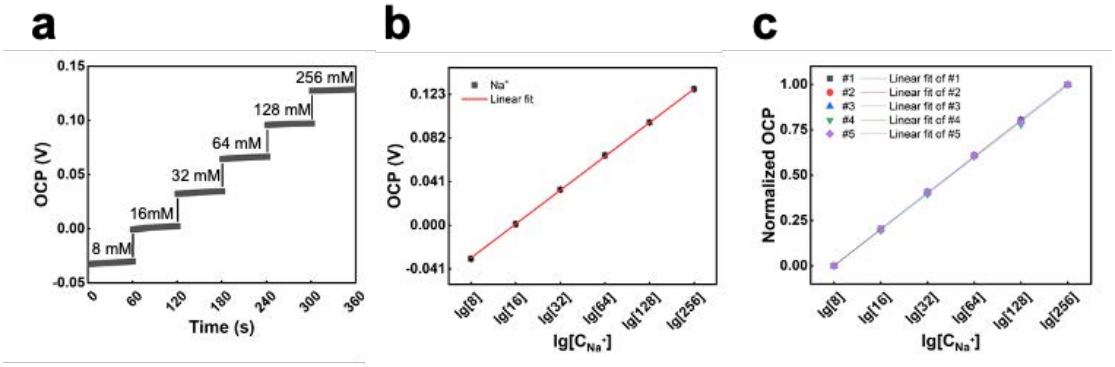

Figure 6.10 Standard curves of Na^+ sensors; (a) the OCP response of the Na^+ sensor against the concentration of Na^+; (b) the linear fit of the Na^+ sensor against the logarithm of the concentration; (c) the repeatability of the Na^+ sensors.

Since the circuit lacks any current flow in this scenario, impurities present in sweat have minimal electrochemical response, thus exerting negligible impact on ion detection. By incorporating the measured open circuit potential from actual sweat into the standard curve, we compared the calculated ion concentrations with those determined using ICP-MS technology. We assumed that the ICP-MS value was the real concentration of ions in the sweat. It is observed that the assessments exhibited similar trends (Figure 6.11a). Subsequently, we adjusted the calculation outcomes by multiplying them with a coefficient, ensuring a closer correspondence to the real concentration (as shown in Figure 6.11b). The coefficient was applied to fit the results being monitored *in situ*.

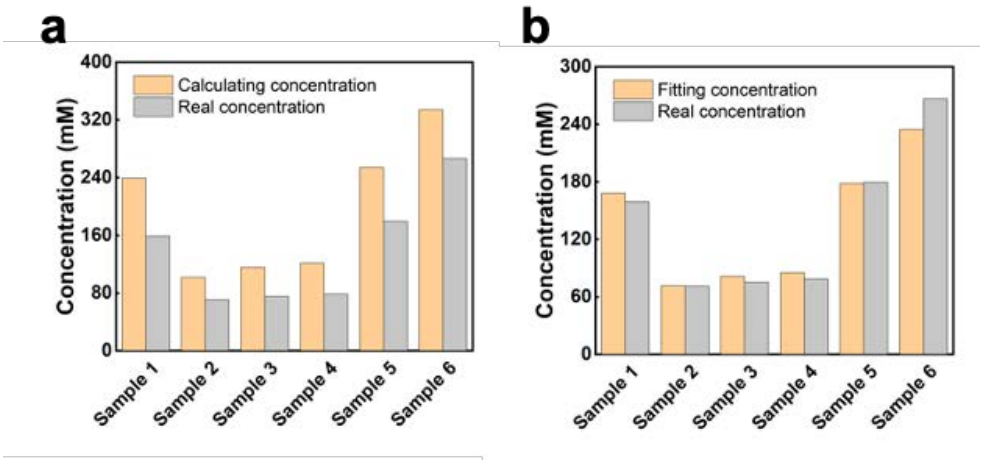

Figure 6.11 Analysis of Na^+ in human sweat; (a) comparison of calculating and real concentration of Na^+ in sweat; (b) comparison of fitting and real concentration of Na^+ in sweat.

Moreover, the performance of the K^+ sensors was assessed. The OCP of the K^+ sensor was measured over a period of time. It was observed that as the concentration of K^+ increased, the OCP also exhibited an upward trend (refer to Figure 6.12a). The standard curve generated through linear regression analysis displayed an R-square value of 0.990, indicating a linear relationship between the logarithm of K^+ concentration and the corresponding OCP value within the range of 2-64 mM (Figure 6.12b). The repeatability of the K^+ sensors was investigated using 5 samples, and the results are depicted in Figure 6.12c.

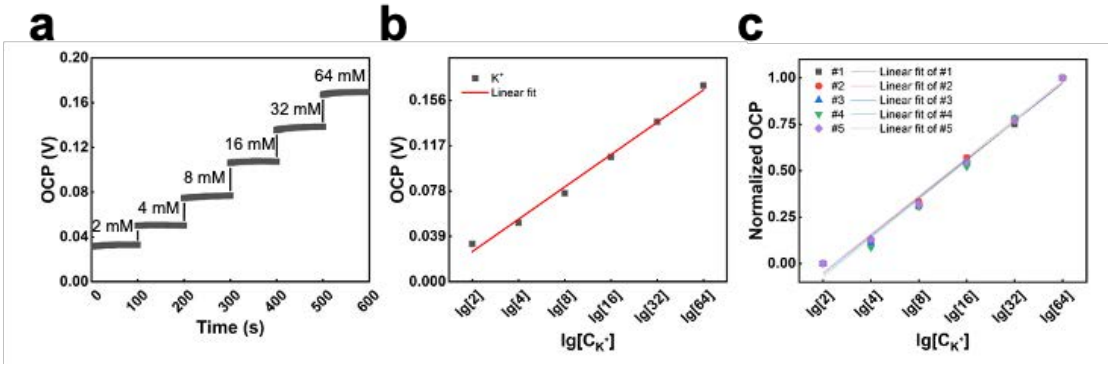

Figure 6.12 Standard curves of K^+ sensors; (a) the OCP response of the K^+ sensor against the concentration of K^+; (b) the linear fit of the K^+ sensor against the logarithm of the concentration; (c) the repeatability of the K^+ sensors.

Similarly, we obtained the calculated concentration of K^+ according to the standard curve of the K^+ sensors (Figure 6.13). To improve the accuracy of the calculation outcomes, a coefficient was introduced and applied to adjust the results, thereby establishing a better correspondence with the actual concentration (Figure 6.13b). This coefficient was incorporated to align the monitored results in situ as well.

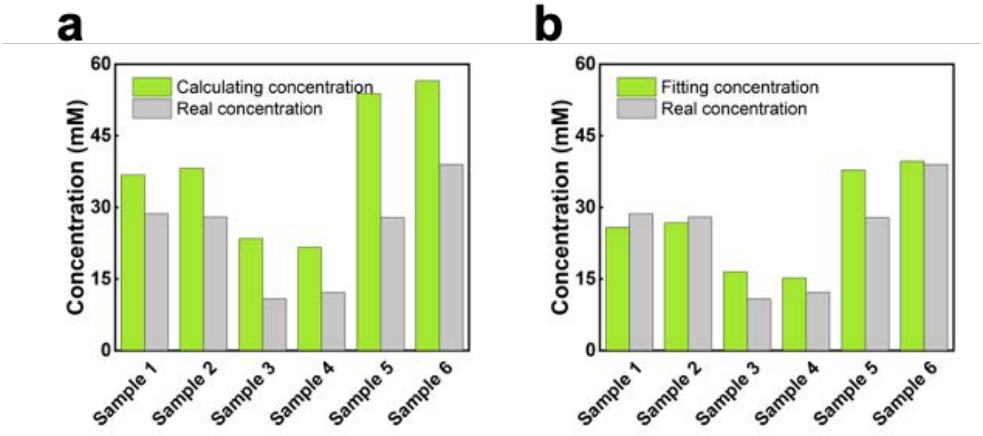

Figure 6.13 Analysis of K^+ in human sweat; (a) comparison of calculating and real concentration of K^+ in sweat; (b) comparison of fitting and real concentration of K^+ in sweat

6.3.6 Sweat Monitoring

To realize the in situ sweat sensing, the portable electrochemical workstation (commercial module was from PlamSens) was applied (Figure 6.14). To directly output the signals, the CH340g module as serial converter was connected to the electrochemical workstation module with the computer. The OCP and the CA were conducted via this module.

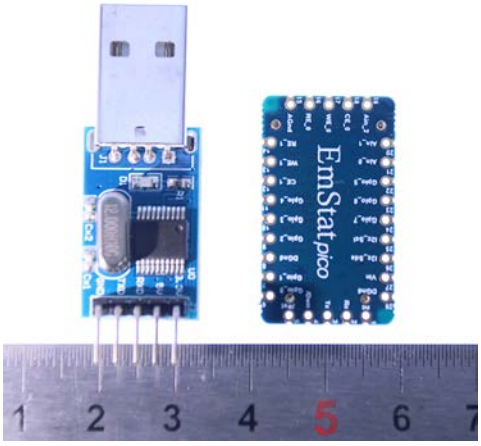

Figure 6.14 The portable electrochemical workstation for *in situ* sweat sensing. The right one is the EmStat pico module from PalmSens; the left one is the CH340g module for the serial converter.

Upon completion of sensor preparation, the electrodes were affixed onto the surface of the human skin following thorough cleansing with clean water. To ensure reliable data, volunteers were instructed to remain relatively still during the testing procedure to minimize potential instabilities at the sensor-skin interface. Initially, the responses of glucose, lactic acid, Na^+, and K^+ in sweat were collected at 0 minutes during exercise. Subsequently, the volunteers consumed a can of Coke and 50 g of chocolate, and sweat response signals were recorded at 10 minutes, 20 minutes, and 30 minutes thereafter (Figure 6.15). We calculated and fitted the output concentration of the sweat sensors. In Table 6.3, we showed the concentration of glucose, lactate, K^+, and Na^+ in sweat at every 10 minutes. concentrations the The results demonstrated that ten minutes after

food consumption, there was an increase in glucose, lactate, and Na^+ concentrations, while the levels of K^+ remained relatively stable (Figure 6.15). After twenty minutes, there was a slight rise in glucose concentration, a minor decrease in lactic acid concentration (still higher than the initial levels), a slight decline in sodium ion concentration, and a significant decrease in potassium ion concentration. At this point, the volunteers were provided with additional drinking water to prevent dehydration. Subsequent testing ten minutes after water replenishment, i.e., 30 minutes after food intake, revealed significant drops in glucose, lactic acid, and Na^+ concentrations, while the K^+ values did not display significant changes.

Table 6.3 Concentration of glucose, lactate, K^+, and Na^+ in sweat at every 10 minutes.

	0 min	**10 min**	**20 min**	**30 min**
Glucose (μM)	115.2	226.4	256.3	73.76
Lactate (mM)	3.1	12.9	10.8	0.4
Na^+ (mM)	20.3	34.9	19.8	8.5
K^+ (mM)	4.8	4.2	1.7	1.8

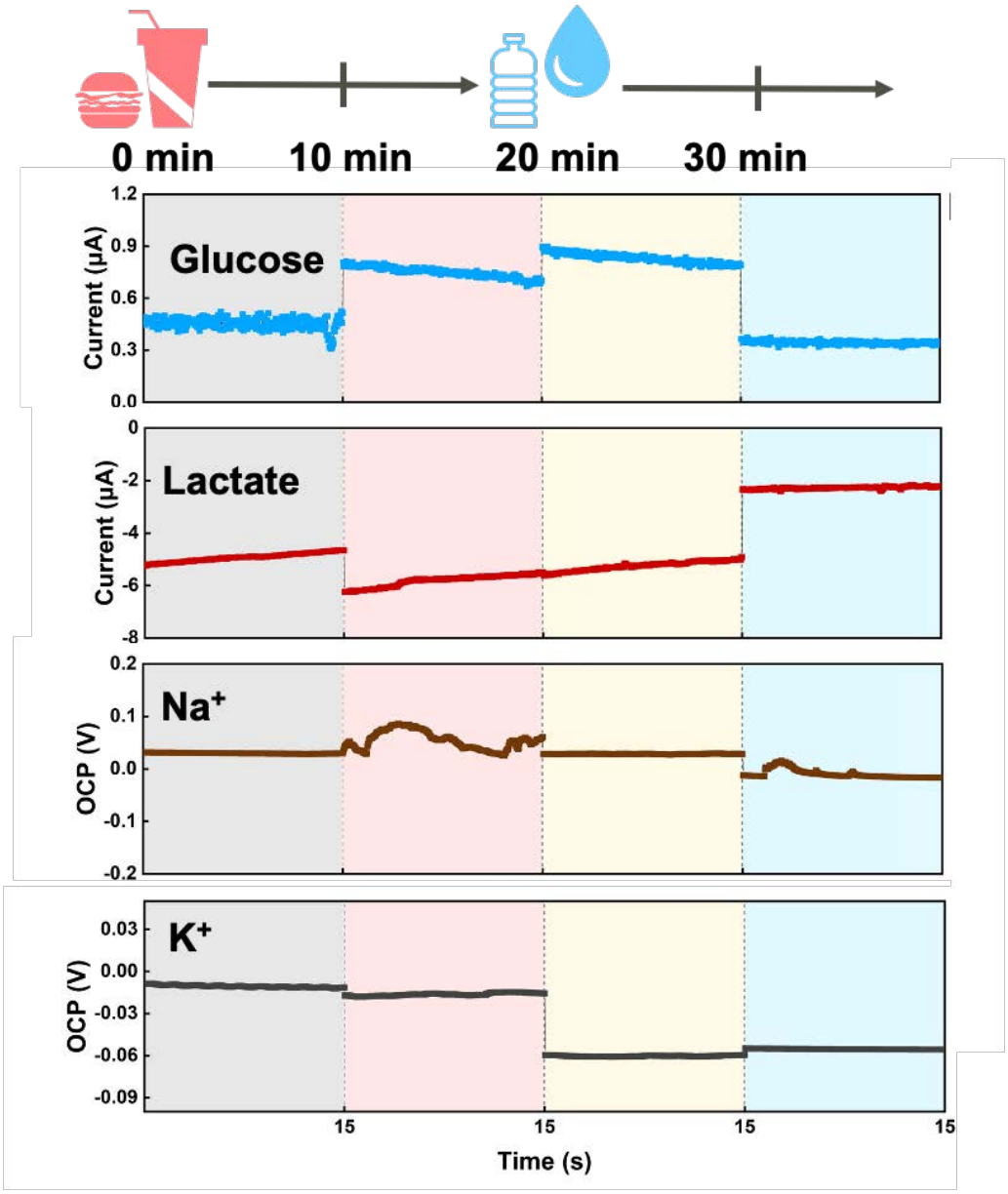

Figure 6.15 the *in situ* sweat monitoring before and after having food and water.

6.4 Conclusions

In this chapter, we use screen printing technology to prepare a liquid metal-based sweat sensor for analyzing the concentrations of glucose, lactate, potassium, and sodium in sweat.

We built a profile of sweat that showed the pH of sweat to be acidic, with a mean of 4.75 and a median of 4.44. The maximum pH value observed is 5.72, lactic acid concentration is in the range of 4-82 mM, glucose concentration in sweat is in the range of 16-200 μM, sodium ion concentration is the highest at 52-266 mM, and potassium ion concentration is lower at 10-39 mM, the calcium ion concentration is 80-453 μM, the magnesium ion concentration is relatively dispersed, with large individual differences, between 76-569 μM, and no iron ions are detected in sweat samples. The impedance values of artificial sweat and real sweat are relatively close, but artificial sweat does not contain potassium ions. Sweat contains electrochemically active substances that are not found in artificial sweat, which will affect the accuracy of electrochemical detection results to a certain extent.

We introduced a second working electrode without active material into the detection system to offset the impact of impurities in sweat on the sensor. The results show that the theoretical concentration value calculated after offset has a similar trend to the real value. The deviation value in glucose sensing is within 25 μM, and the deviation value in lactate sensing is within 10mM. For ion sensors, the electrochemical substance acts very little when measuring the open circuit potential, so the test results themselves have a similar trend to the true value. A coefficient correction can make the fitting result closer to the true value. We applied such liquid metal-based sweat sensors to record and analyze glucose, lactate, sodium, and potassium change of the subject during exercise.

Chapter 7 Conclusions and Suggestions for Future Research

7.1 Conclusions

The primary objective of this research is to explore cost-effective and simple methods for the development of wearable devices using liquid metal. The aim is to resolve compatibility challenges between new liquid metal materials and traditional electronic materials. Additionally, this study aims to harness the bioenergy present in sweat through the utilization of liquid metal equipment, enabling both power supply and sweat analysis. The successful creation of such devices has the potential to advance flexible electronics and provide valuable support for future smart medical care, addressing the issue of limited medical resources.

In Chapter 4, we propose a straightforward approach to fabricate wearable biofuel cells using the screen-printing technique. These biofuel cells are constructed by screen-printing highly conductive metal-polymer composites (MPCs) onto a flexible PDMS substrate. The MPCs possess exceptional electrical conductivity (2.7×10^5 $S\cdot m^{-1}$), ensuring optimal performance of the biofuel cells. Moreover, their remarkable biocompatibility and stretchability (with a strain exceeding 200%) allow the bio-interface to conform effectively to human skin. We successfully employed these biofuel cells to power various wearable sensors, including temperature, oximeter, and heart rate sensors, for monitoring individuals' physical parameters during exercise. In the future, these biofuel cells can be further integrated into even more stretchable wearable electronic devices, such as electronic tattoos, epicardial pacing wires, and displays. This integration would enable them to serve as sustainable and eco-friendly power sources.

In Chapter 5, to summarize, we have successfully developed a stretchable and breathable electrospun mat as a substrate material (with a breathability rate of 13.3 $g\cdot m^{-2}\cdot h^{-1}$ in 45% humidity and 5.42 $g\cdot m^{-2}\cdot h^{-1}$ in 60% humidity) through the electrospinning technique. Additionally, using an etching method, we fabricated sponge-like carbon

electrodes that possess low electrical resistance (6 Ω·mm), high specific surface area, and a certain level of stretchability (with a tensile strain of 35%). Combining these two materials, we have constructed sweat biofuel cells with breathable properties. These biofuel cells have demonstrated a maximum power density of 219 $\mu W \cdot cm^{-3}$ at a voltage of 0.123V. To harness their potential, we have utilized these sweat fuel cells to power strain sensors capable of detecting deformation through changes in current (0.445 ± 0.09 μA for 100% strain). By directly connecting the biofuel cell and the strain sensor in series, with the sensor component attached to the finger joint for detecting finger bending, we can record the current and potentially integrate this application with neural networks and machine learning algorithms for advanced gesture recognition based on variations in current values.

In Chapter 6, our study focuses on the development of a liquid metal-based sweat sensor using screen printing technology. This sensor is designed to analyze the concentrations of glucose, lactate, potassium, and sodium in sweat. In our investigation, we established a comprehensive sweat profile, revealing its characteristic acidic nature, the concentration of lactic acid in sweat ranged between 4-82 mM, while the concentration of glucose ranged from 16 to 200 μM, Na^+ was from 52 to 266 mM, followed by K^+ was from 10 to 39 mM, Ca^{2+} was within the range of 80 to 453 μM, Ma^{2+} exhibited ranging from 76 to 569 μM. To mitigate the effects of impurities in sweat on the sensor, we introduced a second working electrode without any active material into the detection system. Our results demonstrated that after accounting for this offset, the theoretically calculated concentration values exhibited a similar trend to the actual values. The deviation in glucose sensing was within 25 μM, and for lactate sensing, it was within 10 mM. In the case of ion sensors, the electrochemical substances had minimal influence on the measurement of open circuit potential, resulting in test results that closely resembled the true values. However, employing a coefficient correction method helped improve the fitting results, bringing them closer to the true values.

7.2 Suggestions for Future Research

1. The issue of stability remains a significant challenge in current liquid metal devices. Chapter 5 investigates the use of a porous structure in spin membrane substrates to create air-permeable fuel cells. However, the porosity of the spun film substrate hinders the effective encapsulation of liquid metal wires. The thickness of the encapsulation layer poses a dilemma, as excessively thick layers inhibit device and skin conformability, while excessively thin layers hinder effective encapsulation. Additionally, the integration of flexible liquid metal devices with rigid FPCB devices presents a soft-hard combination challenge. This necessitates combining other technologies to enable inherent flexibility in electronic device modules and improving physical structures to render hard circuits more flexible.

2. The current power density of liquid metal-based sweat biofuel cells remains relatively low. Our current approach involves collecting energy into a capacitor via a booster, subsequently charging other electronic devices, or directly supplying power to a resistor for monitoring weak currents as described in Chapter 6. To enhance the utility of sweat biofuel cells in future applications, two approaches can be employed. Firstly, improving the catalytic efficiency of the device can enhance power density. Secondly, developing applications with lower energy consumption can optimize the usefulness of these biofuel cells.

3. The calibration method we employ for sweat analysis has a limited range of applicability. To expand its potential, future research can include calibration with a broader range of samples to further refine the model. Additionally, other components within sweat bear monitoring significance but have not been extensively studied. It remains unclear how our calibration method can be applied to the monitoring of other biomolecules. The exploration of these areas represents future avenues for research in the field of sweat analysis.

REFERENCES

1. Luo, Y.; Abidian, M. R.; Ahn, J.-H.*, et al.*, Technology roadmap for flexible sensors. *ACS Nano* **2023,** *17* (6), 5211-5295.
2. Yin, R. T.; Chen, S. W.; Benjamin Lee, K.*, et al.*, Open thoracic surgical implantation of cardiac pacemakers in rats. *Nature Protocol* **2023,** *18* (2), 374-395.
3. Lin, S.; Cheng, X.; Zhu, J.*, et al.*, Wearable microneedle-based electrochemical aptamer biosensing for precision dosing of drugs with narrow therapeutic windows. *Science Advances* **2022,** *8* (38), eabq4539.
4. Bandodkar, A. J.; Wang, J., Non-invasive wearable electrochemical sensors: A review. *Trends in Biotechnology* **2014,** *32* (7), 363-371.
5. Xu, S.; Kim, J.; Walter, J. R.*, et al.*, Translational gaps and opportunities for medical wearables in digital health. *Science Translational Medicine* **2022,** *14* (666), eabn6036.
6. Jung, Y. H.; Yoo, J.-Y.; Vázquez-Guardado, A.*, et al.*, A wireless haptic interface for programmable patterns of touch across large areas of the skin. *Nature Electronics* **2022,** *5* (6), 374-385.
7. Koydemir, H. C.; Ozcan, A., Wearable and implantable sensors for biomedical applications. *Annual Review of Analytical Chemistry* **2018,** *11* (1), 127-146.
8. Kenry; Yeo, J. C.; Lim, C. T., Emerging flexible and wearable physical sensing platforms for healthcare and biomedical applications. *Microsystems & Nanoengineering* **2016,** *2* (1), 16043.
9. Naganur, V.; Sivathamboo, S.; Chen, Z.*, et al.*, Automated seizure detection with noninvasive wearable devices: A systematic review and meta-analysis. *Epilepsia* **2022,** *63* (8), 1930-1941.
10. Liu, Y.; Pharr, M.; Salvatore, G. A., Lab-on-skin: A review of flexible and stretchable electronics for wearable health monitoring. *ACS Nano* **2017,** *11* (10), 9614-9635.
11. Sun, Q.-J.; Lai, Q.-T.; Tang, Z.*, et al.*, Advanced functional composite materials toward e-skin for health monitoring and artificial intelligence. *Advanced Materials Technologies* **2023,** *8* (5), 2201088.
12. Tang, L.; Mou, L.; Zhang, W.*, et al.*, Large-scale fabrication of highly elastic conductors on a broad range of surfaces. *ACS Appl Mater Interfaces* **2019,** *11* (7), 7138-7147.

13. Tian, X.; Lee, P. M.; Tan, Y. J.*, et al.*, Wireless body sensor networks based on metamaterial textiles. *Nature Electronics* **2019,** *2* (6), 243-251.
14. Yang, K.; Isaia, B.; Brown, L. J. E.*, et al.*, E-textiles for healthy ageing. *Sensors* **2019,** *19* (20), 4463.
15. Chen, G.; Xiao, X.; Zhao, X.*, et al.*, Electronic textiles for wearable point-of-care systems. *Chemical Reviews* **2022,** *122* (3), 3259-3291.
16. Zhu, Y.; Li, S.; Li, J.*, et al.*, Lab-on-a-contact lens: Recent advances and future opportunities in diagnostics and therapeutics. *Advanced Materials* **2022,** *34* (24), 2108389.
17. Yu, D.; Li, Z.; Xie, W.*, et al.*, Applications of nanogenerator-based wearable devices in orthopedics. *Nano Energy* **2022,** *103*, 107762.
18. Wang, S.; Xu, J.; Wang, W.*, et al.*, Skin electronics from scalable fabrication of an intrinsically stretchable transistor array. *Nature* **2018,** *555* (7694), 83-88.
19. Dickey, M. D., Stretchable and soft electronics using liquid metals. *Advanced materials* **2017,** *29* (27), 1606425.
20. Wang, C.; Wang, C.; Huang, Z.*, et al.*, Materials and structures toward soft electronics. *Advanced Materials* **2018,** *30* (50), 1801368.
21. Zhu, S.; So, J.-H.; Mays, R.*, et al.*, Ultrastretchable fibers with metallic conductivity using a liquid metal alloy core. *Advanced Functional Materials* **2013,** *23* (18), 2308-2314.
22. Gozen, B. A.; Tabatabai, A.; Ozdoganlar, O. B.*, et al.*, High-density soft-matter electronics with micron-scale line width. *Advanced Materials* **2014,** *26* (30), 5211-5216.
23. Fassler, A.; Majidi, C., Liquid-phase metal inclusions for a conductive polymer composite. *Advanced Materials* **2015,** *27* (11), 1928-1932.
24. Markvicka, E. J.; Bartlett, M. D.; Huang, X.*, et al.*, An autonomously electrically self-healing liquid metal–elastomer composite for robust soft-matter robotics and electronics. *Nature Materials* **2018,** *17* (7), 618-624.
25. Parida, K.; Thangavel, G.; Cai, G.*, et al.*, Extremely stretchable and self-healing conductor based on thermoplastic elastomer for all-three-dimensional printed triboelectric nanogenerator. *Nature Communications* **2019,** *10* (1), 2158.
26. Thrasher, C. J.; Farrell, Z. J.; Morris, N. J.*, et al.*, Mechanoresponsive polymerized liquid metal networks. *Advanced Materials* **2019,** *31* (40), 1903864.

27. Liang, S.; Li, Y.; Chen, Y.*, et al.*, Liquid metal sponges for mechanically durable, all-soft, electrical conductors. *Journal of Materials Chemistry C* **2017,** *5* (7), 1586-1590.
28. Varga, M.; Mehmann, A.; Marjanovic, J.*, et al.*, Adsorbed eutectic gain structures on a neoprene foam for stretchable mri coils. *Advanced Materials* **2017,** *29* (44), 1703744.
29. Yi, L.; Liu, J., Liquid metal biomaterials: A newly emerging area to tackle modern biomedical challenges. *International Materials Reviews* **2017,** *62* (7), 415-440.
30. Prokhorenko, S. V., Structure and viscosity of gallium, indium, and tin in the vicinity of the crystallization temperature. *Materials Science* **2005,** *41* (2), 271-274.
31. Magos, L.; Clarkson, T. W., Overview of the clinical toxicity of mercury. *Annals of Clinical Biochemistry* **2006,** *43* (4), 257-268.
32. Berlin, M., Mercury in dental amalgam: A risk analysis. *NeuroToxicology* **2020,** *81*, 382-386.
33. Greenwood, N. N.; Earnshaw, A., 4 - lithium, sodium, potassium, rubidium, caesium and francium. In *Chemistry of the elements (second edition)*, Greenwood, N. N.; Earnshaw, A., Eds. Butterworth-Heinemann: Oxford, 1997; pp 68-106.
34. Mi, H.; Zhong, L.; Tang, X.*, et al.*, Electroluminescent fabric woven by ultrastretchable fibers for arbitrarily controllable pattern display. *ACS Applied Materials & Interfaces* **2021,** *13* (9), 11260-11267.
35. Zhang, Q.; Liu, J., Nano liquid metal as an emerging functional material in energy management, conversion and storage. *Nano Energy* **2013,** *2* (5), 863-872.
36. Liu, J.; Yi, L., Liquid alkali alloy for chemothermal therapy of tumor. In *Liquid metal biomaterials: Principles and applications*, Springer Singapore: Singapore, 2018; pp 417-428.
37. Liu, T.; Sen, P.; Kim, C.-J., Characterization of nontoxic liquid-metal alloy galinstan for applications in microdevices. *Journal of Microelectromechanical Systems* **2011,** *21* (2), 443-450.
38. Wang, Q.; Yu, Y.; Liu, J., Preparations, characteristics and applications of the functional liquid metal materials. *Advanced Engineering Materials* **2018,** *20* (5), 1700781.
39. Wang, X.; Guo, R.; Liu, J., Liquid metal based soft robotics: Materials, designs,

and applications. *Advanced Materials Technologies* **2019,** *4* (2), 1800549.

40. Plevachuk, Y.; Sklyarchuk, V.; Shevchenko, N.*, et al.*, Electrophysical and structure-sensitive properties of liquid ga–in alloys. *International Journal of Materials Research* **2015,** *106* (1), 66-71.
41. Spells, K. E., The determination of the viscosity of liquid gallium over an extended nrange of temperature. *Proceedings of the Physical Society* **1936,** *48* (2), 299.
42. Wang, L.; Liu, J., Liquid phase 3d printing for quickly manufacturing conductive metal objects with low melting point alloy ink. *Science China Technological Sciences* **2014,** *57* (9), 1721-1728.
43. Li, G.; Wu, X.; Lee, D.-W., A galinstan-based inkjet printing system for highly stretchable electronics with self-healing capability. *Lab on a Chip* **2016,** *16* (8), 1366-1373.
44. Chang, H.; Zhang, P.; Guo, R.*, et al.*, Recoverable liquid metal paste with reversible rheological characteristic for electronics printing. *ACS Applied Materials & Interfaces* **2020,** *12* (12), 14125-14135.
45. Matsuhisa, N.; Kaltenbrunner, M.; Yokota, T.*, et al.*, Printable elastic conductors with a high conductivity for electronic textile applications. *Nature Communications* **2015,** *6* (1), 7461.
46. Zheng, Z.; Wei, S.; Yang, Y.*, et al.*, Low-temperature solidifiable liquid metal with ultrahigh thermal conductivity enabled by spontaneous phase transition for electronics' safety and long-life cooling. *Advanced Engineering Materials* **2023,** *25* (11), 2201817.
47. Hafiz, S. S.; Xavierselvan, M.; Gokalp, S.*, et al.*, Eutectic gallium–indium nanoparticles for photodynamic therapy of pancreatic cancer. *ACS Applied Nano Materials* **2022,** *5* (5), 6125-6139.
48. Li, H.; Qiao, R.; Davis, T. P.*, et al.*, Biomedical applications of liquid metal nanoparticles: A critical review. *Biosensors* **2020,** *10* (12), 196.
49. Jia, M.; Newberg, J. T., Liquid–gas interfacial chemistry of gallium–indium eutectic in the presence of oxygen and water vapor. *The Journal of Physical Chemistry C* **2019,** *123* (47), 28688-28694.
50. Ilyukhina, A. V.; Ilyukhin, A. S.; Shkolnikov, E. I., Hydrogen generation from water by means of activated aluminum. *International Journal of Hydrogen Energy* **2012,** *37* (21), 16382-16387.

51. Wang, L.; Liu, J., Electromagnetic rotation of a liquid metal sphere or pool within a solution. *Proceedings of the Royal Society A: Mathematical, Physical and Engineering Sciences* **2015,** *471* (2178), 20150177.
52. Bi, S.; Hang, C.; Qi, J.*, et al.*, Green synthesis of liquid metal-doped carbon dots for treating multidrug-resistant gram-negative bacteria. *Advanced Biology* **2023,** *7* (6), 2200297.
53. Bi, S.; Qi, J.; Zhang, W.*, et al.*, A liquid metal dressing for anti-inflammatory and anti-infection applications to treat diabetic wounds. *Chemical Communications* **2023,** *59* (54), 8420-8423.
54. Chitambar, C. R., Medical applications and toxicities of gallium compounds. *International Journal of Environmental Research and Public Health* **2010,** *7* (5), 2337-61.
55. Dunne, S. M.; Abraham, R., Dental post-operative sensitivity associated with a gallium-based restorative material. *British Dental Journal* **2000,** *189* (6), 310-313.
56. Yi, L.; Jin, C.; Wang, L.*, et al.*, Liquid-solid phase transition alloy as reversible and rapid molding bone cement. *Biomaterials* **2014,** *35* (37), 9789-9801.
57. Tang, L.; Cheng, S.; Zhang, L.*, et al.*, Printable metal-polymer conductors for highly stretchable bio-devices. *iScience* **2018,** *4*, 302-311.
58. Tang, L.; Mou, L.; Shang, J.*, et al.*, Metal-hygroscopic polymer conductors that can secrete solders for connections in stretchable devices. *Materials Horizons* **2020,** *7* (4), 1186-1194.
59. Zhuang, Q.; Ma, Z.; Gao, Y.*, et al.*, Liquid–metal-superlyophilic and conductivity–strain-enhancing scaffold for permeable superelastic conductors. *Advanced Functional Materials* **2021,** *31* (47), 2105587.
60. Ma, Z.; Huang, Q.; Xu, Q.*, et al.*, Permeable superelastic liquid-metal fibre mat enables biocompatible and monolithic stretchable electronics. *Nature Materials* **2021,** *20* (6), 859-868.
61. Ding, L.; Hang, C.; Yang, S.*, et al.*, In situ deposition of skin-adhesive liquid metal particles with robust wear resistance for epidermal electronics. *Nano Letters* **2022,** *22* (11), 4482-4490.
62. Ren, N.; Hang, C.; Liu, X.*, et al.*, Printable metal–polymer conductors for local drug delivery. *Nano Letters* **2022,** *22* (18), 7554-7562.
63. Tang, L.; Shang, J.; Jiang, X., Multilayered electronic transfer tattoo that can

enable the crease amplification effect. *Science Advances* **2021,** *7* (3), eabe3778.

64. Hlaing, T.; DiMino, T.; Kowey, P. R.*, et al.*, Ecg repolarization waves: Their genesis and clinical implications. *Ann Noninvasive Electrocardiol* **2005,** *10* (2), 211-23.
65. Gerson, M. C.; Phillips, J. F.; Morris, S. N.*, et al.*, Exercise-induced u-wave inversion as a marker of stenosis of the left anterior descending coronary artery. *Circulation* **1979,** *60* (5), 1014-20.
66. Viskin, S.; Heller, K.; Barron, H. V.*, et al.*, Postextrasystolic u wave augmentation, a new marker of increased arrhythmic risk in patients without the long qt syndrome. *Journal of the American College of Cardiology* **1996,** *28* (7), 1746-1752.
67. Zemelka-Wiacek, M., Metal allergy: State-of-the-art mechanisms, biomarkers, hypersensitivity to implants. *Journal of Clinical Medicine* **2022,** *11* (23), 6971.
68. Cheng, J.; Shang, J.; Yang, S.*, et al.*, Wet-adhesive elastomer for liquid metal-based conformal epidermal electronics. *Advanced Functional Materials* **2022,** *32* (25), 2200444.
69. Ding, L.; Hang, C.; Cheng, S.*, et al.*, A soft, conductive external stent inhibits intimal hyperplasia in vein grafts by electroporation and mechanical restriction. *ACS Nano* **2020,** *14* (12), 16770-16780.
70. Hang, C.; Ding, L.; Cheng, S.*, et al.*, A soft and absorbable temporary epicardial pacing wire. *Advanced Materials* **2021,** *33* (36), 2101447.
71. Zhang, M.; Yao, S.; Rao, W.*, et al.*, Transformable soft liquid metal micro/nanomaterials. *Materials Science and Engineering: R: Reports* **2019,** *138*, 1-35.
72. Tang, L.; Yang, S.; Zhang, K.*, et al.*, Skin electronics from biocompatible in situ welding enabled by intrinsically sticky conductors. *Advanced Science* **2022,** *9* (23), 2202043.
73. Mou, L.; Xia, Y.; Jiang, X., Epidermal sensor for potentiometric analysis of metabolite and electrolyte. *Analytical Chemistry* **2021,** *93* (33), 11525-11531.
74. Mou, L.; Xia, Y.; Jiang, X., Liquid metal-polymer conductor-based wireless, battery-free epidermal patch. *Biosensors and Bioelectronics* **2022,** *197*, 113765.
75. Sun, X.; Yuan, B.; Sheng, L.*, et al.*, Liquid metal enabled injectable biomedical technologies and applications. *Applied Materials Today* **2020,** *20*, 100722.
76. Guo, R.; Liu, J., Implantable liquid metal-based flexible neural microelectrode

array and its application in recovering animal locomotion functions. *Journal of Micromechanics and Microengineering* **2017,** *27* (10), 104002.

77. Abd, M. A.; Al-Saidi, M.; Lin, M.*, et al.* In *Surface feature recognition and grasped object slip prevention with a liquid metal tactile sensor for a prosthetic hand*, 2020 8th IEEE RAS/EMBS International Conference for Biomedical Robotics and Biomechatronics (BioRob), 29 Nov.-1 Dec. 2020; 2020; pp 1174-1179.
78. Shang, J.; Tang, L.; Guo, K.*, et al.*, Electronic exoneuron based on liquid metal for the quantitative sensing of the augmented somatosensory system. *Microsystems & Nanoengineering* **2023,** *9* (1), 112.
79. Oh, J.; Kim, S.; Lee, S.*, et al.*, A liquid metal based multimodal sensor and haptic feedback device for thermal and tactile sensation generation in virtual reality. *Advanced Functional Materials* **2021,** *31* (39), 2007772.
80. Pyun, K. R.; Rogers, J. A.; Ko, S. H., Materials and devices for immersive virtual reality. *Nature Reviews Materials* **2022,** *7* (11), 841-843.
81. Dong, R.; Wang, L.; Hang, C.*, et al.*, Printed stretchable liquid metal electrode arrays for in vivo neural recording. *Small* **2021,** *17* (14), e2006612.
82. Wu, M.; Zhuang, Q.; Yao, K.*, et al.*, Stretchable, skin-conformable neuromorphic system for tactile sensory recognizing and encoding. *InfoMat* **2023,** *5* (12), e12472.
83. Zhuang, Q.; Yao, K.; Wu, M.*, et al.*, Wafer-patterned, permeable, and stretchable liquid metal microelectrodes for implantable bioelectronics with chronic biocompatibility. *Science Advances* **2023,** *9* (22), eadg8602.
84. Chen, F.; Zhuang, Q.; Ding, Y.*, et al.*, Wet-adaptive electronic skin. *Advanced Materials* **2023,** *35*, 2305630.
85. Wang, D.; Dong, R.; Wang, X.*, et al.*, Flexible electronic catheter based on nanofibers for the in vivo elimination of circulating tumor cells. *ACS Nano* **2022,** *16* (4), 5274-5283.
86. Zhong, L.; Tang, L.; Yang, S.*, et al.*, Stretchable liquid metal-based metal-polymer conductors for fully screen-printed biofuel cells. *Analytical Chemistry* **2022,** *94* (48), 16738-16745.
87. Won, P.; Valentine, C. S.; Zadan, M.*, et al.*, 3d printing of liquid metal embedded elastomers for soft thermal and electrical materials. *ACS Applied Materials & Interfaces* **2022,** *14* (49), 55028-55038.

88. Dong, R.; Liu, Y.; Mou, L.*, et al.*, Microfluidics-based biomaterials and biodevices. *Advanced Materials* **2019,** *31* (45), 1805033.
89. Ryu, G.; Park, I.; Kim, H., Liquid metal micro- and nanodroplets: Characteristics, fabrication techniques, and applications. *ACS Omega* **2023,** *8* (18), 15819-15830.
90. Kim, M.; Lim, H.; Ko, S. H., Liquid metal patterning and unique properties for next-generation soft electronics. *Advanced Science* **2023,** *10* (6), 2205795.
91. Zheng, Y.; He, Z.; Gao, Y.*, et al.*, Direct desktop printed-circuits-on-paper flexible electronics. *Scientific Reports* **2013,** *3* (1), 1786.
92. Neumann, T. V.; Dickey, M. D., Liquid metal direct write and 3d printing: A review. *Advanced Materials Technologies* **2020,** *5* (9), 2000070.
93. Yang, J.; Tang, D.; Ao, J.*, et al.*, Ultrasoft liquid metal elastomer foams with positive and negative piezopermittivity for tactile sensing. *Advanced Functional Materials* **2020,** *30* (36), 2002611.
94. Kim, T.; Kim, D.-m.; Lee, B. J.*, et al.*, Soft and deformable sensors based on liquid metals. *Sensors* **2019,** *19* (19), 4250.
95. Gao, Y.; Ota, H.; Schaler, E. W.*, et al.*, Wearable microfluidic diaphragm pressure sensor for health and tactile touch monitoring. *Advanced Materials* **2017,** *29* (39), 1701985.
96. Chen, X.; Wan, H.; Guo, R.*, et al.*, A double-layered liquid metal-based electrochemical sensing system on fabric as a wearable detector for glucose in sweat. *Microsystems & Nanoengineering* **2022,** *8* (1), 48.
97. Lim, T.; Zhang, H., Multilayer carbon nanotube/gold nanoparticle composites on gallium-based liquid metals for electrochemical biosensing. *ACS Applied Nano Materials* **2021,** *4* (11), 12690-12701.
98. Cheng, S.; Hang, C.; Ding, L.*, et al.*, Electronic blood vessel. *Matter* **2020,** *3* (5), 1664-1684.
99. Kim, M.-g.; Lee, B.; Li, M.*, et al.*, All-soft supercapacitors based on liquid metal electrodes with integrated functionalized carbon nanotubes. *ACS Nano* **2020,** *14* (5), 5659-5667.
100. Liu, G.; Kim, J. Y.; Wang, M.*, et al.*, Soft, highly elastic, and discharge-current-controllable eutectic gallium–indium liquid metal–air battery operated at room temperature. *Advanced Energy Materials* **2018,** *8* (16), 1703652.
101. Ye, L.; Hong, Y.; Liao, M.*, et al.*, Recent advances in flexible fiber-shaped metal-

air batteries. *Energy Storage Materials* **2020,** *28*, 364-374.

102. Liu, D.; Su, L.; Liao, J.*, et al.*, Rechargeable soft-matter egain-mno2 battery for stretchable electronics. *Advanced Energy Materials* **2019,** *9* (46), 1902798.
103. Li, F.; Shu, J.; Zhang, L.*, et al.*, Liquid metal droplet robot. *Applied Materials Today* **2020,** *19*, 100597.
104. Weng, W.; Chen, P.; He, S.*, et al.*, Smart electronic textiles. *Angewandte Chemie International Edition* **2016,** *55* (21), 6140-6169.
105. Zhang, X.; Chen, G.; Sun, L.*, et al.*, Claw-inspired microneedle patches with liquid metal encapsulation for accelerating incisional wound healing. *Chemical Engineering Journal* **2021,** *406*, 126741.
106. Agrawal, D. R.; Tanabe, Y.; Weng, D.*, et al.*, Conformal phased surfaces for wireless powering of bioelectronic microdevices. *Nature Biomedical Engineering* **2017,** *1* (3), 0043.
107. Piñuela, M.; Mitcheson, P. D.; Lucyszyn, S., Ambient rf energy harvesting in urban and semi-urban environments. *IEEE Transactions on Microwave Theory and Techniques* **2013,** *61* (7), 2715-2726.
108. Yildiz, F., Potential ambient energy-harvesting sources and techniques. *Journal of Technology Studies* **2009,** *35* (1), 40-48.
109. Cansiz, M.; Altinel, D.; Kurt, G. K., Efficiency in rf energy harvesting systems: A comprehensive review. *Energy* **2019,** *174*, 292-309.
110. Teng, L.; Ye, S.; Handschuh-Wang, S.*, et al.*, Liquid metal-based transient circuits for flexible and recyclable electronics. *Advanced Functional Materials* **2019,** *29* (11), 1808739.
111. Liang, T.; Yuan, Y. J., Wearable medical monitoring systems based on wireless networks: A review. *IEEE Sensors Journal* **2016,** *16* (23), 8186-8199.
112. Khan, H.; Mahmood, N.; Zavabeti, A.*, et al.*, Liquid metal-based synthesis of high performance monolayer sns piezoelectric nanogenerators. *Nature Communications* **2020,** *11* (1), 3449.
113. Yang, Y.; Sun, N.; Wen, Z.*, et al.*, Liquid-metal-based super-stretchable and structure-designable triboelectric nanogenerator for wearable electronics. *ACS Nano* **2018,** *12* (2), 2027-2034.
114. Ali, A.; Shaukat, H.; Bibi, S.*, et al.*, Recent progress in energy harvesting systems for wearable technology. *Energy Strategy Reviews* **2023,** *49*, 101124.

115. Sha, Z.; Boyer, C.; Li, G.*, et al.*, Electrospun liquid metal/pvdf-hfp nanofiber membranes with exceptional triboelectric performance. *Nano Energy* **2022,** *92*, 106713.
116. Wang, Z. L.; Chen, J.; Lin, L., Progress in triboelectric nanogenerators as a new energy technology and self-powered sensors. *Energy & Environmental Science* **2015,** *8* (8), 2250-2282.
117. Wei, X.-K.; Domingo, N.; Sun, Y.*, et al.*, Progress on emerging ferroelectric materials for energy harvesting, storage and conversion. *Advanced Energy Materials* **2022,** *12* (24), 2201199.
118. Green, M.; Dunlop, E.; Hohl-Ebinger, J.*, et al.*, Solar cell efficiency tables (version 57). *Progress in Photovoltaics: Research and Applications* **2021,** *29* (1), 3-15.
119. Lipomi, D. J.; Tee, B. C.-K.; Vosgueritchian, M.*, et al.*, Stretchable organic solar cells. *Advanced Materials* **2011,** *23* (15), 1771-1775.
120. Yun, I.; Lee, Y.; Park, Y.-G.*, et al.*, Transferable transparent electrodes of liquid metals for bifacial perovskite solar cells and heaters. *Nano Energy* **2022,** *93*, 106857.
121. Li, J.-F.; Liu, W.-S.; Zhao, L.-D.*, et al.*, High-performance nanostructured thermoelectric materials. *NPG Asia Materials* **2010,** *2* (4), 152-158.
122. Tang, J.; Wang, J.; Liu, J.*, et al.*, A volatile fluid assisted thermo-pneumatic liquid metal energy harvester. *Applied Physics Letters* **2016,** *108* (2), 023903.
123. Leonov, V., Thermoelectric energy harvesting of human body heat for wearable sensors. *IEEE Sensors Journal* **2013,** *13* (6), 2284-2291.
124. Malakooti, M. H.; Kazem, N.; Yan, J.*, et al.*, Liquid metal supercooling for low-temperature thermoelectric wearables. *Advanced Functional Materials* **2019,** *29* (45), 1906098.
125. Silva, C. A.; lv, J.; Yin, L.*, et al.*, Liquid metal based island-bridge architectures for all printed stretchable electrochemical devices. *Advanced Functional Materials* **2020,** *30* (30), 2002041.
126. Yehezkeli, O.; Tel-Vered, R.; Wasserman, J.*, et al.*, Integrated photosystem ii-based photo-bioelectrochemical cells. *Nature Communications* **2012,** *3* (1), 742.
127. Gerster, D.; Reichert, J.; Bi, H.*, et al.*, Photocurrent of a single photosynthetic protein. *Nature Nanotechnology* **2012,** *7* (10), 673-676.
128. Wu, H.; Zhang, Y.; Kjøniksen, A.-L.*, et al.*, Wearable biofuel cells: Advances from

fabrication to application. *Advanced Functional Materials* **2021,** *31* (48), 2103976.

129. Ray, T. R.; Choi, J.; Bandodkar, A. J.*, et al.*, Bio-integrated wearable systems: A comprehensive review. *Chemical Reviews* **2019,** *119* (8), 5461-5533.
130. Khalid, S.; Raouf, I.; Khan, A.*, et al.*, A review of human-powered energy harvesting for smart electronics: Recent progress and challenges. *International Journal of Precision Engineering and Manufacturing-Green Technology* **2019,** *6* (4), 821-851.
131. Calabrese Barton, S.; Gallaway, J.; Atanassov, P., Enzymatic biofuel cells for implantable and microscale devices. *Chemical Reviews* **2004,** *104* (10), 4867-4886.
132. Hatada, M.; Loew, N.; Inose-Takahashi, Y.*, et al.*, Development of a glucose sensor employing quick and easy modification method with mediator for altering electron acceptor preference. *Bioelectrochemistry* **2018,** *121*, 185-190.
133. Yu, Y.; Nassar, J.; Xu, C.*, et al.*, Biofuel-powered soft electronic skin with multiplexed and wireless sensing for human-machine interfaces. *Science Robotics* **2020,** *5* (41), eaaz7946.
134. PEREIRA, A. R.; SEDENHO, G. C.; SOUZA, J. C. P. D.*, et al.*, Advances in enzyme bioelectrochemistry. *Anais da Academia Brasileira de Ciências* **2018,** *90*, 825-857.
135. Gao, W.; Emaminejad, S.; Nyein, H. Y. Y.*, et al.*, Fully integrated wearable sensor arrays for multiplexed in situ perspiration analysis. *Nature* **2016,** *529* (7587), 509-514.
136. Sakharov, D.; Shkurnikov, M.; Vagin, M. Y.*, et al.*, Relationship between lactate concentrations in active muscle sweat and whole blood. *Bulletin of Experimental Biology and Medicine* **2010,** *150* (1), 83.
137. Tehrani, F.; Teymourian, H.; Wuerstle, B.*, et al.*, An integrated wearable microneedle array for the continuous monitoring of multiple biomarkers in interstitial fluid. *Nature Biomedical Engineering* **2022,** *6* (11), 1214-1224.
138. Bandodkar, A. J.; Jeerapan, I.; Wang, J., Wearable chemical sensors: Present challenges and future prospects. *ACS Sensors* **2016,** *1* (5), 464-482.
139. Sempionatto, J. R.; Jeerapan, I.; Krishnan, S.*, et al.*, Wearable chemical sensors: Emerging systems for on-body analytical chemistry. *Analytical Chemistry* **2019,** *92* (1), 378-396.
140. Min, J.; Sempionatto, J. R.; Teymourian, H.*, et al.*, Wearable electrochemical

biosensors in north america. *Biosensors and Bioelectronics* **2021,** *172*, 112750.

141. Terse-Thakoor, T.; Punjiya, M.; Matharu, Z.*, et al.*, Thread-based multiplexed sensor patch for real-time sweat monitoring. *npj Flexible Electronics* **2020,** *4* (1), 18.
142. Yokus, M. A.; Songkakul, T.; Pozdin, V. A.*, et al.*, Wearable multiplexed biosensor system toward continuous monitoring of metabolites. *Biosensors and Bioelectronics* **2020,** *153*, 112038.
143. Kondoh, Y.; Kawase, M.; Ohmori, S., D-lactate concentrations in blood, urine and sweat before and after exercise. *European Journal of Applied Physiology and Occupational Physiology* **1992,** *65* (1), 88-93.
144. Sun, M.; Gu, Y.; Pei, X.*, et al.*, A flexible and wearable epidermal ethanol biofuel cell for on-body and real-time bioenergy harvesting from human sweat. *Nano Energy* **2021,** *86*, 106061.
145. Wang, C.; Shim, E.; Chang, H.-K.*, et al.*, Sustainable and high-power wearable glucose biofuel cell using long-term and high-speed flow in sportswear fabrics. *Biosensors and Bioelectronics* **2020,** *169*, 112652.
146. Mohebbi Najm Abad, J.; Farahbakhsh, A.; Mir, M.*, et al.*, Urea-self powered biosensors: A predictive evolutionary model for human energy harvesting. *Sensors* **2023,** *23* (19), 8180.
147. Gamella, M.; Campuzano, S.; Manso, J.*, et al.*, A novel non-invasive electrochemical biosensing device for in situ determination of the alcohol content in blood by monitoring ethanol in sweat. *Analytica Chimica Acta* **2014,** *806*, 1-7.
148. Jia, W. Z.; Valdes-Ramirez, G.; Bandodkar, A. J.*, et al.*, Epidermal biofuel cells: Energy harvesting from human perspiration. *Angewandte Chemie-International Edition* **2013,** *52* (28), 7233-7236.
149. Xu, Z.; Liu, Y.; Williams, I.*, et al.*, Flat enzyme-based lactate biofuel cell integrated with power management system: Towards long term in situ power supply for wearable sensors. *Applied Energy* **2017,** *194*, 71-80.
150. Jeerapan, I.; Sempionatto, J. R.; Pavinatto, A.*, et al.*, Stretchable biofuel cells as wearable textile-based self-powered sensors. *Journal of Materials Chemistry A* **2016,** *4* (47), 18342-18353.
151. Bandodkar, A. J.; You, J.-M.; Kim, N.-H.*, et al.*, Soft, stretchable, high power density electronic skin-based biofuel cells for scavenging energy from human

sweat. *Energy & Environmental Science* **2017,** *10* (7), 1581-1589.

152. Escalona-Villalpando, R. A.; Ortiz-Ortega, E.; Bocanegra-Ugalde, J. P.*, et al.*, Clean energy from human sweat using an enzymatic patch. *Journal of Power Sources* **2019,** *412*, 496-504.
153. Chen, X.; Yin, L.; Lv, J.*, et al.*, Stretchable and flexible buckypaper-based lactate biofuel cell for wearable electronics. *Advanced Functional Materials* **2019,** *29* (46), 1905785.
154. Wiig, H.; Swartz, M. A., Interstitial fluid and lymph formation and transport: Physiological regulation and roles in inflammation and cancer. *Physiological Reviews* **2012,** *92* (3), 1005-1060.
155. Valdés-Ramírez, G.; Li, Y.-C.; Kim, J.*, et al.*, Microneedle-based self-powered glucose sensor. *Electrochemistry Communications* **2014,** *47*, 58-62.
156. Falk, M.; Pankratov, D.; Lindh, L.*, et al.*, Miniature direct electron transfer based enzymatic fuel cell operating in human sweat and saliva. *Fuel Cells* **2014,** *14* (6), 1050-1056.
157. Kim, J.; Valdés-Ramírez, G.; Bandodkar, A. J.*, et al.*, Non-invasive mouthguard biosensor for continuous salivary monitoring of metabolites. *Analyst* **2014,** *139* (7), 1632-1636.
158. Mitsubayashi, K.; Arakawa, T., Cavitas sensors: Contact lens type sensors & mouthguard sensors. *Electroanalysis* **2016,** *28* (6), 1170-1187.
159. Falk, M.; Andoralov, V.; Blum, Z.*, et al.*, Biofuel cell as a power source for electronic contact lenses. *Biosensors and Bioelectronics* **2012,** *37* (1), 38-45.
160. Reid, R. C.; Minteer, S. D.; Gale, B. K., Contact lens biofuel cell tested in a synthetic tear solution. *Biosensors and Bioelectronics* **2015,** *68*, 142-148.
161. Chen, F.; Huang, Q.; Zheng, Z., Permeable conductors for wearable and on-skin electronics. *Small Structures* **2022,** *3* (1), 2100135.
162. Sato, K.; Kang, W.; Saga, K.*, et al.*, Biology of sweat glands and their disorders. I. Normal sweat gland function. *Journal of the American Academy of Dermatology* **1989,** *20* (4), 537-563.
163. Hodge, B. D.; Sanvictores, T.; Brodell, R. T., Anatomy, skin sweat glands. **2018**.
164. Baker, L. B.; Wolfe, A. S., Physiological mechanisms determining eccrine sweat composition. *European Journal of Applied Physiology* **2020,** *120* (4), 719-752.
165. SMITH, C. J.; HAVENITH, G., Body mapping of sweating patterns in athletes: A

sex comparison. *Medicine & Science in Sports & Exercise* **2012,** *44* (12), 2350-2361.

166. Sato, K., The mechanism of eccrine sweat secretion. *Perspectives in Exercise Science and Sports Medicine: Exercise, Heat, and Thermoregulation* **1993,** *6*, 85-117.
167. Sonner, Z.; Wilder, E.; Heikenfeld, J.*, et al.*, The microfluidics of the eccrine sweat gland, including biomarker partitioning, transport, and biosensing implications. *Biomicrofluidics* **2015,** *9* (3), 031301.
168. Yang, D. S.; Ghaffari, R.; Rogers, J. A., Sweat as a diagnostic biofluid. *Science* **2023,** *379* (6634), 760-761.
169. Chen, Y.; Lu, S.; Zhang, S.*, et al.*, Skin-like biosensor system via electrochemical channels for noninvasive blood glucose monitoring. *Science Advances* **2017,** *3* (12), e1701629.
170. Katchman, B. A.; Zhu, M.; Blain Christen, J.*, et al.*, Eccrine sweat as a biofluid for profiling immune biomarkers. *PROTEOMICS–Clinical Applications* **2018,** *12* (6), 1800010.
171. Moyer, J.; Wilson, D.; Finkelshtein, I.*, et al.*, Correlation between sweat glucose and blood glucose in subjects with diabetes. *Diabetes Technology & Therapeutics* **2012,** *14* (5), 398-402.
172. Jia, W.; Bandodkar, A. J.; Valdés-Ramírez, G.*, et al.*, Electrochemical tattoo biosensors for real-time noninvasive lactate monitoring in human perspiration. *Analytical Chemistry* **2013,** *85* (14), 6553-6560.
173. Patterson*, M. J.; Galloway, S. D. R.; Nimmo, M. A., Variations in regional sweat composition in normal human males. *Experimental Physiology* **2000,** *85* (6), 869-875.
174. Prompt, C. A.; Quinto, P. M.; Kleeman, C. R., High concentrations of sweat calcium, magnesium and phosphate in chronic renal failure. *Nephron* **2008,** *20* (1), 4-9.
175. Parrilla, M.; Cuartero, M.; Crespo, G. A., Wearable potentiometric ion sensors. *TrAC Trends in Analytical Chemistry* **2019,** *110*, 303-320.
176. Nyman, E.; Palmlöv, A., The elimination of ethyl alcohol in sweat1. *Skandinavisches Archiv Für Physiologie* **1936,** *74* (2), 155-159.
177. Buono, M. J., Sweat ethanol concentrations are highly correlated with co-existing

blood values in humans. *Experimental Physiology* **1999,** *84* (2), 401-4.

178. Sempionatto, J. R.; Lasalde-Ramírez, J. A.; Mahato, K.*, et al.*, Wearable chemical sensors for biomarker discovery in the omics era. *Nature Reviews Chemistry* **2022,** *6* (12), 899-915.
179. Lee, H.; Choi, T. K.; Lee, Y. B.*, et al.*, A graphene-based electrochemical device with thermoresponsive microneedles for diabetes monitoring and therapy. *Nature Nanotechnology* **2016,** *11* (6), 566-572.
180. Lee, H.; Song, C.; Hong, Y. S.*, et al.*, Wearable/disposable sweat-based glucose monitoring device with multistage transdermal drug delivery module. *Science Advances* **2017,** *3* (3), e1601314.
181. Xiao, J.; Liu, Y.; Su, L.*, et al.*, Microfluidic chip-based wearable colorimetric sensor for simple and facile detection of sweat glucose. *Analytical Chemistry* **2019,** *91* (23), 14803-14807.
182. He, W.; Wang, C.; Wang, H.*, et al.*, Integrated textile sensor patch for real-time and multiplex sweat analysis. *Science Advances* **2019,** *5* (11), eaax0649.
183. Suresh N. Thennadil, J. L. R., Brian J. Wenzel, Kevin H. Hazen, Timothy L. Ruchti, and Marshall B. Block, Comparison of glucose concentration in interstitial fluid, and capillary and venous blood during rapid changes in blood glucose levels. *Diabetes Technology & Therapeutics* **2001,** *3* (3), 357-365.
184. Pu, Z.; Zhang, X.; Yu, H.*, et al.*, A thermal activated and differential self-calibrated flexible epidermal biomicrofluidic device for wearable accurate blood glucose monitoring. *Science Advances* **2021,** *7* (5), eabd0199.
185. Karpova, E. V.; Shcherbacheva, E. V.; Galushin, A. A.*, et al.*, Noninvasive diabetes monitoring through continuous analysis of sweat using flow-through glucose biosensor. *Analytical Chemistry* **2019,** *91* (6), 3778-3783.
186. Bolat, G.; De la Paz, E.; Azeredo, N. F.*, et al.*, Wearable soft electrochemical microfluidic device integrated with iontophoresis for sweat biosensing. *Analytical and Bioanalytical Chemistry* **2022,** *414* (18), 5411-5421.
187. Inzucchi, S. E., Diagnosis of diabetes. *New England Journal of Medicine* **2012,** *367* (6), 542-550.
188. Komives, G. K.; Robinson, S.; Roberts, J. T., Urea transfer across the sweat glands. *Journal of Applied Physiology* **1966,** *21* (6), 1681-1684.
189. Subrahmanyam, S.; Piletsky, S. A.; Piletska, E. V.*, et al.*, 'Bite-and-

switch'approach using computationally designed molecularly imprinted polymers for sensing of creatinine. *Biosensors and Bioelectronics* **2001,** *16* (9-12), 631-637.

190. Kalasin, S.; Sangnuang, P.; Surareungchai, W., Lab-on-eyeglasses to monitor kidneys and strengthen vulnerable populations in pandemics: Machine learning in predicting serum creatinine using tear creatinine. *Analytical Chemistry* **2021,** *93* (30), 10661-10671.
191. Tonelli, M.; Manns, B., Supplementing creatinine-based estimates of risk in chronic kidney disease: Is it time? *The Journal of the American Medical Association* **2011,** *305* (15), 1593-1595.
192. Emaminejad, S.; Gao, W.; Wu, E.*, et al.*, Autonomous sweat extraction and analysis applied to cystic fibrosis and glucose monitoring using a fully integrated wearable platform. *Proceedings of the National Academy of sciences* **2017,** *114* (18), 4625-4630.
193. Ray, T. R.; Ivanovic, M.; Curtis, P. M.*, et al.*, Soft, skin-interfaced sweat stickers for cystic fibrosis diagnosis and management. *Science Translational Medicine* **2021,** *13* (587), eabd8109.
194. Beller, G. A.; Maher, J. T.; Hartley, L. H.*, et al.*, Changes in serum and sweat magnesium levels during work in the heat. *Aviation Space and Environmental Medicine* **1975,** *46* (5), 709-712.
195. Torrente-Rodríguez, R. M.; Tu, J.; Yang, Y.*, et al.*, Investigation of cortisol dynamics in human sweat using a graphene-based wireless mhealth system. *Matter* **2020,** *2* (4), 921-937.
196. Pearlmutter, P.; DeRose, G.; Samson, C.*, et al.*, Sweat and saliva cortisol response to stress and nutrition factors. *Scientific Reports* **2020,** *10* (1), 19050.
197. Kallapur, B.; Ramalingam, K.; Mujib, A.*, et al.*, Quantitative estimation of sodium, potassium and total protein in saliva of diabetic smokers and nonsmokers: A novel study. *Journal of Natural Science, Biology, and Medicine* **2013,** *4* (2), 341.
198. Yang, Y.; Song, Y.; Bo, X.*, et al.*, A laser-engraved wearable sensor for sensitive detection of uric acid and tyrosine in sweat. *Nature Biotechnology* **2020,** *38* (2), 217-224.
199. Zhao, J.; Nyein, H. Y. Y.; Hou, L.*, et al.*, A wearable nutrition tracker. *Advanced Materials* **2021,** *33* (1), 2006444.
200. Lin, S.; Yu, W.; Wang, B.*, et al.*, Noninvasive wearable electroactive

pharmaceutical monitoring for personalized therapeutics. *Proceedings of the National Academy of Sciences* **2020,** *117* (32), 19017-19025.

201. Yoon, H.-J.; Lee, G.; Kim, J.-T.*, et al.*, Biodegradable, three-dimensional colorimetric fliers for environmental monitoring. *Science Advances* **2022,** *8* (51), eade3201.
202. Liu, S.; Yang, D. S.; Wang, S.*, et al.*, Soft, environmentally degradable microfluidic devices for measurement of sweat rate and total sweat loss and for colorimetric analysis of sweat biomarkers. *EcoMat* **2023,** *5* (1), e12270.
203. Yin, L.; Kim, K. N.; Lv, J.*, et al.*, A self-sustainable wearable multi-modular e-textile bioenergy microgrid system. *Nature Communications* **2021,** *12* (1), 1542.
204. Manohar, A. K.; Bretschger, O.; Nealson, K. H.*, et al.*, The use of electrochemical impedance spectroscopy (eis) in the evaluation of the electrochemical properties of a microbial fuel cell. *Bioelectrochemistry* **2008,** *72* (2), 149-154.
205. Van Benschoten, J. J.; Lewis, J. Y.; Heineman, W. R.*, et al.*, Cyclic voltammetry experiment. *Journal of Chemical Education* **1983,** *60* (9), 772.
206. Gai, P.; Song, R.; Zhu, C.*, et al.*, A ternary hybrid of carbon nanotubes/graphitic carbon nitride nanosheets/gold nanoparticles used as robust substrate electrodes in enzyme biofuel cells. *Chemical Communications* **2015,** *51* (79), 14735-14738.
207. An, S. Y.; Schon, T. B.; McAllister, B. T.*, et al.*, Design strategies for organic carbonyl materials for energy storage: Small molecules, oligomers, polymers and supramolecular structures. *EcoMat* **2020,** *2* (4), e12055.
208. Hao, S.; Sun, X.; Zhang, H.*, et al.*, Recent development of biofuel cell based self-powered biosensors. *Journal of Materials Chemistry B* **2020,** *8* (16), 3393-3407.
209. Fu, Y.; Li, P.; Bu, L.*, et al.*, Exploiting metal-organic coordination polymers as highly efficient immobilization matrixes of enzymes for sensitive electrochemical biosensing. *Analytical Chemistry* **2011,** *83* (17), 6511-6517.
210. Jia, W.; Valdés-Ramírez, G.; Bandodkar, A. J.*, et al.*, Epidermal biofuel cells: Energy harvesting from human perspiration. *Angewandte Chemie International Edition* **2013,** *52* (28), 7233-7236.
211. Liu, Y.-L.; Jin, Z.-H.; Liu, Y.-H.*, et al.*, Stretchable electrochemical sensor for real-time monitoring of cells and tissues. *Angewandte Chemie International Edition* **2016,** *55* (14), 4537-4541.
212. Li, P.; Wu, Z.; Hu, H.*, et al.*, Efficient flexible perovskite solar cells using low-

cost cu top and bottom electrodes. *ACS Applied Materials & Interfaces* **2020,** *12* (23), 26050-26059.

213. Liu, Y.-L.; Huang, W.-H., Stretchable electrochemical sensors for cell and tissue detection. *Angewandte Chemie International Edition* **2021,** *60* (6), 2757-2767.
214. Greulich, C.; Braun, D.; Peetsch, A.*, et al.*, The toxic effect of silver ions and silver nanoparticles towards bacteria and human cells occurs in the same concentration range. *RSC Advances* **2012,** *2* (17), 6981-6987.
215. Selloum, D.; Chaaya, A. A.; Bechelany, M.*, et al.*, A highly efficient gold/electrospun pan fiber material for improved laccase biocathodes for biofuel cell applications. *Journal of Materials Chemistry A* **2014,** *2* (8), 2794-2800.
216. U S, J.; Goel, S., Microfluidic non-enzymatic biofuel cell integrated with electrodeposited metallic catalysts on a paper based platform. *Journal of Power Sources* **2021,** *510*, 230405.
217. Zhang, Y.; Hao, S.; Sun, X.*, et al.*, A self-powered glucose biosensor based on mediator-free hybrid cu/glucose biofuel cell for flow sensing of glucose. *Electroanalysis* **2022,** *34* (12), 1953-1960.
218. Kim, D. C.; Shim, H. J.; Lee, W.*, et al.*, Material-based approaches for the fabrication of stretchable electronics. *Advanced Materials* **2020,** *32* (15), 1902743.
219. Miyamoto, A.; Lee, S.; Cooray, N. F.*, et al.*, Inflammation-free, gas-permeable, lightweight, stretchable on-skin electronics with nanomeshes. *Nature Nanotechnology* **2017,** *12* (9), 907-913.
220. Fan, Y. J.; Li, X.; Kuang, S. Y.*, et al.*, Highly robust, transparent, and breathable epidermal electrode. *ACS Nano* **2018,** *12* (9), 9326-9332.
221. Pan, Q.; Tong, N.; He, N.*, et al.*, Electrospun mat of poly(vinyl alcohol)/graphene oxide for superior electrolyte performance. *ACS Applied Materials & Interfaces* **2018,** *10* (9), 7927-7934.
222. Ma, R.; Kang, B.; Cho, S.*, et al.*, Extraordinarily high conductivity of stretchable fibers of polyurethane and silver nanoflowers. *ACS Nano* **2015,** *9* (11), 10876-10886.
223. Sun, B.; McCay, R. N.; Goswami, S.*, et al.*, Gas-permeable, multifunctional on-skin electronics based on laser-induced porous graphene and sugar-templated elastomer sponges. *Advanced Materials* **2018,** *30* (50), 1804327.
224. Min, H.; Jang, S.; Kim, D. W.*, et al.*, Highly air/water-permeable hierarchical mesh

architectures for stretchable underwater electronic skin patches. *ACS Applied Materials & Interfaces* **2020,** *12* (12), 14425-14432.

225. Zhu, D.; Handschuh-Wang, S.; Zhou, X., Recent progress in fabrication and application of polydimethylsiloxane sponges. *Journal of Materials Chemistry A* **2017,** *5* (32), 16467-16497.
226. Lan, W.-J.; Maxwell, E. J.; Parolo, C.*, et al.*, Paper-based electroanalytical devices with an integrated, stable reference electrode. *Lab on a Chip* **2013,** *13* (20), 4103-4108.
227. Ghosh, R.; Quayle, J. R., Phenazine ethosulfate as a preferred electron acceptor to phenazine methosulfate in dye-linked enzyme assays. *Analytical Biochemistry* **1979,** *99* (1), 112-7.
228. Suzuki, N.; Lee, J.; Loew, N.*, et al.*, Engineered glucose oxidase capable of quasi-direct electron transfer after a quick-and-easy modification with a mediator. *International Journal of Molecular Sciences* **2020,** *21* (3), 1137.